Doctoral Dissertation

Numerical Analysis on the Dynamic Performance of the Rotating Drill Pipe Model in Uniform Flow due to the Magnus Effect

HANNY TUN

June 2024

Graduate School of Engineering

Osaka University

Numerical Analysis on the Dynamic Performance of the Rotating Drill Pipe Model in Uniform Flow due to the Magnus Effect

By

HANNY TUN

A Dissertation for the Doctor of Engineering Degree
submitted to

Graduate School of Engineering

Department of Naval Architecture and Ocean Engineering

Osaka University

in June 2024

Supervised by

Professor Hiroyoshi Suzuki

Committee members

Professor Munehiko Minoura

Associate Professor Hidetaka Senga

Abstract

In recent years, drilling operations have primarily focused on exploration of oil and gas production as well as carrying out scientific research. Extracting core samples from deep ocean regions and conducting environmental studies, including the identification of earthquake sources were demanded around the world . Throughout these operations, numerous drill pipe failures, caused by the complex dynamics of the drill pipe during riserless drilling, were encountered. As drill pipes reach the deep-sea regions, the pipe dynamics become increasingly complex, making it challenging to observe the underwater behavior. Moreover, the limited visibility from the drilling ship leads the difficulties in maintenance of Weight on Bit (WOB) and the rotation of the drill bit.

Based on the types of motion and the direction, many drill pipe dynamics such as the Magnus Effect, Vortex Induced Vibration (VIV), Whirl Motion, Stick-slip Motion, and Bit-Bounce Motion have emerged during the drilling operations. This study mainly focuses on the dynamic behavior of the drill pipe influenced by the Magnus effect among these dynamic motions. Depending on the length of the drill pipes used in the drilling operation, the bending deformation due to Magnus force can also be seen. In addition, the drill pipe can also be assumed to have a flexible structure compared to its diameter and length ratio although these pipes are generally made of steel.

In riserless drilling operation, the rotation of the drill pipe generates lift forces due to ocean currents, a phenomenon known as the Magnus effect. The Magnus effect, which mainly depends on the pipe rotation and the ocean current velocity, can also lead the pipe structural failures due to excessive axial stresses and fatigue. The key parameters affecting the Magnus effect are the flow velocity and the rotational speed of the pipe. Therefore, Suzuki et al., (2022), examined the dynamic behavior of the drill pipe under the Magnus effect using a non-rotating drill pipe model by experimental and numerical investigations.

This study investigates the nonlinear dynamic motions of the rotating drill pipe due to the Magnus effect based on numerical simulation by considering the gyroscopic effect and the rotary inertia of the pipe . A three-dimensional fully parameterized beam element based on the absolute nodal coordinate formulation (ANCF) is used to account for the rotary inertia of the rotating pipe model. The pipe's rotation is applied via a rotation

matrix at the top node and transmitted along the pipe's length through twisting, thereby addressing the nonlinear interaction between bending and torsional deformations.

In addition, three-dimensional components of hydrodynamics forces in relation to the inflow velocity of water, rotational velocity, and orientation of the pipe were computed using ANSYS Fluent. The obtained forces are applied as an external force vector on the pipe model. Moreover, the effect of internal viscous damping on the behavior of the rotating drill pipe model was also investigated. Description of the pipe deformation, including the status of WOB applied at the pipe bottom position is analyzed and discussed for each condition. Through a comparison of simulation results and experimental results, the applicability of the presented model drill pipe was confirmed.

Finally, the actual drill pipe behavior due to the Magnus Effect was evaluated and discussed based on the present drill pipe behavior estimation program by applying three-dimensional hydrodynamic forces and absolute nodal coordinate formulation (ANCF) based on the Fortran In-house Code. Therefore, the numerical study on the dynamic behaviors of the rotating drill pipe model due to the Magnus Effect was proposed and implemented for the application of actual drill pipe behavior estimation in this study.

Acknowledgments

In the Marine Hydro-Science and Engineering Laboratory, the entire journey of completing this doctoral thesis was encouraged by my supervisor Professor Dr., Hiroyoshi Suzuki with his unwavering support and guidance. I would like to express my deepest gratitude and appreciation to my supervisor for his expertise, insights, and invaluable advice in shaping the direction and quality of this research.

I am also grateful to all the professors and staff from Osaka University, and the MEXT scholarship organization for their great contributions starting from admission to throughout my doctoral course. Moreover, I would like to send my great thanks to Associate Professor, Dr., Hidetaka Senga, Mr. Kimura, Ms. Kikuchi, and Ms. Tatsumi for their kind support and contributions. I would like to mention my sincere appreciation to Assistant Prof., Dr., Thant Zin Htun, who gave me full theoretical guidance and great contributions to my research experience. For their contributions of knowledge, experience, and advice for doing the experiment, Internship experience, and Chikyu Drilling vessel field trip, I would like to send my great thanks to Dr., Tomoya Inoue, Dr., Tatsuya Kaneko, and all representatives from JAMSTEC.

In addition, I would like to extend my appreciation to my OU Seniors from Myanmar. Then, I would like to express my heartfelt thanks to the encouragement of Prof., Myint Myint Khine, Associate Prof., Khin Khin Moe and all the professors from Myanmar Maritime University and the teachers who taught and guided me directly or indirectly, starting from primary student life to until the doctoral course. I am indebted to my colleagues and friends for their support, encouragement, and understanding throughout this challenging journey.

Last but not least, I am deeply grateful to my parents, and all my family members, also Mr. Thet Cho Winn for their unconditional love, encouragement, and sacrifices. Their love and belief in me have been the driving force behind my long academic journey. This thesis would not have been possible without the support and contributions of those mentioned above. I am truly grateful to all from the deepest of my heart.

Hanny Tun

Suita, Osaka, Japan *June 2024*

Table of Contents

List of Figures

List of Tables

List of Abbreviations

Symbol	Meaning
ANCF	Absolute Nodal Coordinate Formulation
CFD	Computational Fluid Dynamics
CFx	Hydrodynamic force coefficient in x-direction
CFy	Hydrodynamic force coefficient in y-direction
DOF	Degree of Freedom
dp	Pushing distance
FSI	Fluid-Structure Interaction
NR	Ground Reaction Force
NE	Number of Elements
Rn	Reynolds number
r	The radius of the pipe
$r\omega/U$	Rotation ratio
U	Flow velocity
VIV	Vortex-Induced Vibration
WOB	Weight on Bit
Fx	Hydrodynamic Force in x-direction
Fy	Hydrodynamic Force in y-direction
Fz	Hydrodynamic Force in z-direction
ξ	Damping constant
θ	Tilt angle
α	Oblique angle
ω	Number of revolutions
l_p	Total length of the pipe model
l_a	Length of the pipe model in the air
l'	Length of the pipe model inside the ground

This page was intentionally left blank!

Chapter 1

Introduction

1.1 Background

In many oil and gas explorations, drilling operations have been mainly carried out for the exploration of underground natural resources and it has been recently carried out also for the evaluating of scientific research, like extracting the core sample from the deep ocean regions and performing environmental studies including the finding of earthquake occurrence sources. In Japan, many earthquakes are happening around the country year by year, and it still needs to carry out many environmental-related studies based on underwater dynamics-related research fields. To fulfill these requirements, the drilling vessel, Chikyu as shown in (Fig. 1.1) is operating around the country under the goals set up by the Japan Agency for Marine-Earth Science and Technology (JAMSTEC).

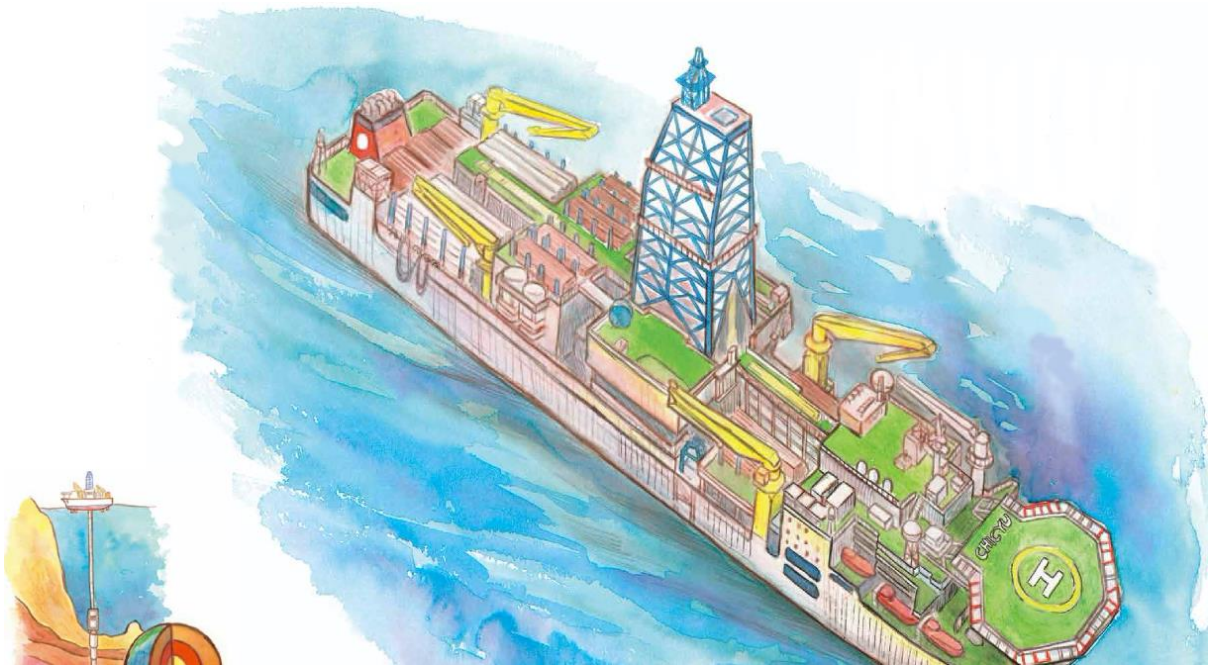

Fig. 1.1 Drilling vessel Chikyu and drilling operation illustration by (Tamano and Toshie, 2019)

The above figure, (Fig. 1.1) also represents the drilling vessel Chikyu in the true story of an event that took place during the 2011 Tohoku earthquake and tsunami by the author of (Tamano and Toshie, 2019), many people were injured and lost during this natural

disaster, it is also one of the proofs that the environmental research should be continuously carried out in the earthquake zones with the help of the drilling operation to prevent from the similar event in Japan, to know the underground environmental changes and to keep the sustainability of the nature around the world through the academic researches.

Generally, there are two different types of drilling operations, (i. Riser Drilling, which uses the riser pipes to connect the sea floor and drill ship and the drill pipe was operated inside the riser pipe, (ii. Riserless drilling, in which the drill pipe directly connects the drill ship to the sea floor, and this study mainly focuses on the riserless drilling operation.

During these operations, numerous drill pipe failures have been occurred due to the complex dynamics of the drill pipe in riserless drilling. If the drill pipes approach the deep-water regions, the more complex dynamics behaviors come out, but the visibility of the pipe behaviors is limited, and it is still difficult to adequately maintain WOB and the rotation of the drill bit.

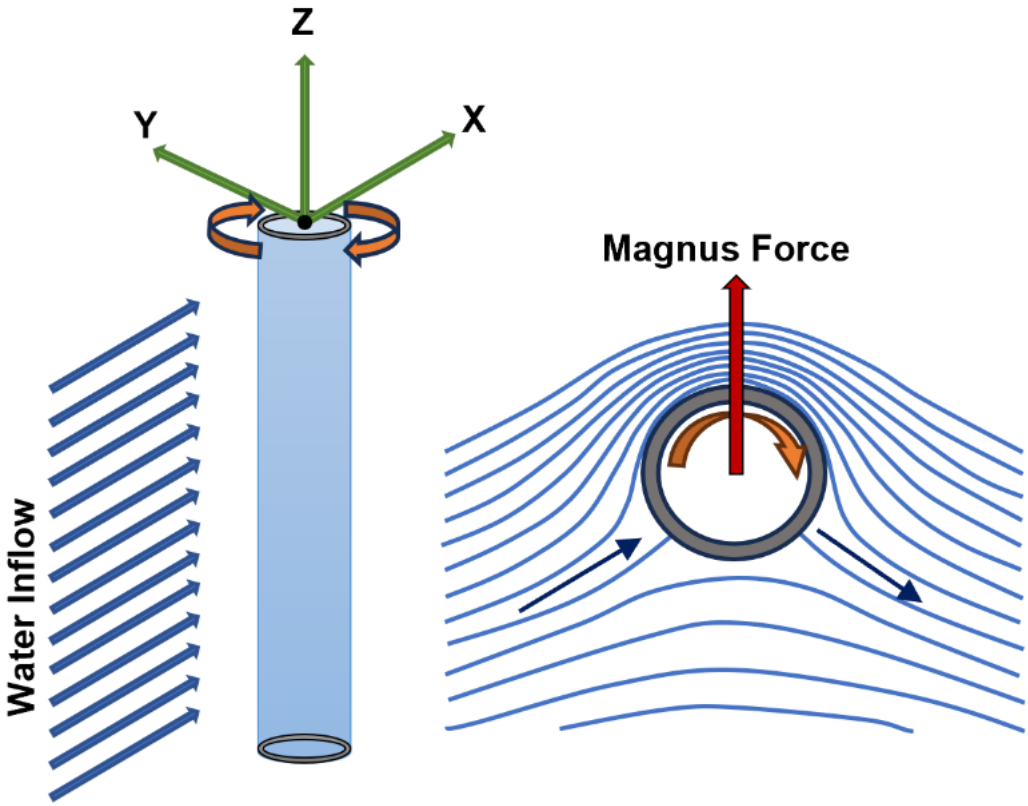

Fig. 1.2 Magnus effect of a rotating pipe model

Based on the types of motion and the direction, many drill pipe dynamics such as the Magnus Effect, Vortex Induced Vibration (VIV), Whirl Motion, Stick-slip Motion, and Bit-Bounce Motion have emerged during the drilling operations. Among these motions, this study mainly focuses on the dynamic behavior of the drill pipe due to the Magnus effect. The Magnus effect, primarily influenced by the pipe's rotation and the ocean current velocity, can also cause structural failures in the pipe due to excessive bending stresses and fatigue, as illustrated in (Fig. 1.2).

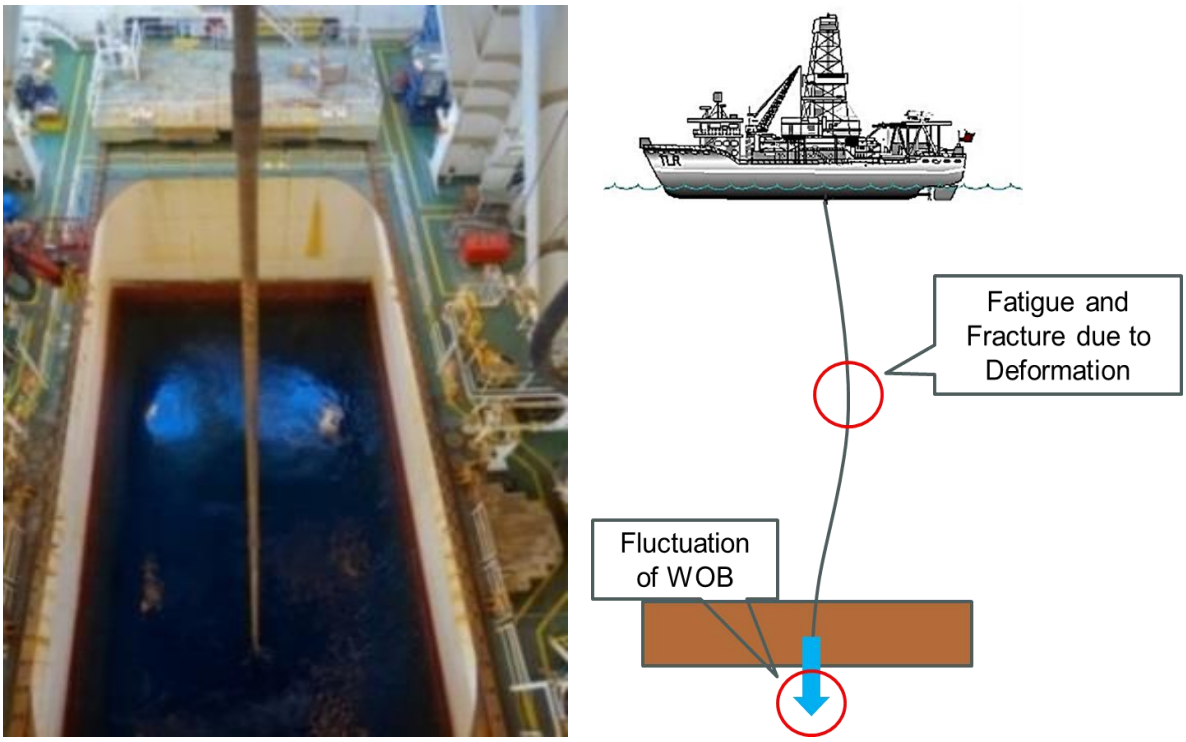

Fig. 1.3 Drill pipe in the drilling operation

Moreover, the drill pipes are subjected to ocean currents and a downward force; weight on bit (WOB) is exerted on the drill bit while rotating on its longitudinal axis as shown in (Fig. 1.3), during the drilling operations at sea. These forces play a significant role in the correct representation of the drill pipe's underwater dynamics, which is yet to be properly investigated. However, it may be challenging to adequately maintain WOB and rotate the drill bit because of the complex nonlinear dynamic motions of the drill pipe in deep drilling operations. The drill pipes and the drill bit used in the real drilling operations are shown in (Fig. 1.4), and these figures were taken during the field trip of the Chikyu vessel in Yokohama, Japan.

Thus, excessive bending stress and fatigue caused by the occurrence of a high magnitude of Magnus lift force leads to the drill pipe failure and it was investigated by (Inoue et al., 2017a). In addition, it is also still difficult to monitor the entire length of the long drill pipe in deep drilling operations since the dynamic behaviors of the pipe can be observed for only 30m on top of the pipe currently. Based on this fact, the numerical simulation of the rotating drill pipe can accomplish the investigation for the study of the underwater behavior of the drill pipe in deep drilling operations.

Fig. 1.4 Drill pipes and the drill bits in the Chikyu vessel

1.2 Motivation for this research

In previous studies, a two-dimensional hydrodynamic force model corresponding to the tangential and normal directions of the pipe was used, and the simulation results lacked congruence with the experimental results. Thus, a better approximation of the hydrodynamic forces was used by (Suzuki et al., 2022), and the simulation results indicated reasonable agreement with the experimental results in the case of the non-rotating pipe model. Nonetheless, the case of a rotating pipe model, which considers the pipe's rotation and rotary inertia under WOB fluctuation, is yet to be investigated.

In this study, we introduced the new hydrodynamics force model, such as lift force due to the Magnus effect and drag force due to fluid resistance acting on the drill pipe model

and applied the external forces to a model of the drill pipe to stimulate the underwater behaviors of the rotating drill pipe model.

Furthermore, the application of the three-dimensional fully parameterized ANCF beam elements leads to a constant mass matrix, which takes into account the rotary inertia terms. The element can also capture the cross-sectional deformation modes, such as torsion and shear deformation of the drill pipe model. As shown later in this paper, these ANCF beam elements can automatically account for the effects of gyroscopic forces and moments without the need to introduce any additional terms in the equations of motion.

In addition, consideration of the effect of hydrodynamic force and the internal viscous damping with different material models on the dynamic behaviors of the drill pipe model was evaluated and discussed based on the 24-DOF ANCF framework. Then, the fluctuation of WOB at the drill pipe bottom position was discussed and analyzed for each condition.

Thus, the present study mainly contributes to the dynamic behavior of the rotating drill pipe model due to the Magnus effect under WOB fluctuation by comparing the simulation and experimental results for the drill pipe model and the implementation of the underwater dynamic performance of the drill pipe was proposed by using three-dimensional ANCF beam element.

1.3 Literature Review

1.3.1 Drill Pipe Dynamics

Throughout the many decades, many researchers carried out research on the drill pipe dynamic considering the hydrodynamic force acting on the riser pipes. (Chung et al., 1981, 1993) conducted studies of hydrodynamic forces acting on the long pipes in riser drilling. Between these two papers, the behavior of an underwater deep-sea mining system (riser assembly) under environmental conditions such as current velocity, viscosity, and density, which vary with depth, was computed at the Reynolds number of the actual system (about 2.0×10^5) in the former one. Then, the several methods for suppression of VIV (Vortex induced vibration) of deep-sea mining systems (riser assembly) by using the actual size pipe were examined by the later one. Moreover, the interest in drill pipe dynamics was

extended by conducting the detailed measurement for the 2000[m] length of the riser assembly in terms of the vibration caused by drilling (Blevins et al., 2017).

In riser-less drilling, the drill pipe is directly exposed to the external environment, leading to increased complexity in its behavior. In deep drilling scenarios, the complexity escalates as the drill pipe elongates, nearing the predominant period of the ship's motion, thereby affecting its natural period. Understanding drill pipe dynamics is crucial for drilling operations to enhance efficiency and safety. For instance, the fluctuating axial stress induced by ship motion can be substantially higher up to ten times than anticipated under rigid body assumptions, highlighting the significant impact of drill pipe dynamics and the potential risk of drill pipe failure in extreme cases. Therefore, the drill pipe failure and fatigue failure of the drill pipe due to impact forces and cyclic loading acting on the drill pipe were studied and reported experimentally and numerically by (Zhao et al., 2018).

Vortex excitation in tidal currents becomes intricate due to drill pipe rotation, resulting in characteristics distinct from those observed in a stationary pipe was stated in (Inoue et al., 2013*)*. Moreover, the rotation of the drill pipe within tidal currents induces a lift force known as the Magnus effect, causing the pipe's deformation. These dynamics have been implicated in the damage and rupture of drill pipes and the disruption of drilling operations was studied by (Inoue at al., 2017a). However, only the uppermost 30 meters of the drill pipe, which extends several thousand meters, is observable. Presently, inferring drill pipe deformation and behavior underwater solely from fluctuations and behavior at the top 30 meters is unattainable. Consequently, there is considerable anticipation regarding the use of numerical analysis for estimating drill pipe behavior.

(Batchelor et al., 1967) defined the Magnus effect as the occurrence of a side-force on a rigid circular cylinder when it is both rotating and moving forward, as well as on a sphere. The Magnus effect finds applications in ship and ocean engineering, such as in ship roll stabilization (Ozturk et al., 2020) and the design of rotor ships (Nuttall & Kaitu'u et al., 2016).

The key parameters influencing the lift force generated by the Magnus effect are the inflow velocity and rotation speed. Depending on the operational conditions, the lift force can exceed several times the drag induced by the current. Due to the spatial and temporal fluctuations in tidal currents, the lift force fluctuates and varies spatially.

Additionally, the motion of the drill pipe and the self-excited rotation resulting from its rotation affect the inflow velocity and angle. This phenomenon within drill pipe dynamics holds significant operational importance and has garnered academic interest.

This study focuses on examining the dynamics of drill pipes influenced by the three-dimensional Magnus effect, accounting for both temporal and spatial variations. Addressing this challenge requires analyzing the motion of a very long pipe with rotation while considering fluid-structure interaction. However, it remains uncertain whether hydrodynamic forces, including lift and drag, resulting from the Magnus effect on a rotating drill pipe, can be accurately represented by those acting on a two-dimensional cylinder.

Previous attempts to analyze the deformation of the model pipe through numerical analysis, particularly using the lift and drag forces based on flow simulation around a two-dimensional cylinder, were proposed by (Suzuki et al., 2016, 2018; Inoue et al., 2017b, 2019). Of these, the detailed findings of the study by (Inoue et al., 2019) are highlighted. This study investigated the behavior of the drill pipe model under rotation when its bottom end was not fixed, simulating hang-off conditions through model experiments and numerical simulations.

In contrast, our study first focused on measuring hydrodynamic forces, such as lift and drag, resulting from the Magnus effect on a rotating drill pipe model under uniform flow conditions (with the lower end of the drill pipe model grounded). Additionally, we observed the dynamic behavior of the drill pipe model and measured its deformation due to the Magnus effect. Furthermore, we validated the accuracy of our numerical analysis against the measured results. Despite encountering challenges such as uncertainty regarding the ground state of the lower end of the drill pipe model and limitations in hydrodynamic force measurement methods, we have made progress and reported some significant findings.

1.3.2 Kinematic Description of Three-dimensional ANCF Beam Element

In the theory of a three-dimensional Absolute Nodal Coordinate Formulation (ANCF) (Shabana, 1998; Shabana and Yakoub, 2001; Gerstmayr and Shabana, 2006; Yakoub and Shabana, 2001), the kinematic description of the element coordinates can be expressed

as the nodal displacements and position gradient (slopes) which are defined in global inertia frame. ANCF is not based on any infinite or finite rotation coordinates, and it does not suffer from singularities that emerge from angle parameterization. Moreover, it has been proven that an arbitrary motion produces zero strain in the literature of (Otsuka et al., 2022). Therefore, ANCF is well suited for large deformation and rotation cases, and it can be applied for analyzing the flexible multi-body dynamic problems of many applications.

The consideration of the rotary inertia effect in ANCF was discussed also by (Shabana and Yakoub, 2001) and the dynamic analysis of the rotating drill pipe model incorporating the Magnus effect and rotary inertia of the pipe was stated in (Tun et al., 2023).

Based on the non-incremental finite element method for large rotation and deformation problems, different approaches for viscoelastic constitutive models have already been developed in some literature. The ANCF solid element considering the internal viscous damping based on the Kelvin-Voigt model was proposed by (Ma Chao et al., 2016). An internal damping model based on the Rayleigh functions, which account for the linear viscoelastic relations to multiaxial stress, including the terms of material response to deviatoric and dilutional excitations, was developed in (Garcia-Vallejo et al., 2005). Meanwhile, the Poisson's effect was neglected yet in both elastic and viscous terms in this approach to avoid the Poisson locking problems. Therefore, the constitutive equations for isotropic homogenous viscoelastic material which took into account the Poisson's effect were developed by (Htun et al., 2020). Moreover, the literature of (Berzeri and Shabana, 2000; Htun et al., 2020) stated that the dilatational damping factor, γ_d can be assumed as a fraction, ξ (damping constant) of its critical value for a pure deviatoric (torsion) test case.

In ANCF simulation, it is crucial to develop an efficient and reliable elastic force model for nonlinear finite element analysis. The elastic force models which account for the coupling between bending and axial deformations using a continuum mechanics approach in ANCF had been developed by (Berzeri and Shabana, 2000), and modeling nonlinear nearly incompressible materials with polynomial Mooney Rivlin models and volumetric energy penalty function was presented by (Orzechowski and Fraczek, 2015), description of elastic force and study on the stiffness properties in ANCF was proposed

by (Sopanen and Mikkola, 2003a; 2003b) with the application of fully parameterized ANCF beam element.

Based on previous studies, this study applied the two well-known hyper-elastic force models: Neo Hookean and incompressible Mooney Rivlin material models (Mooney, M.A, 1940; Rivlin, R.S, 1948), which are based on strain energy density function and applicable to consider the large deformation problems.

1.3.3 Experimental Study of the Drill Pipe Model

To investigate the underwater behavior of the drill pipe model, a model test was conducted at Osaka University's Towing Tank. In this experiment, we applied the rotation to the drill pipe model from a rotating device, and the flow velocity was created by running a towing carriage to take the test at the different flow and rotational velocities. The detailed status of the model test experiment and the simulation results of the non-rotating pipe model in ANCF were described by (Suzuki et al., 2022)and the calculation results for the rotating drill pipe model considering the pipe rotary inertia were analyzed and validated with the experimental results in (Tun et al., 2023).

1.3.4 Estimation of Hydrodynamic Forces exerted on the Rotating Cylinder

To consider the hydrodynamic forces exerted on the drill pipe, there are several approaches for calculating these forces in previous studies. The consideration of the computational hydrodynamic forces was also described in (Nakajima et al., 1983; Takehara et al., 2011). Moreover, the estimation of two-dimensional hydrodynamic forces exerted on a rotating cylinder was proposed by (Inoue et al., 2019). In the studies of (Chen and Rheem, 2019; Suzuki et al., 2022), the approaches for estimating the magnitude of three-dimensional hydrodynamic forces exerted on the rotating cylinder in the flow were described.

Based on previous studies, the hydrodynamic force estimation for a three-dimensional tilt-oblique rotating cylinder measured with respect to the flow direction was developed by (Suzuki et al., 2022). We applied this approach to the drill pipe underwater behavior estimation program and the validations against the numerical and experimental results were shown in (Tun et al., 2023).

1.4 Objectives of the Thesis

This study mainly focusses on the study of the dynamic behavior of the rotating drill pipe due to the Magnus effect under the WOB fluctuation by applying a fully parameterized ANCF beam element. The main objectives of this study are,

- To develop a numerical simulation model that takes into account the pipe rotary inertia and considers the cross-sectional deformation modes like torsion and shear, which can capture the underwater dynamic motions of the drill pipe that cannot be easily captured during the actual drilling operation.
- To study the flow and forces around the drill pipe in a riserless drilling operation, by applying the three-dimensional hydrodynamic force developed based on the tilt-oblique rotating cylinder to stimulate the deformed shape of the drill pipe.
- To deepen the understanding of the application of Absolute Nodal Coordinate Formulation in drill pipe dynamics.
- To observe the deformation profiles of the drill pipe due to the Magnus effect based on different material models and to apply for the actual scale drill pipe that was used in the drilling operation.

1.5 Novelty of This Research

The contributions of this doctoral dissertation are as follows.

- The numerical model of a rotating drill pipe model, which automatically accounts for the rotary inertia and can capture the cross-sectional deformation modes, such as torsion and shear deformations,
- Three-dimensional hydrodynamic force model considering the flow around the deformed drill pipe,
- The dynamic behaviors of the drill pipe model considering the effect of internal viscous damping under the WOB fluctuations,
- The underwater behavior of the actual drill pipe due to the Magnus Effect applying the fully parameterized ANCF beam element.

1.6 Thesis Overview

This dissertation has been structured as the following chapter sections.

Chapter 1 represents the Introduction of this dissertation including the literature review, objectives, and contributions on the dynamics of the drill pipe in the drilling operations,

Chapter 2 presents the Kinematic description of the fully parameterized ANCF beam element for the rotating drill pipe model and the theoretical approach of considering the rotary inertia of the pipe model incorporating the Magnus Effect,

Chapter 3 shows the Experimental study of the drill pipe model due to the Magnus effect by considering the hydrodynamic forces and the deformation of the pipe model,

Chapter 4 expresses the three-dimensional hydrodynamic force estimation of the drill pipe model by ANSYS Fluent 2020 R2 compared to the previous and present studies,

Chapter 5 describes the Computational Set up and constraints for ANCF Simulation and the computational results for the underwater behavior of the rotating drill pipe model under WOB fluctuation,

Chapter 6 demonstrates the underwater performance of the actual scale drill pipe due to the Magnus effect by applying the present analytical drill pipe model,

Chapter 7 will be the conclusion and future works.

Finally, it was mentioned in all the references for this dissertation.

Chapter 2

Modeling the Rotating Drill Pipe Model by Applying Absolute Nodal Coordinate Formulation

2.1 Kinematic Description of a Fully Parameterized ANCF Beam Element

Absolute Nodal Coordinate Formulation (ANCF) (Shabana et al., 1998; 2001) is the non-incremental finite element formulation suited for the large deformation and rotation problems of the flexible multi-body dynamics field. In ANCF, element coordinates are expressed in terms of nodal displacements and position gradient vectors, which are defined in the global inertia frame as shown in (Fig. 2.1). A global shape function that can represent the complete set of rigid modes was used to capture the beam deformation.

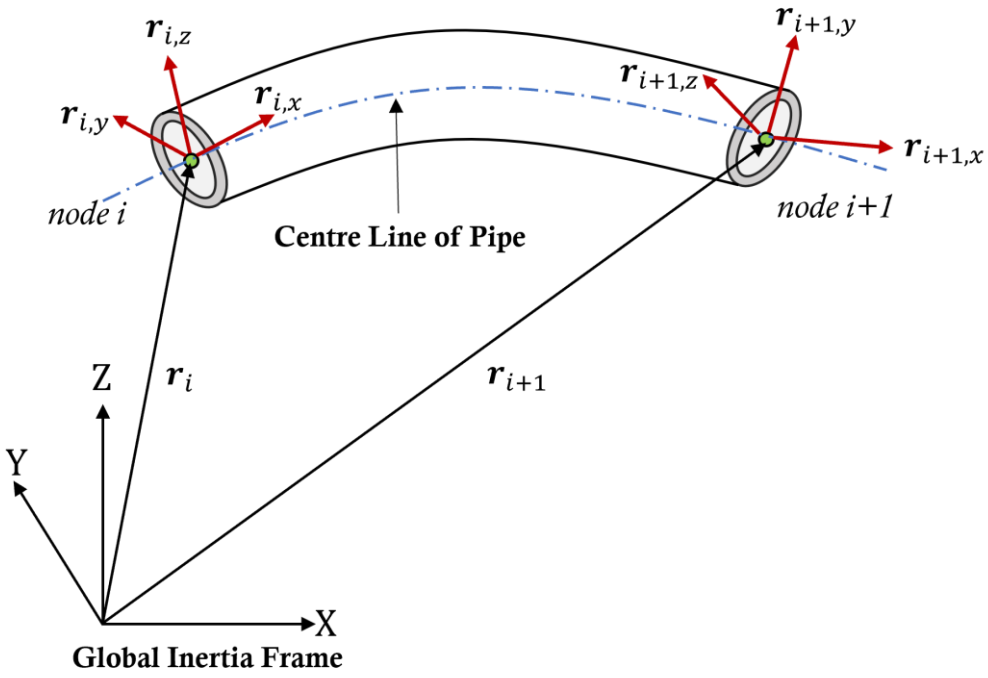

Fig. 2.1 Description of an ANCF beam element in the global inertia frame

Because of its many computational advantages, there are several practical applications and studies by using the ANCF beam element and formulation such as analysis of thin beams and cables (Gerstmayr et al., 2006), dynamic analysis of remotely operated

underwater vehicles (ROV) and its tethered cable system (Htun et al., 2019, 2020, 2021, 2022), the studies of stiffness properties and description of elastic forces by using ANCF beam element (Sopanen et al., 2003), dynamic analysis of rotating shafts using nonlinear super element (Wang et al., 2017). In this study, we applied a three-dimensional ANCF beam element to study the dynamic behaviors of a rotating drill pipe model in uniform flow.

For a three-dimensional fully parameterized beam element, the global position vector, $\boldsymbol{r}$ of an arbitrary point can be expressed in terms of the shape function $\boldsymbol{S}$ and element nodal coordinate vector, $\boldsymbol{e}$ as

$$\boldsymbol{r} = \boldsymbol{S}(\boldsymbol{x}, \boldsymbol{y}, \boldsymbol{z}) \, . \boldsymbol{e} \tag{2.1}$$

where, $\boldsymbol{S}$ is the global shape function matrix defined based on the element coordinates using the Euler-Bernoulli beam theory, as in (Eq. 2.1).

$$\boldsymbol{S} = [S_1\boldsymbol{I} \;\; S_2\boldsymbol{I} \;\; S_3\boldsymbol{I} \;\; S_4\boldsymbol{I} \;\; S_5\boldsymbol{I} \;\; S_6\boldsymbol{I} \;\; S_7\boldsymbol{I} \;\; S_8\boldsymbol{I}\,] \tag{2.2}$$

Then, $\boldsymbol{I}$ is the 3 x 3 identity matrix and each value of $\boldsymbol{S}$ was stated in (Shabana et al., 2001). The nodal coordinate vector of the beam element, $\boldsymbol{e}$ represents,

$$\boldsymbol{e} = \left[\boldsymbol{r}_i^T \;\; \boldsymbol{r}_{i,x}^T \;\; \boldsymbol{r}_{i,y}^T \;\; \boldsymbol{r}_{i,z}^T \;\; \boldsymbol{r}_{i+1}^T \;\; \boldsymbol{r}_{i+1,x}^T \;\; \boldsymbol{r}_{i+1,y}^T \;\; \boldsymbol{r}_{i+1,z}^T\right] \tag{2.3}$$

where, $\boldsymbol{r_i}$ and $\boldsymbol{r_{i+1}}$ show the position vectors at node *i* and *i+1* respectively, and the gradient vectors ($\boldsymbol{r_{i,x}}$, $\boldsymbol{r_{i,y}}$, $\boldsymbol{r_{i,z}}$, $\boldsymbol{r_{i+1,x}}$, $\boldsymbol{r_{i+1,y}}$, $\boldsymbol{r_{i+1,z}}$), respectively describe the partial differentiation of the position vector $\boldsymbol{r_i}$ and $\boldsymbol{r_{i+1}}$ in the global inertial frame.

In general, the kinetic energy of the ANCF beam element can be described as follows,

$$T = \frac{1}{2}\int_V \rho \dot{\boldsymbol{r}}^{\boldsymbol{T}}\dot{\boldsymbol{r}}\,|\boldsymbol{J_0}|dV = \frac{1}{2}\left(\dot{\boldsymbol{e}}^T \int_V \rho \boldsymbol{S}^T\,\boldsymbol{S}|\boldsymbol{J_0}|dV\right)\dot{\boldsymbol{e}} = \frac{1}{2}\dot{\boldsymbol{e}}^T\boldsymbol{M}\dot{\boldsymbol{e}} \tag{2.4}$$

where $\boldsymbol{M}$ is the constant mass matrix and $\boldsymbol{M}$ can be expressed as,

$$\boldsymbol{M} = \int_V \rho \boldsymbol{S}^T\,\boldsymbol{S}|\boldsymbol{J_0}|dV \tag{2.5}$$

Here, the matrix, $\boldsymbol{J_0}$ can be stated by using gradient slope vectors,
$\boldsymbol{J_0} = \left[\boldsymbol{r}_{,x} \;\; \boldsymbol{r}_{,y} \;\; \boldsymbol{r}_{,z}\right]$ and $|\boldsymbol{J_0}|$ represents the Jacobian of the mapping between the current and reference configurations (Htun et al., 2020).

2.2 Rotary Inertia Effect in ANCF Formulation

In the three-dimensional fully parameterized ANCF beam element, the effect of rotary inertia of the beam cross section can be automatically accounted for (Shabana et al., 2001). Moreover, the position of the arbitrary point, P on the cross-section of the beam element can be described as,

$$\boldsymbol{r}_P = \boldsymbol{S}\boldsymbol{e} \tag{2.6}$$

And, it can also be written as,

$$\boldsymbol{r}_P = \boldsymbol{S}_l\boldsymbol{e}_l + \boldsymbol{S}_s\boldsymbol{e}_s \tag{2.7}$$

where, $\boldsymbol{S}_l$ represents the shape function matrix on the beam's length, and $\boldsymbol{S}_s$ means the shape function matrix of the beam's transverse cross-section, (Yakoub et al., 2001).

Here, $\boldsymbol{e}_l$ and $\boldsymbol{e}_s$ represents the nodal coordinate vectors of the element with respect to the shape function $\boldsymbol{S}_l$ and $\boldsymbol{S}_s$ respectively. Then, the absolute velocity vector will be,

$$\dot{\boldsymbol{r}}_P = \boldsymbol{S}\dot{\boldsymbol{e}} = \boldsymbol{S}_l\dot{\boldsymbol{e}}_l + \boldsymbol{S}_s\dot{\boldsymbol{e}}_s \tag{2.8}$$

The detailed representation of the beam kinetic energy including the effect of rotary inertia was clearly stated in (Shabana et al., 2001).

2.3 Gyroscopic Effect in Rotating Drill Pipe Model

ANCF is an absolute-coordinates-based full inertia approach that can also automatically account for the gyroscopic effect when a rotational displacement is set up as the boundary condition and special treatment was not needed for incorporating the gyroscopic effect in the description of the beam's inertia.

In this analysis, a rotation matrix, $\boldsymbol{R_\theta}$ was implied as a boundary condition at the top node of the drill pipe model as in (Eq. 2.9), to consider the rotation of the drill pipe. Here, $\boldsymbol{J_0}$ represents the Jacobian matrix of the position vector at the initial reference position.

$$\boldsymbol{R_\theta} = \boldsymbol{J_0^{-1}}\begin{pmatrix} 1 & 0 & 0 \\ 0 & \cos\theta & -\sin\theta \\ 0 & \sin\theta & \cos\theta \end{pmatrix}, \quad \boldsymbol{J_0} = \begin{pmatrix} r_{,x_0} & r_{,y_0} & r_{,z_0} \end{pmatrix} \tag{2.9}$$

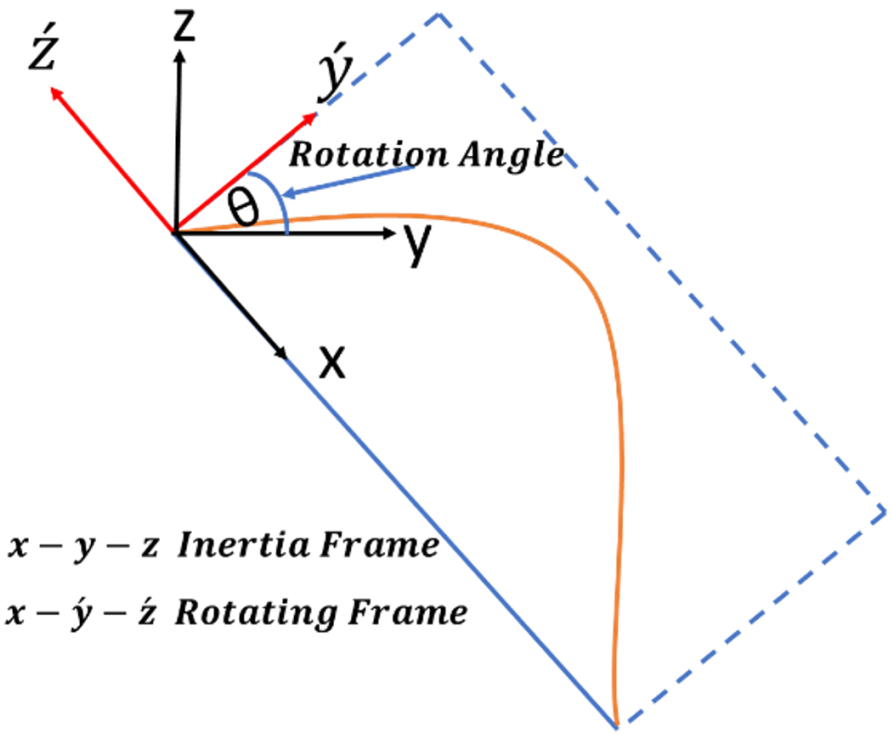

Fig. 2.2 Inertial frame and rotating frame of the beam element

The global position vector of the j^{th} element, $\boldsymbol{r_j}$, defined in the inertia frame can be generally expressed as,

$$\boldsymbol{r}_j = \bar{\boldsymbol{A}}_{\boldsymbol{\theta}}\bar{\boldsymbol{r}}_j, j=1,2 \tag{2.10}$$

where, $\bar{\boldsymbol{r}}_j$ represents the position vector defined in the rotating frame,

and the rotation matrix, $\bar{\boldsymbol{A}}_{\boldsymbol{\theta}}$ will be,

$$\bar{\boldsymbol{A}}_{\boldsymbol{\theta}} = \begin{bmatrix} 1 & 0 & 0 \\ 0 & cos\theta & -sin\theta \\ 0 & sin\theta & cos\theta \end{bmatrix} \tag{2.11}$$

The block diagonal matrix, $\boldsymbol{A}_{\boldsymbol{\theta}}$ can be described as,

$$\boldsymbol{A}_{\boldsymbol{\theta}} = diag[\,\bar{\boldsymbol{A}}_{\boldsymbol{\theta 1}}, \bar{\boldsymbol{A}}_{\boldsymbol{\theta 2}}, \ldots\ldots, \bar{\boldsymbol{A}}_{\boldsymbol{\theta n}}\,] \tag{2.12}$$

the position vector, $\boldsymbol{r}$ can also be stated as,

$$\boldsymbol{r} = \boldsymbol{A}_{\boldsymbol{\theta}}\bar{\boldsymbol{r}} = \boldsymbol{S}\boldsymbol{A}_{\boldsymbol{\theta}}\bar{\boldsymbol{e}} \tag{2.13}$$

and the velocity vector, $\dot{\boldsymbol{r}}$ will become,

$$\dot{\boldsymbol{r}} = \boldsymbol{S}\boldsymbol{A}_{\boldsymbol{\theta}}\dot{\bar{\boldsymbol{e}}} + \boldsymbol{S}\dot{\boldsymbol{A}_{\boldsymbol{\theta}}}\bar{\boldsymbol{e}} \tag{2.14}$$

Then, the kinetic energy of the beam in the rotating frame can be expressed as:

$$T_r = \frac{\rho}{2}\int_V \left(\dot{\bar{\boldsymbol{e}}}^T \boldsymbol{A}_{\boldsymbol{\theta}}{}^T \boldsymbol{S}^T \boldsymbol{S}\boldsymbol{A}_{\boldsymbol{\theta}}\dot{\bar{\boldsymbol{e}}} + \dot{\bar{\boldsymbol{e}}}^T \boldsymbol{A}_{\boldsymbol{\theta}}{}^T \boldsymbol{S}^T \boldsymbol{S}\dot{\boldsymbol{A}_{\boldsymbol{\theta}}}\bar{\boldsymbol{e}} + \dot{\bar{\boldsymbol{e}}}^T \dot{\boldsymbol{A}_{\boldsymbol{\theta}}}{}^T \boldsymbol{S}^T \boldsymbol{S}\boldsymbol{A}_{\boldsymbol{\theta}}\dot{\bar{\boldsymbol{e}}} + \dot{\bar{\boldsymbol{e}}}^T \dot{\boldsymbol{A}_{\boldsymbol{\theta}}}{}^T \boldsymbol{S}^T \boldsymbol{S}\dot{\boldsymbol{A}_{\boldsymbol{\theta}}}\bar{\boldsymbol{e}}\right) dV \tag{2.15}$$

Using Lagrange's equation, one can state the consideration of inertia force as shown in (Eq. 2.16). In this equation, the term, $\boldsymbol{A_\theta}^T \boldsymbol{M}\boldsymbol{A_\theta}\ddot{\bar{\boldsymbol{e}}}$ represents the inertia force, and the second term, $\boldsymbol{G}\dot{\bar{\boldsymbol{e}}}$ describes the gyroscopic force and the final term, $\boldsymbol{A_\theta}^T \boldsymbol{M}\ddot{\boldsymbol{A}}_{\boldsymbol{\theta}}\bar{\boldsymbol{e}}$ states the rotary inertia for pure rotation about the global inertia frame.

$$\boldsymbol{Q_{inertia}} = \frac{d}{dt}\left(\frac{\partial T}{\partial \dot{\bar{\boldsymbol{e}}}}\right) - \frac{\partial T}{\partial \bar{\boldsymbol{e}}} = \boldsymbol{A_\theta}^T \boldsymbol{M}\boldsymbol{A_\theta}\ddot{\bar{\boldsymbol{e}}} + \boldsymbol{G}\dot{\bar{\boldsymbol{e}}} + \boldsymbol{A_\theta}^T \boldsymbol{M}\ddot{\boldsymbol{A}}_{\boldsymbol{\theta}}\bar{\boldsymbol{e}} \tag{2.16}$$

Here, the mass matrix, $\boldsymbol{M} = \int_V \rho \boldsymbol{S}^T \boldsymbol{S} dV$, then the gyroscopic matrix, $\boldsymbol{G}$ can be stated as,

$$\boldsymbol{G} = \boldsymbol{A_\theta}^T \boldsymbol{M}\dot{\boldsymbol{A}}_{\boldsymbol{\theta}} - \dot{\boldsymbol{A}_{\boldsymbol{\theta}}}^T \boldsymbol{M}\boldsymbol{A_\theta} \tag{2.17}$$

Therefore, no other special treatment for gyroscopic effect needed to be considered in describing the equation of motion for the fully parameterized ANCF beam element in the present model.

2.4 Formulation of Internal and External Forces of the Drill Pipe Model

The generalized viscoelastic force vector, $\boldsymbol{Q_{ve}}$ can be described as,

$$\boldsymbol{Q_{ve}} = -\int_V \left[\left(\frac{\partial \boldsymbol{\varepsilon}}{\partial \boldsymbol{e}}\right)^T \boldsymbol{E}\boldsymbol{\varepsilon} + \left(\frac{\partial \dot{\boldsymbol{\varepsilon}}}{\partial \dot{\boldsymbol{e}}}\right)^T \boldsymbol{D}\dot{\boldsymbol{\varepsilon}}\right] |\boldsymbol{J_0}| \, dV \tag{2.18}$$

where, $\boldsymbol{E}$ represents the elasticity matrix, which contains the Lame constants, λ and μ, $\boldsymbol{\varepsilon}$ and $\dot{\boldsymbol{\varepsilon}}$ are green Lagrange strain tensors. The detailed representation of the elasticity matrix, $\boldsymbol{E}$, and the damping matrix, $\boldsymbol{D}$ were stated in (Htun et al., 2020), by using the stress component as,

$$\boldsymbol{\sigma} = \boldsymbol{E}\boldsymbol{\varepsilon} + \boldsymbol{D}\dot{\boldsymbol{\varepsilon}} \tag{2.19}$$

A generalized equivalent force vector of gravitational force acting on an element can be written as,

$$\boldsymbol{Q_g} = \int_0^1 A_c \cdot l_e (\boldsymbol{G_r})^T \boldsymbol{S}(x, 0, 0)\, d\xi \tag{2.20}$$

A generalized equivalent force vector of buoyancy force acting on an element can be stated as,

$$\boldsymbol{Q_b} = \int_0^1 A_c \cdot l_e (\boldsymbol{B})^T \boldsymbol{S}(x, 0, 0)\, d\xi \tag{2.21}$$

where, A_c is the cross-sectional area of the pipe model, and the length of the element will be l_e and each term of $\boldsymbol{G_r}$ and $\boldsymbol{B}$ represents,

$$\boldsymbol{G_r} = \rho_{pipe}[0 \quad 0 \quad -g]^T, \tag{2.22}$$

$$\boldsymbol{B} = \rho_{water}[0 \quad 0 \quad g]^T \tag{2.23}$$

The generalized force vector for added mass force will be,

$$\boldsymbol{Q_{am}} = -\rho_w A_c C_a l (\int_0^1 \mathbf{S}^{\mathbf{T}} \boldsymbol{D_n} \mathbf{S} d\xi)\, \ddot{\boldsymbol{e}} \tag{2.24}$$

Then, the added mass matrix, $\boldsymbol{M_a}$ can be expressed by,

$$\boldsymbol{M_a} = \rho_w A_c C_a l (\int_0^1 \mathbf{S}^{\mathbf{T}} \boldsymbol{D_n} \mathbf{S} d\xi) \tag{2.25}$$

Here, each term represents the density of water, ρ_w , the added mass coefficient, C_a, length of the drill pipe, l .

The detailed representation of the projection matrix in the normal direction, $\boldsymbol{D_n}$ and the normal component of the acceleration vector, $\dot{\boldsymbol{U}}_{\boldsymbol{n}}$ can be found in (Htun et al., 2022). Then, the generalized external force vector, $\boldsymbol{Q_{ext}}$ of an externally applied force can be expressed as,

$$\boldsymbol{Q_{ext}} = \int_V \boldsymbol{F}_{ext}{}^T \boldsymbol{S} |\boldsymbol{J_0}| dV \tag{2.26}$$

2.5 Viscoelastic Forces of a Three-dimensional ANCF Beam Element

Based on the non-incremental finite element method for large rotation and deformation problems, different approaches for viscoelastic constitutive models have already been

developed in some literature. The ANCF solid element considering the internal viscous damping based on the Kelvin-Voigt model was proposed by (Ma Chao et al., 2016). An internal damping model based on the Rayleigh functions, which account for the linear viscoelastic relations to multiaxial stress, including the terms of material response to deviatoric and dilutional excitations, was developed in (Garcia-Vallejo et al., 2005). Meanwhile, the Poisson's effect was neglected yet in both elastic and viscous terms in this approach to avoid the Poisson locking problems. Therefore, the constitutive equations for isotropic homogenous viscoelastic material which took into account the Poisson's effect were developed by (Htun et al., 2020).

According to the approach of (Htun et al., 2020), a Kelvin-Voigt model that can characterize the material responses to the bulk and deviatoric stresses based on the Rayleigh damping model can be written in (Eq. 2.27 and 2.28),

$$\mathbf{S} = \mathbf{E}_{\mathrm{d}} : \boldsymbol{\varepsilon}_{\mathrm{d}} + \mathbf{D}_{\mathrm{d}} : \dot{\boldsymbol{\varepsilon}}_{\mathrm{d}} = (2\mu_s(1+\upsilon)\mathbf{I}) : \boldsymbol{\varepsilon}_{\mathrm{d}} + (2\mu_s(1+\upsilon)\gamma_d\mathbf{I}) : \dot{\boldsymbol{\varepsilon}}_{\mathrm{d}} \tag{2.27}$$

$$p = E_t\varepsilon_t + D_t\dot{\varepsilon}_t = 3K(1-2\upsilon)\varepsilon_t + 3K(1-2\upsilon)\gamma_s\dot{\varepsilon}_t \tag{2.28}$$

where $\boldsymbol{S}$ and $\boldsymbol{\varepsilon}_d$ are deviatoric stress and strain tensors, $\boldsymbol{E}_d$ and $\boldsymbol{D}_d$ are the elastic and damping coefficients tensors corresponding to the deviatoric stresses, p and ε_t are the dilatational stress and strain, E_t and D_t are the elastic and damping coefficients respective to the dilatational stresses respectively. Then, γ_d and γ_s are the dissipation factors associated with the deviatoric and dilatational stresses and can be estimated analytically. Also, the bulk modulus of the material, K, and the shear modulus, μ_s can be described based on Young's modulus, E and the Poisson's ratio, ν can be expressed in (Eq. 2.29), and the stress components of the viscoelastic material, $\boldsymbol{\sigma}$ can be defined in (Eq. 2.30).

$$K = E/3(1-2\nu)\ ;\ \mu_s = E/2(1+\nu) \tag{2.29}$$

$$\boldsymbol{\sigma} = \boldsymbol{E}\boldsymbol{\varepsilon} + \boldsymbol{D}\dot{\boldsymbol{\varepsilon}} \tag{2.30}$$

where $\boldsymbol{E}$ and $\boldsymbol{D}$ are the elastic and damping matrices, $\boldsymbol{\varepsilon}$ and $\dot{\boldsymbol{\varepsilon}}$ are the Green Lagrange Strain tensor and its time derivative. Then, the equation of motion for the rotating drill pipe model can be written as in (Eq. 2.31), and a total mass matrix, $\boldsymbol{M_T}$ can be stated as in (Eq. 2.32).

$$\begin{bmatrix} \boldsymbol{M_T} & \boldsymbol{\phi_q^T} \\ \boldsymbol{\phi_q} & \mathbf{0} \end{bmatrix} \begin{bmatrix} \ddot{\boldsymbol{q}} \\ \boldsymbol{\lambda} \end{bmatrix} = \begin{bmatrix} \boldsymbol{Q} \\ \widehat{\boldsymbol{\gamma}} \end{bmatrix} \tag{2.31}$$

$$\boldsymbol{M_T} = \boldsymbol{M} + \boldsymbol{M_a} \tag{2.32}$$

Here, $\boldsymbol{M}$ is the constant mass matrix in (Eq. 2.5), and the added mass matrix is $\boldsymbol{M_a}$, and the vector of absolute accelerations, $\ddot{\boldsymbol{q}}$, can be expressed in (Eq. 2.33), and from this acceleration vector, $\ddot{\boldsymbol{q}}$, the expression of the velocity vector, $\dot{\boldsymbol{q}}$ and the displacement vector, $\boldsymbol{q}$ can also be obtained.

$$\ddot{\boldsymbol{q}} = \boldsymbol{M^{-1}Q} - \boldsymbol{M^{-1}\phi_q^T}.\left(\boldsymbol{\phi_q M^{-1}\phi_q^T}\right)^{-1}.(\boldsymbol{\phi_q M^{-1}Q} - \boldsymbol{\gamma}) \tag{2.33}$$

In (Eq. 2.31, and Eq. 2.33), $\boldsymbol{Q}$ represents a generalized external force vector including all external forces, internal damping, and elastic forces, $\boldsymbol{\lambda}$ represents a vector of Lagrange multipliers, $\boldsymbol{\phi_q}$ denotes the Jacobian matrix of the constraints $\boldsymbol{\phi}$ and, $\boldsymbol{\gamma}$ is a quadratic velocity vector and $\widehat{\boldsymbol{\gamma}}$ is the stabilized quadratic velocity vector respectively. The detailed representations of Baumgarte's stabilization technique and constraint formulations were expressed in (Htun et al., 2022).

2.6 Hyper-elastic Material Models in ANCF Simulation

In ANCF simulation, it is crucial to develop an efficient and reliable elastic force model for nonlinear finite element analysis. The elastic force models which account for the coupling between bending and axial deformations using a continuum mechanics approach in ANCF had been developed by (Berzeri and Shabana, 2000), and modeling nonlinear nearly incompressible materials with polynomial Mooney Rivlin models and volumetric energy penalty function was presented by (Orzechowski and Fraczek, 2015), description of elastic force and study on the stiffness properties in ANCF was proposed by (Sopanen and Mikkola, 2003a; 2003b) with the application of fully parameterized ANCF beam element. Here, the strain energy function for the Neo Hookean model, U_{nh} can be expressed as in (Eq. 2.34) and,

$$U_{nh} = \mu_{10}(\boldsymbol{I_1} - 3), (\mu_{10} \neq 0) \tag{2.34}$$

Then, the description of the strain energy function for the incompressible Mooney Rivlin model, U_{mr} can be written as in (Eq. 2.35) according to (Orzechowski and Fraczek, 2015),

$$U_{mr} = \mu_{10}(\boldsymbol{I_1} - 3) + \mu_{01}(\boldsymbol{I_2} - 3) \tag{2.35}$$

where μ_{10} and μ_{01} represent the elastic coefficients, $\boldsymbol{I_1}$, $\boldsymbol{I_2}$ are the variants of the right Cauchy-Green deformation tensor.

Moreover, the detailed consideration of the viscoelastic forces of a three-dimensional ANCF beam element was discussed by (Htun et al., 2020) applying incompressible Mooney Rivlin material model to capture the deformation of the subsea cable with the consideration of the locking phenomenon experienced in 24-DOF ANCF beam element. Based on previous studies, this study applied the two well-known hyper-elastic force models: Neo Hookean and incompressible Mooney Rivlin material models (Mooney, M.A, 1940; Rivlin, R.S, 1948), which are based on strain energy density function and applicable to consider the large deformation problems.

2.7 Consideration of Dissipation Factors for Internal Damping

The literature of (Berzeri and Shabana, 2000; Htun et al., 2020) stated that the dilatational damping factor, γ_d can be assumed as a fraction, ξ (damping constant) of its critical value for a pure deviatoric (torsion) test case. Thus, γ_d can be expressed in (Eq. 2.36).

$$\gamma_d = \xi\gamma_d^{crit}, \gamma_d^{crit} = \frac{2}{\omega_n^d} \tag{2.36}$$

Here, ω_n^d is the torsional natural frequency and the first natural frequency can be calculated as in (Eq. 2.37),

$$\omega_n^d = \frac{\alpha}{L}\sqrt{\frac{C_t\mu_s}{\rho I_p}} \tag{2.37}$$

where $\alpha = \frac{\pi}{2}$, ρ is the material density, μ_s is the shear modulus, I_p is the polar moment of the cross-section, and L is the beam length. Here, C_t is the torsion factor and it can be written for circular cross-section with radius, r as in (Eq. 2.38),

$$C_t = \frac{\pi r^4}{12} \tag{2.38}$$

Since the volumetric dissipation factor γ_s can be determined from pure bending axial stress only, the axial stress, σ_{xx} can be expressed in (Eq. 2.39) and the dissipation factor, γ_{xx} can also be expressed in (Eq. 2.40).

$$\sigma_{xx} = E\varepsilon_{xx} + D\dot{\varepsilon}_{xx} = E\varepsilon_{xx} + E\gamma_{xx}\dot{\varepsilon}_{xx} \tag{2.39}$$

$$\gamma_{xx} = \xi\gamma_{xx}^{crit},\ \gamma_{xx}^{crit} = \frac{2}{\omega_n^b} \tag{2.40}$$

Also, the bending natural frequency can be determined as in (Eq. 2.41),

$$\omega_n^b = \frac{\beta}{L}\sqrt{\frac{EI}{mL}} \tag{2.41}$$

where β is a constant of the nth mode of vibration and boundary conditions, E is Young's modulus, and I is the second moment of area, L is the beam length and m is the beam mass respectively. According to (Htun et al., 2020), the relationship between γ_{xx}, γ_d and γ_s with the influence of Poisson's ratio will become in (Eq. 2.42) and neglecting the Poisson's effect can be stated in (Eq. 2.43), K is the bulk modulus and μ_s is the shear modulus with the same representations in (Eq. 2.29).

$$\gamma_{xx} = \frac{3K\gamma_d + \mu_s\gamma_s}{3K + \mu_s} \tag{2.42}$$

$$\gamma_{xx} = \frac{2\gamma_d + \gamma_s}{3} \tag{2.43}$$

Chapter 3

Experimental Study of the Underwater Behavior of the Rotating Drill Pipe Model in Uniform Flow

3.1 Experimental Setup of the Drill Pipe Model

The model test was conducted at Osaka University's towing tank with dimensions ($L \times B \times D$ = 100 m × 7.8 m × 4.35 m), as illustrated in Fig. 3.1. To investigate the underwater behavior of the drill pipe during the drilling operation in the tidal currents, a temporary bottom measuring 3 meters deep ($L \times B$ = 1.2 m × 0.9 m) was affixed to the towing carriage, along with a guide pipe. This temporary bottom was suspended by four 50 mm square aluminum columns, each covered with NACA0024 airfoils featuring a 300 mm chord length. This design aimed to mitigate the formation of the Karman vortex from the columns and minimize the drag, as shown in (Fig. 3.1).

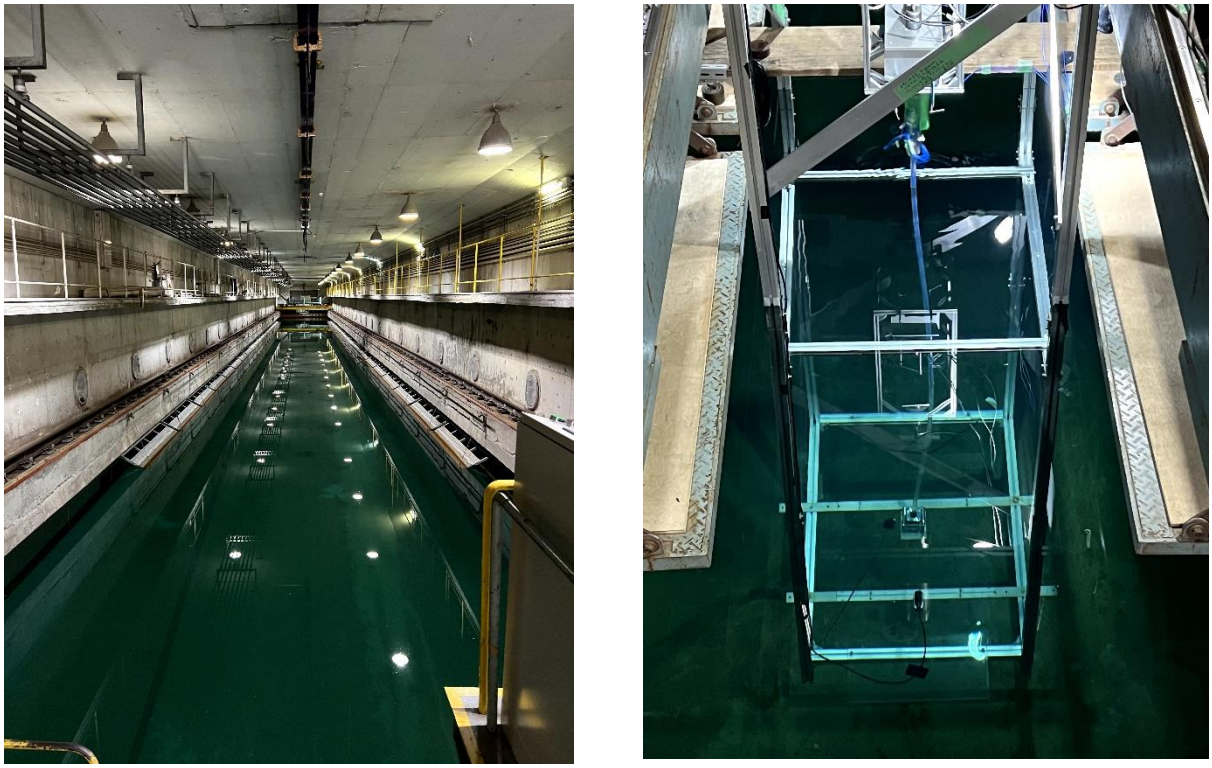

Fig. 3.1 Experimental towing tank and the experimental setup of the drill pipe model

The experimental setup schematic is described in (Fig. 3.2). A rotating mechanism containing a drill pipe model was attached to a four-channel load cell (measuring *Fx*, *Fy*, *Mz*, and *My* forces), which, in turn, was connected to the oblique shaft mounted on the

towing carriage. The lower end of the drill pipe model was inserted into a guide pipe secured at the temporary bottom, as detailed earlier.

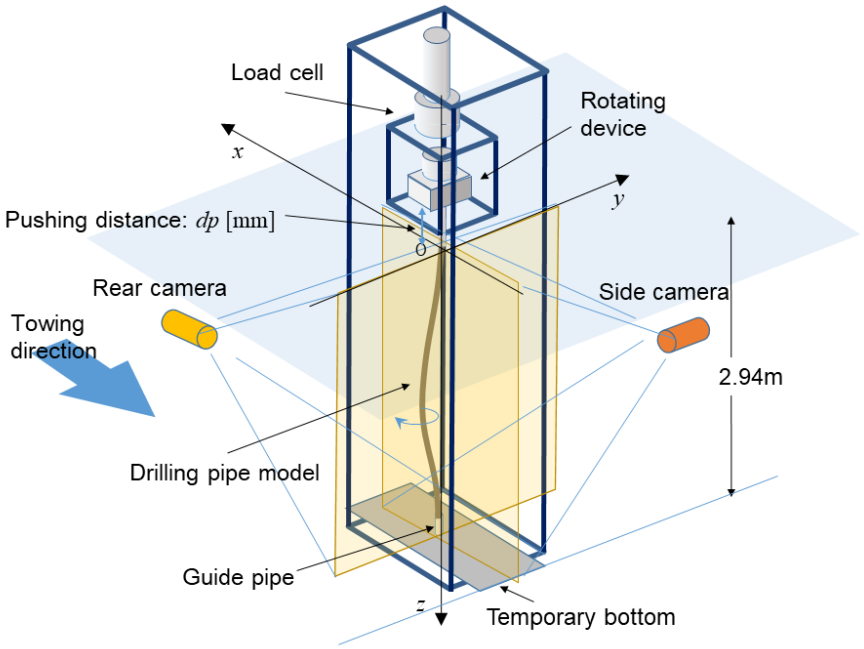

Fig. 3.2 The schematic diagram of the experimental apparatus

The upper end of the drill pipe model is directly linked to the rotating shaft, which in turn connects to the motor via a reduction gear. The rotation of the drill pipe model was controlled by the rotating motor. Then, the bottom end of the drill pipe model is inserted into the guide pipe and the bottom position moves vertically in the *z*-direction. since the lower end of the drill pipe model was only controlled by the movement in the horizontal plane (*x*-*y* direction) and the restriction of the rotation or vertical displacement (*z*-axis) of the drill pipe model, depending on the positioning of the top end of the drill pipe model, its bottom end moves vertically in the *z*-direction accordingly.

For monitoring and measuring the underwater behavior of the drill pipe model, two underwater cameras were set up at the apparatus's side and rear (referred to as side and rear cameras, respectively). The side camera tracks displacements in the *x*-direction (aligned with the uniform flow), while the rear camera observes movements in the *y*-direction (90° lateral to the uniform flow). To prevent interference from wakes or waves generated by the camera or its supports, the rear camera is positioned behind the drill pipe model.

The coordinate system's origin is situated at the intersection of the drill pipe model and the water surface. The downward vertical direction, opposite to the towing carriage's motion, and the cross product of these two directions are defined as z, x, and y, respectively. Drill pipe model displacement data were gathered through analysis of images captured by the side and rear cameras. Additionally, hydrodynamic force components in the x and y directions were measured from the load cell output. The drill pipe model, comprising two φ = 19.05 mm Teflon pipes connected to form a 3.155 m length, is detailed in Table 1.

Under these conditions, the drill pipe rotates within the uniform flow, enabling observation and measurement of the hydrodynamic forces acting on the pipe model. Then, the displacement of the drill pipe model was obtained by analyzing the images acquired by the side and rear cameras. In contrast, from the output of the load cell, the hydrodynamic force components in the x and y directions were measured. Two ϕ = 19.05[mm] Teflon pipes, which are 1.405 and 1.75[m] long, were connected to form a 3.155[m] drill pipe model.

The principal particulars of the drill pipe model are summarized in Table 1. In this condition, the drill pipe is rotated in a uniform flow, and the hydrodynamic force acting on the whole apparatus and the behavior of the drill pipe model were observed and measured.

Table 3.1 Principal particulars of the drill pipe model

Material	Teflon
Length L [m]	3.155
Diameter: D_o [mm] (outer) D_i [mm] (inner)	19.05 15.88
Density ρ_p[g/cm^3]	2.12~2.20
Young's modulus E[GPa]	0.640

Furthermore, (Suzuki et al., 2022) have thoroughly analyzed and discussed the detailed setup and experimental results of this study, with a comparison numerical study of the non-rotating analytical pipe model in ANCF simulation.

3.2 Experimental Conditions of the Drill Pipe Model

In this measurement setup, alterations were made to both the uniform flow velocity and the rotation speed of the model drill pipe. While WOB (weight on bit) is a critical parameter in actual drilling, its measurement poses challenges, particularly in the longitudinal direction (z-direction) of the model drill pipe. Consequently, we opted to vary the pushing distance (dp) of the model drill pipe a change in the distance from the water surface to the top of the model drill pipe. Increasing dp allows for the simulation of larger WOB in a static state. However, during uniform flow and rotation, the model drill pipe undergoes deformation, raising uncertainties about whether its lower end maintains contact with the base of the guide pipe. Despite these challenges, we selected and applied three dp values for the measurement.

The model drill pipe, with a length of 3.155 m, is positioned above a temporary bottom set at a depth of 2.94 m. However, the bottom of the guide pipe is situated 45 mm above the temporary bottom, ensuring contact with the model drill pipe. Under these conditions, when the model drill pipe is inserted into and secured within the guide pipe, its upper end rests 0.26 m above the water surface (z = -0.26 m). At this position, where the upper end is supported, the WOB is zero. This specific position serves as the origin for the pushing distance dp (dp = 0 mm). As dp is increased from this state, static WOB is applied. These measurement conditions are outlined in Table 3.2.

In this measurement, both the uniform flow velocity and the rotation speed of the drill pipe model were varied, as summarized in Table 3.2. For the present measurement setup, the Reynolds numbers (Rn) concerning the diameter of the drill pipe model range approximately in 2000, 4000, and 6000 for flow velocities U of 0.1 m/s, 0.2 m/s, and 0.3 m/s, respectively. In practical drilling operations, the WOB (weight on bit) stands as a crucial parameter. While this measurement also considers changes in WOB, currently, there's no direct method to gauge the force along the longitudinal (axial) direction (z-direction) of the drill pipe model.

Table 3.2 Experimental conditions of the drill pipe model

Inflow Velocity, U [m/s]	0, 0.10, 0.20, 0.30
Number of Revolution, n [rpm]	0, 100, 200, 250, 300
Pushing distance, dp [mm]	0, 85, 115
Reynold Number ($Rn=UD_o/\nu$)	2000,4000,6000

Hence, the pushing distance (dp) of the drill pipe model was adjusted to a variation in the distance from the water surface to the top of the drill pipe model. Increasing the dp value allows for a larger simulated WOB under static conditions. However, during uniform flow and rotation, the drill pipe model undergoes deformation, and it's uncertain whether the lower end maintains contact with the base of the guide pipe. Nevertheless, despite these challenges, three dp values were selected and applied in the measurement.

The drill pipe model measures 3.155 m in length, with a temporary bottom set at a depth of 2.94 m. The bottom of the guide pipe rests 45 mm above the temporary bottom and is in contact with the drill pipe model. Under these circumstances, when the drill pipe model is inserted and secured within the guide pipe, its upper end sits 0.26 m above the water surface (z = -0.26 m). As the upper end is supported at this position, the WOB reduces to zero. Additionally, this position serves as the reference for the pushing distance, dp (dp = 0 mm). If dp increases from this state, the initial WOB is statically applied. Notably, the actual drill pipe typically has a diameter of about 5-6 inches, with a rotational speed ranging from approximately 60 to 150 rpm as mentioned in, (Suzuki et al., 2022).

3.3 Measurement Results of the Drill Pipe Model

The drill pipe model restricts the displacement of the upper end in all directions and the planar displacement of the lower end, making it challenging to measure the hydrodynamic force acting solely on the drill pipe model. However, in the current measurement setup, the rotating device is suspended on a load cell, enabling the measurement of the force exerted on the drill pipe rotating device. Consequently, the measured forces encompass not only the hydrodynamic force acting on the drill pipe

model but also the force acting on the lower end of the drill pipe model to constrain its displacement. To measure the displacement of the drill pipe model, we employed image analysis utilizing three-dimensional position analysis software. This software facilitates three-dimensional image analysis by capturing images from two different directions. Measurements were obtained by capturing images of markers positioned on the drill pipe model at intervals of 0.1 m.

The time-averaged non-dimensional forces acting on the model drill pipe rotating device are illustrated in (Fig. 3.3). If the forces in the x and y directions acting on the model drill pipe rotating device are denoted as *Fx* and *Fy*, respectively, their non-dimensional values, *CFx* and *CFy*, can be expressed as follows.

$$C_{Fx} = F_x / 0.5\rho U^2 S_n,\ C_{Fy} = F_y / 0.5\rho U^2 S_n \qquad (n = 1,2,3) \tag{3.1}$$

Where S_n (n=1,2,3) means the projected area of the submerged part of the model drill pipe in the *y-z* plane in the static state for each *dp*.

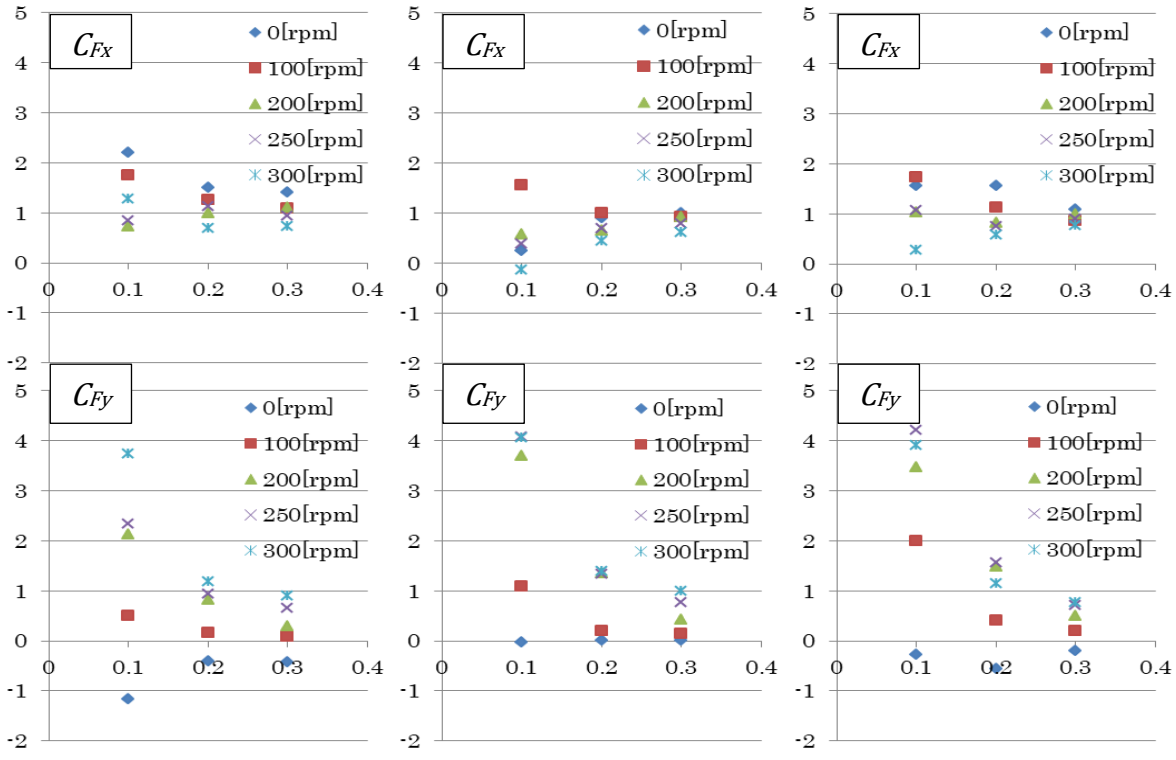

a) *dp*=0[mm] b) *dp*=85[mm] c) *dp*=115[mm]

Fig. 3.3 Hydrodynamic coefficients acting on the rotating device of the drill pipe model

The coefficient, *CFx*, inclusive of the drag component acting on the model drill pipe, tends to decrease as rotation speed increases, converging to a constant value with higher flow velocities. The behavior observed in *CFy* is related to the lift force attributable to the Magnus effect, contingent upon the rotation ratio defined by $r\omega/U$. As per existing knowledge (Hoerner, 1985), the larger the rotation ratio, the greater the lift coefficient. It is presumed that the lift coefficient varies with the rotation ratio, defined as $r\omega/U$.

The displacement of the model drill pipe in the *x*, and *y* direction may exhibit minimal variation, although there might be some alterations due to changes in the submerged length of the model drill pipe resulting from adjustments in the pushing distance *dp*. Indeed, it's accurate to acknowledge that the force in the *z*-direction wasn't measured, and the hydrodynamic force acting specifically on the model drill pipe wasn't separately assessed. Moreover, this initial displacement of the drill pipe model in uniform flow is described in (Fig 3.4).

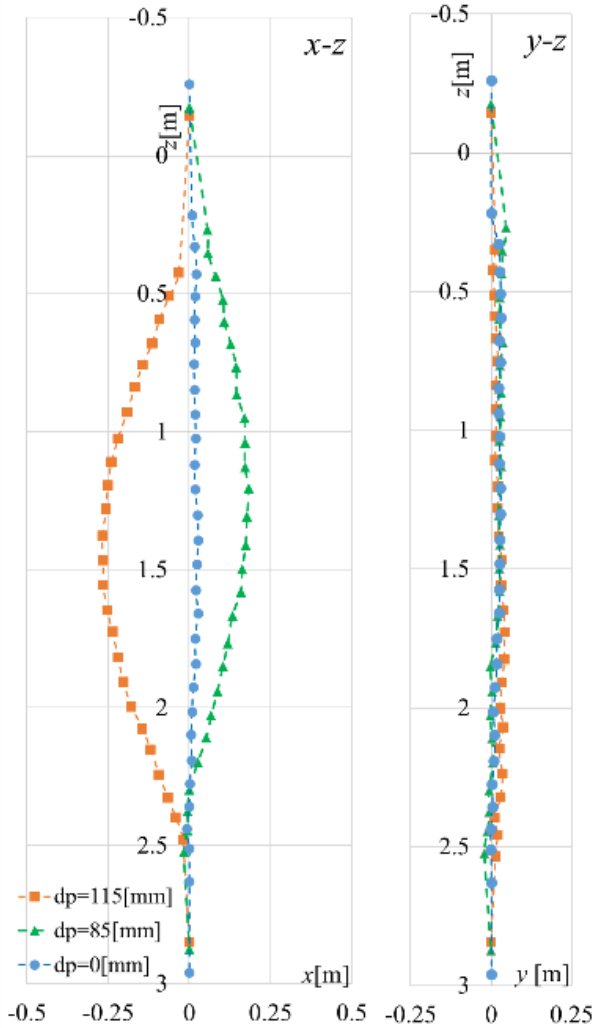

Fig. 3.4 Initial displacements of the drill pipe model in uniform flow

3.4 Underwater Behavior of the Drill Pipe Model in Uniform Flow

The displacement of the model drill pipe was observed and measured while varying the uniform flow velocity *U*, rotation speed *n*, and pushing distance *dp*, as previously described. Here, (Fig. 3.5) illustrates the displacement of the model drill pipe under uniform flow velocity conditions in the non-rotating state. Specifically, in the scenario with *U*=0.3 m/s and *dp*=0 mm, the model drill pipe became dislodged from the guide pipe and hung off. To prevent such occurrences, an appropriate *dp* value of *dp*=115 mm was set to ensure the model drill pipe remained engaged with the guide pipe, enabling subsequent observation and measurement.

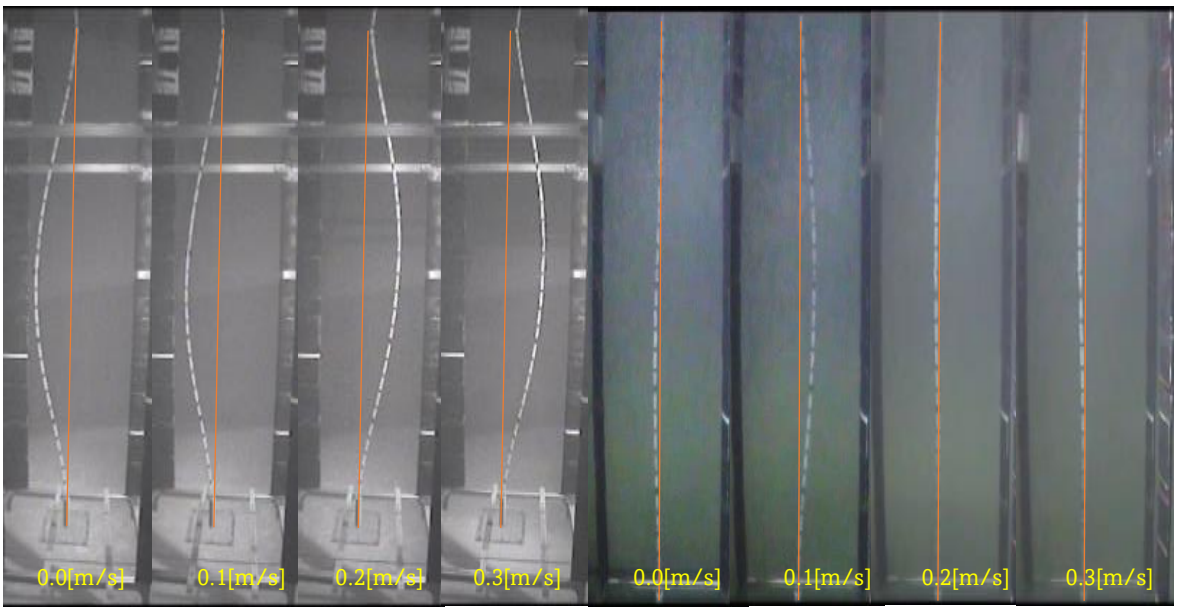

(a) *x*-displacement (b) *y*-displacement

Fig. 3.5 Photos of the underwater behavior of the drill pipe model without rotation

The images captured by the side camera reveal that initially, the model drill pipe experiences upstream displacement. Notably, the *x*-displacement is slightly smaller compared to the *U*=0.0 m/s case. As the uniform flow velocity increases, such as at *U*=0.2 m/s, the model drill pipe flexes in the downstream direction, with the flexion becoming more pronounced at *U*=0.3 m/s. However, the lateral displacement remains minimal across all cases, as observed in the images from the rear camera. (Fig. 3.7 and 3.9) illustrate the behavior of the model drill pipe during rotation at n=250 rpm for *dp*=0 mm and 85 mm, respectively. Interestingly, while hang-off phenomena occurred in the non-rotating condition at U=0.3 m/s and *dp*=0 mm, the same condition under rotation did not lead to hang-off phenomena.

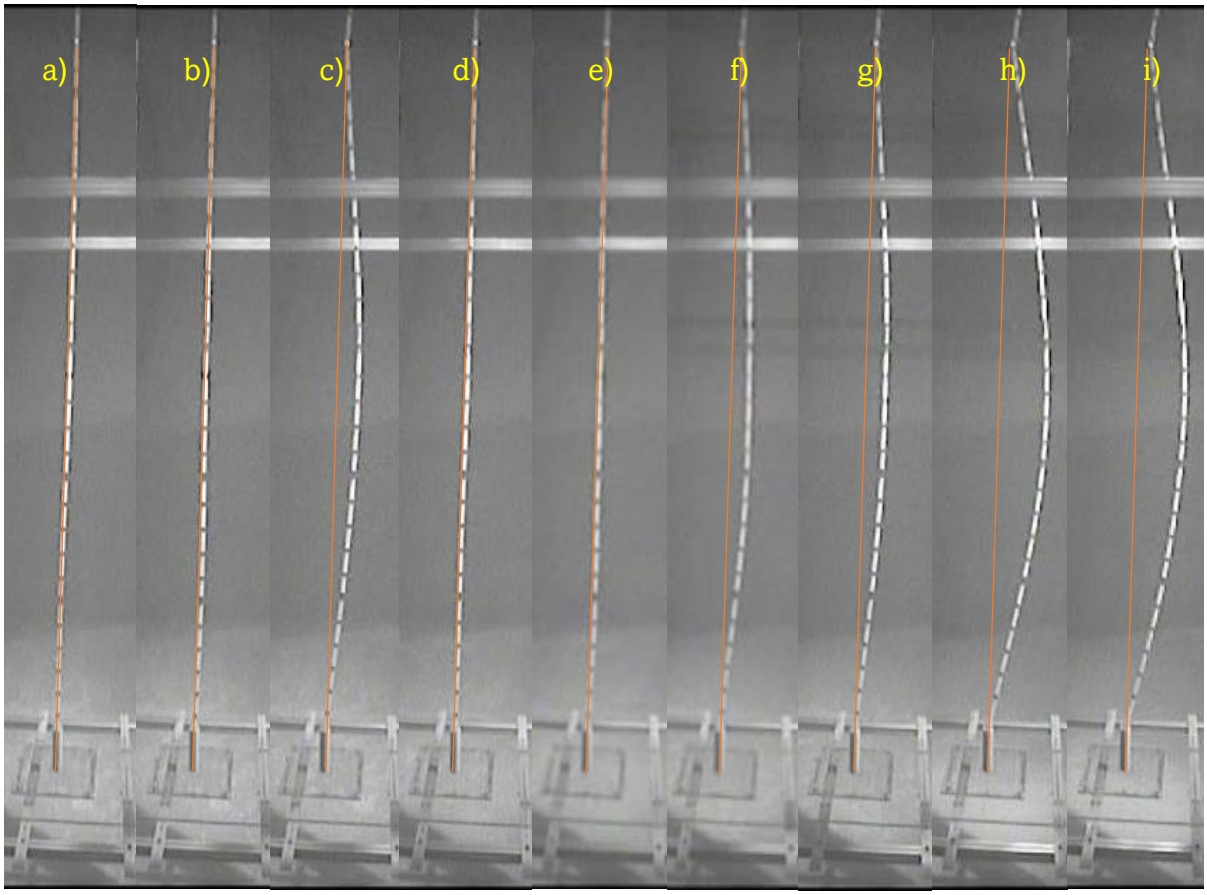

Fig. 3.6 Images captured by side camera (*x*-displacement) for *dp*=0 mm

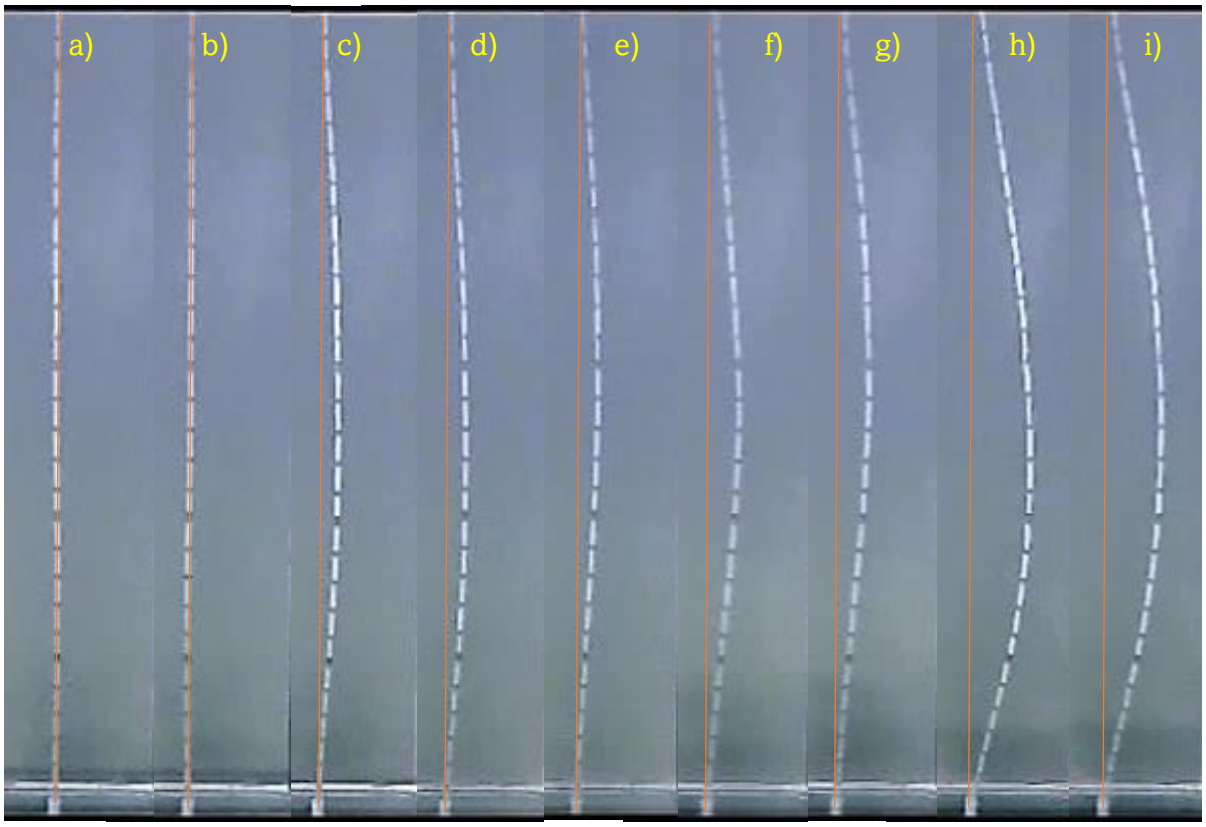

Fig. 3.7 Images captured by rear camera (*y*-displacement) for *dp*=0 mm

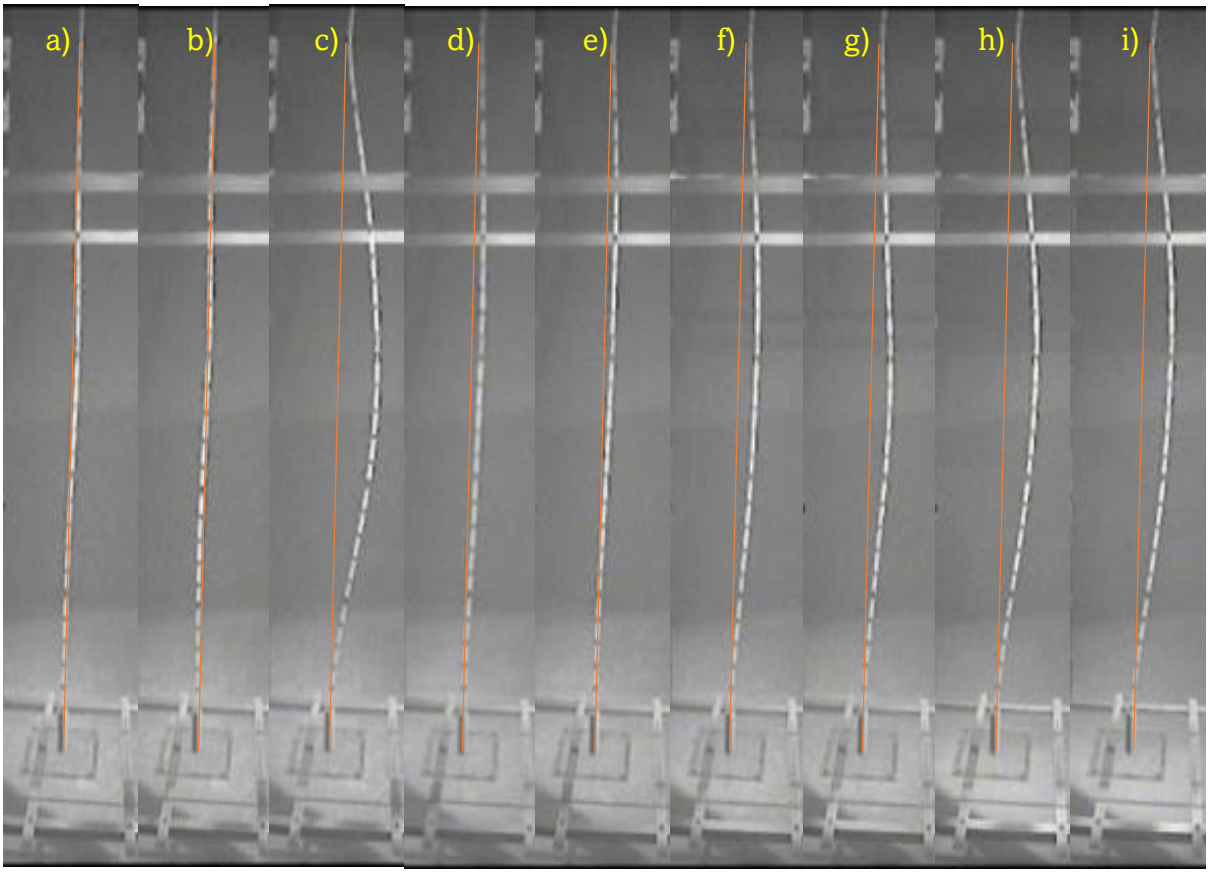

Fig. 3.8 Images captured by side camera (*x*-displacement) for *dp*=85 mm

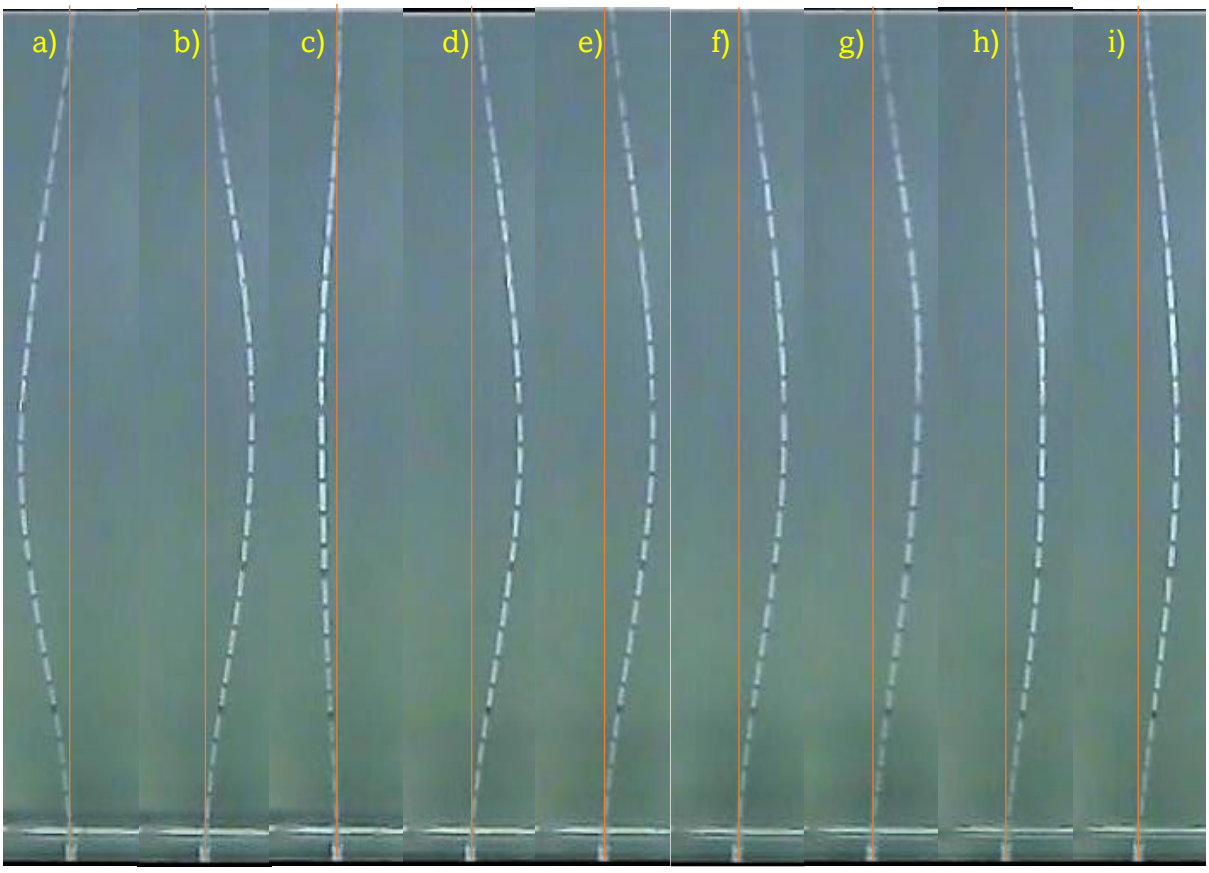

Fig. 3.9 Images captured by rear camera (*y*-displacement) for *dp*=85 mm

As the uniform flow velocity U increases, the x-displacement increases, while the y-displacement tends to decrease. This is also consistent with the trend of C_{Fx} and C_{Fy} shown in (Fig. 3.3). It should be noted that for dp=115[mm] when the uniform flow velocity U is zero, swing-around phenomena do not occur at any rotation speed. The experimental observation involved the investigation of the model drill pipe's displacement under varying uniform flow velocity (U), rotation speed (n), and pushing distance (dp) conditions. The analysis incorporated observations captured by a side camera while the towing carriage's speed increased incrementally from 0 m/s to 0.3 m/s while maintaining rotation speed. The selected images represented distinct stages of motion, including stationary, accelerating, and steady-state conditions.

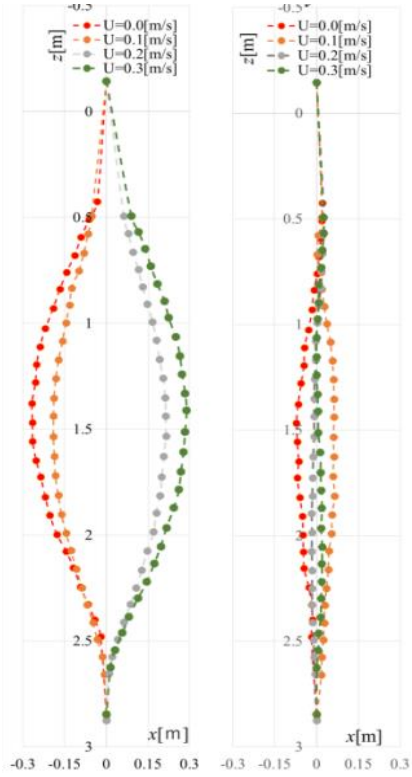

Fig. 3.10 Underwater behavior of the drill pipe model in different flow velocities

For instance, in the case of dp=0 mm (Fig. 3.6 and 3.7), it was observed that both x and y displacements increased with higher flow velocities. However, under constant velocity, x-displacement was minimal, with a predominance of y-displacement. Conversely, for dp=85 mm (Fig. 3.8 and 3.9), it was inferred that when both the fluid and the model drill pipe were stationary, the lower end contacted the guide pipe base, generating WOB. The rotation of the model drill pipe induced swing-around phenomena, with maximum x-displacement occurring during acceleration, and y-deformation opposite to the final state.

As flow velocity increased, *x*-displacement increased while *y*-displacement was more pronounced at *U*=0.1 m/s than at *U*=0.3 m/s. Additionally, single-node oscillations, possibly involving Vortex-Induced Vibration (VIV), were observed in all flow velocity cases, suggesting non-steady-state motion despite reaching a deformed state. Further analysis in (Fig. 3.10) revealed that under non-rotating conditions, only *x*-displacement due to resistance was evident, with negligible lift force effects. Interestingly, despite reaching a deformed state, the absolute value of deformation at *U*=0.3 m/s remained comparable to initial states, possibly indicating WOB influence. Subsequent measurements (Fig. 3.11) demonstrated that varying *dp* did not significantly affect model drill pipe displacement, suggesting insensitivity of the motion to *dp* variations.

The investigation indicated distinct trends concerning displacement response to changes in flow velocity and rotation speed. Specifically, x-displacement tended to increase with increasing flow velocity while decreasing or remaining stable with increasing rotation speed. Conversely, y-displacement showed an opposite trend, peaking at *U*=0.1 m/s, possibly due to the larger rotation ratio at this velocity, resulting in a higher lift coefficient. Overall, *y*-displacement tended to surpass *x*-displacement across varying conditions, attributed to the influence of the rotation ratio on lift coefficient magnitudes.

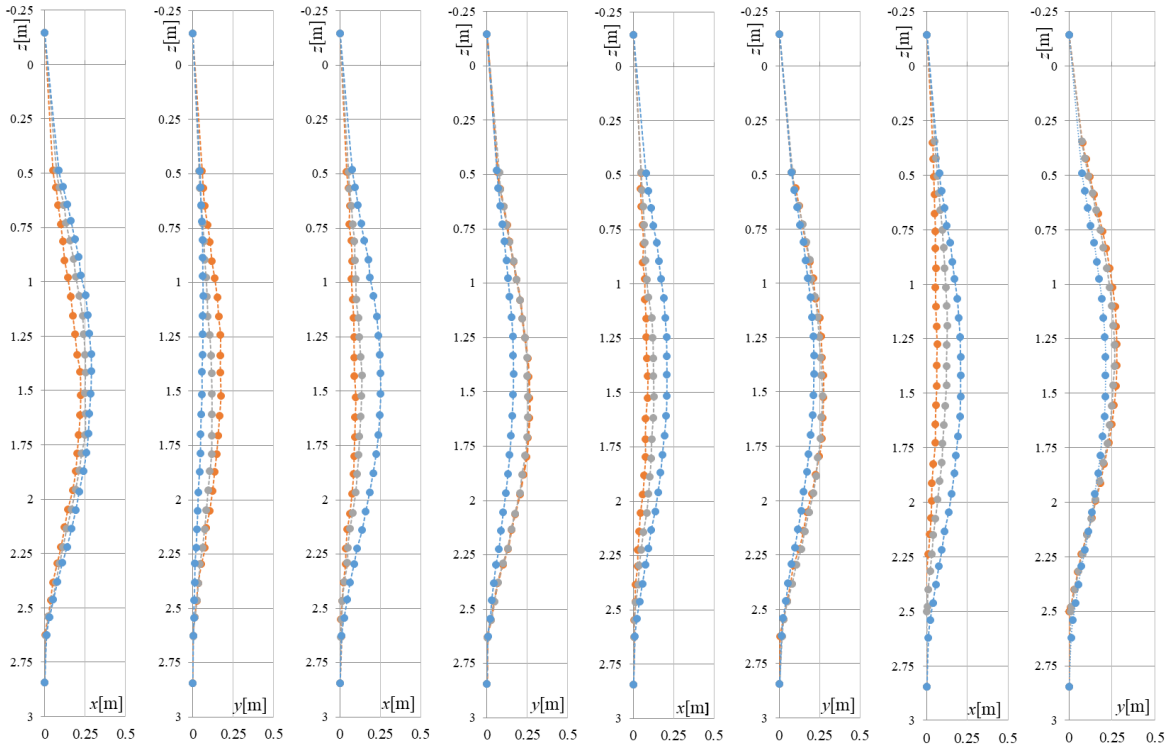

a)n=100[rpm] b)n=200[rpm] c)n=250[rpm] d)n=300[rpm]

Fig. 3.11 Underwater behavior of the rotating drill pipe model in uniform flow

Chapter 4

Estimation of Hydrodynamic Force Exerted on the Rotating Drill Pipe Model

During drilling operations, the drill pipe was directly exposed to the ocean current, and the hydrodynamic forces generated from the current were exerted on the surface of the drill pipe. In previous studies, the lift and drag forces were estimated based on the two-dimensional rotating cylinder in which forces were exerted normally to the surface of the pipe (Inoue et al., 2019), and the hydrodynamics forces acting on the drill pipe were estimated in terms of tilt and oblique angles related to a flow direction of the drill pipe model (Suzuki et al., 2020, 2022) and applied to the non-rotating drill pipe model in the previous study. In this study, the modification of the hydrodynamic forces exerted on the rotating drill pipe model was analyzed and discussed in, (Tun et al., 2023) ; (Koga, 2022) and it will be introduced in further detail in this chapter.

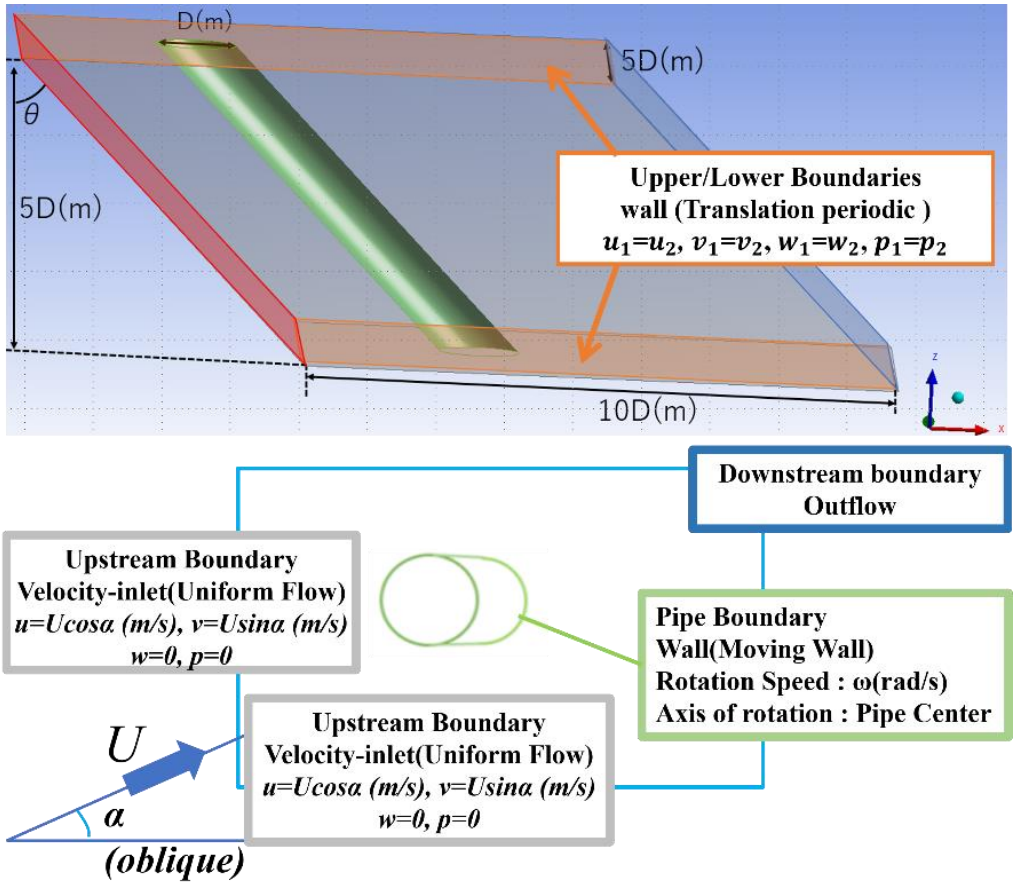

Fig. 4.1 Boundary conditions for the CFD analysis in the previous study

4.1 Computational setup for CFD analysis in previous study

In this study, the computational fluid dynamics (CFD) software, ANSYS Fluent 2020 R2 was used to estimate the fluid forces exerted on the drill pipe model. The *SST k-ω* was used as a turbulent model and the inflow velocity, U was 0.3 m/s for uniform flow consideration. These calculation conditions and the setting for the tilt angle, θ, and the oblique angle, α are shown in (Table 4.1) and (Fig. 4.1).

Table 4.1 Solver condition and computational conditions in CFD analysis

CFD code	ANSYS Fluent 2020 R2
Turbulence model	*SST k-ω*
Inflow velocity U [m/s]	0.300
Number of Revolution ω [rad/s]	26.46 (250 rpm)
Rotation ratio ($r\omega/U$)	0.84
Reynold Number, *Rn*	6000(0.3 m/s)
θ (degree)	-20, -10, 0, 10, 20, 30
α(degree)	-10, 0, 10, 20, 30, 40

The other boundary conditions applied in this study are shown in (Fig. 4.1). The computational domain for the drill pipe model was considered as the ($10D$ x $5D$ x $5D$) as shown in Fig. 4.1, here, D means the diameter of the pipe model.

Since it may be challenging to properly set up the normal, tangential, and bi-normal components of the deformed drill pipe model stated in the previous study (Suzuki et al., 2022), the absolute coordinates as mentioned in x, y, and z coordinates were used to define the three-dimensional hydrodynamics force model for this work. The hydrodynamic force results obtained from the variation of the orientation of the pipe, the tilt angle θ, and oblique angles, α, were shown in (Fig. 4.2).

4.2 Estimation of Hydrodynamic Forces of the Drill Pipe Model (Previous Study)

According to the hydrodynamic force calculation results shown in (Fig. 4.2), it can be found that F_x tends to decrease as the oblique angle increases, F_y tends to increase as the oblique angle increases, and both fluid forces in x and y components have less dependency on tilt angle, θ. In contrast, F_z is dependent on both the oblique and the tilt angle, and it can be found that the fluid force values tend to increase both the tilt and oblique angle increase.

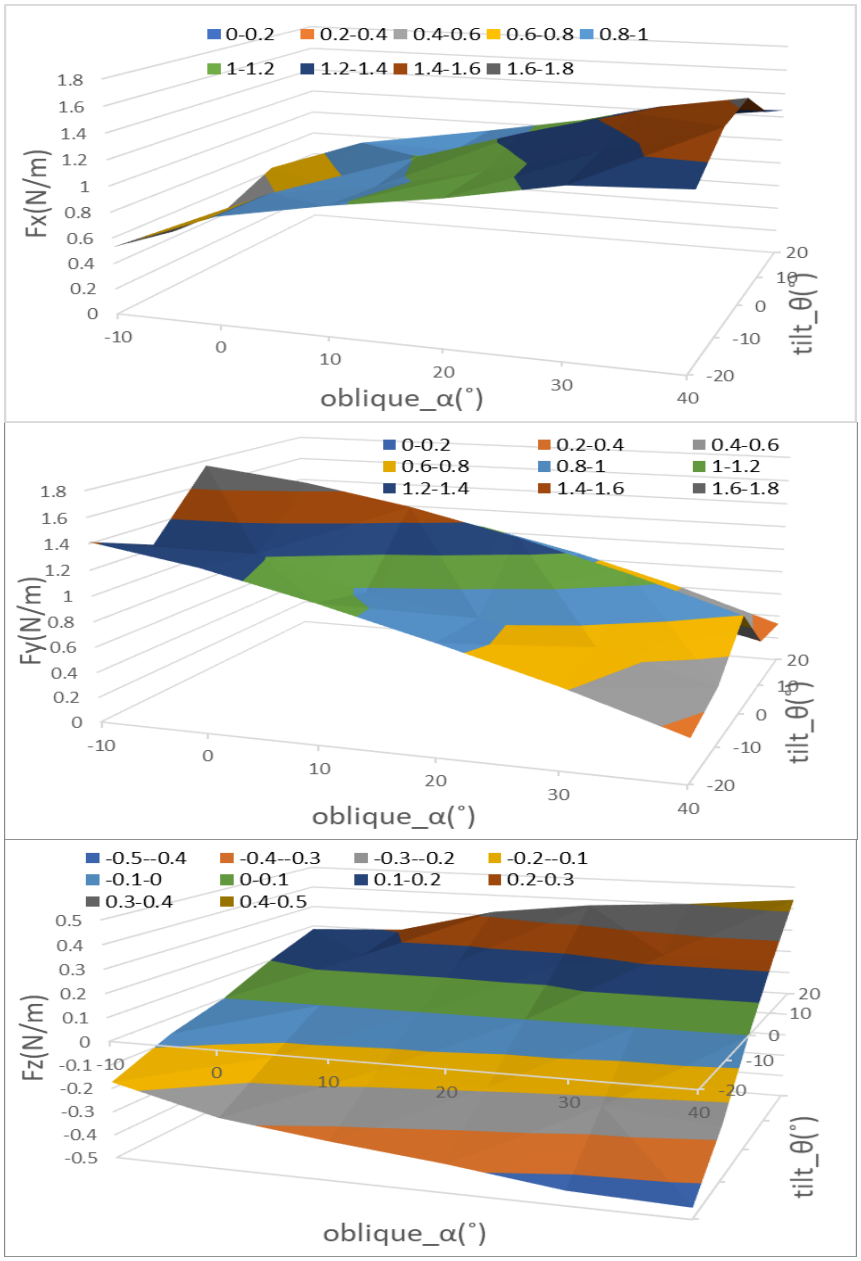

Fig. 4.2 Previous Study's hydrodynamic force distribution (U=0.3m/s, 250rpm with counterclockwise rotation)

4.3 Estimation of Hydrodynamic Force for Rotating Drill Pipe Model (Current Study)

4.3.1 Modification of the Computational Domain for the Drill Pipe Model

In this study, the boundary conditions for ANSYS Fluent analysis only focus on the length and breadth of the boundaries since the important parameters for flow velocity and pipe boundaries are based on these two parameters of the computational domain. Compared to previous studies, the computational domain was doubled in the *x* direction, tripled in the *y* direction, and halved in the *z* direction in this study. As for the change in the *x* and *y* directions, it was considered that the length from the rotating cylinder to the outflow boundary would not be sufficient when the oblique angle increased. Moreover, to reduce the calculation time for this calculation, a shorter length in *z*-direction was proposed in this study. For the drill pipe model, the length of the pipe model could be several meters long and the setting height could be changed properly based on our drill pipe model consideration as shown in Fig. 4.3.

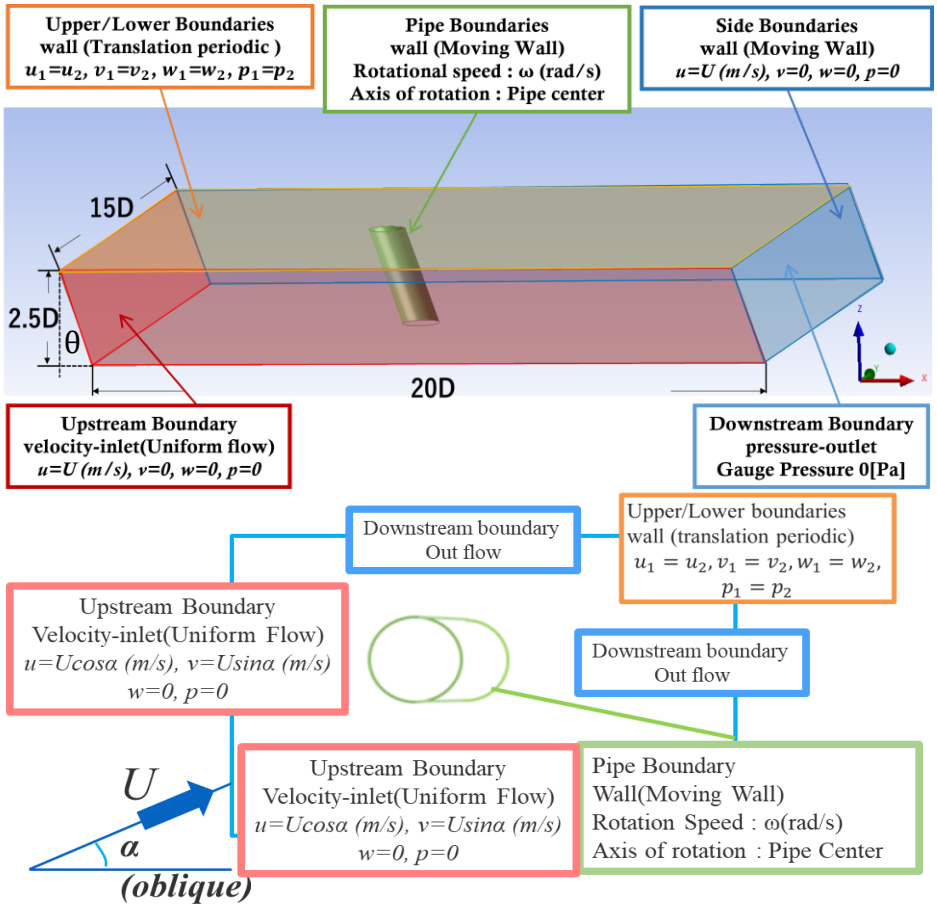

Fig. 4.3 Boundary conditions for the current hydrodynamic force consideration

4.3.2 Modification of the Geometry of the Drill Pipe Model (Element Number and Meshing around the Pipe)

Based on previous studies, the hydrodynamic force estimation for a three-dimensional tilt-oblique rotating cylinder measured with respect to the flow direction was developed by (Suzuki et al., 2022). We applied this approach to the drill pipe underwater behavior estimation program and the validations against the numerical and experimental results were shown in (Tun et al., 2023). In this study, the estimation of three-dimensional hydrodynamic force was performed by using the new computational domain as shown in (Fig. 4.3) in the computational fluid dynamic (CFD) analysis. The calculation was carried out by ANSYS Fluent 2020 R2 and SST k-ω was used as the turbulence model as in the previous study. The computational parameters for this calculation are shown in Table 2.

Table 4.2 Solver condition and computational conditions for the drill pipe model

CFD Code	ANSYS Fluent 2020 R2
Turbulence model	SST k-ω
Inflow velocity U [m/s]	0.300
Reynold Number, Rn $(\approx)$	6000
Number of Revolution ω [rpm]	200, 250, 300
Rotation ratio ($r\omega/U$)	0.84
Tilt angle θ (degree)	-20, -10, 0, 10, 20, 30
Oblique angle α (degree)	-10, 0, 10, 20, 30, 40

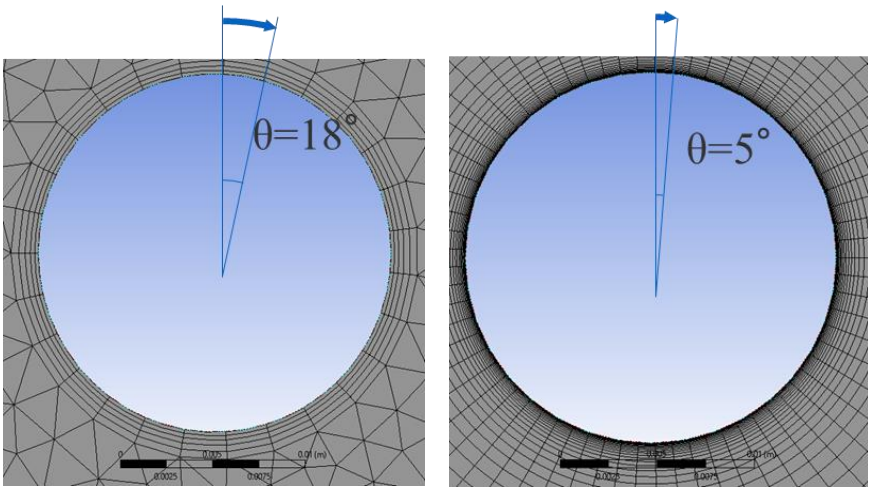

Fig. 4.4 Boundary layer mesh diagram for previous and current studies of the pipe model

Table 4.3 Comparison of the calculation conditions of the drill pipe model in ANSYS Fluent

Particulars	Previous	Present
Element Size	1.80×10^{-2}m	4.00×10^{-3}m
Element Order	2nd order	2nd order
Growth rate	1.20	1.20
Maximum size	3.61×10^{-2}m	8.00×10^{-3}m
Feature removal size	9.03×10^{-5}m	2.00×10^{-5}m
Supplement curvature	Yes	Yes
Minimum size of curvature	1.80×10^{-4}m	4.00×10^{-5}m
Curvature normal angle	18.0°	5.0°
Average surface area	2.86×10^{-2}m^2	4.08×10^{-2}m^2
Minimum side length	6.18×10^{-2}m	5.09×10^{-2}m
Target skewness	0.90	0.90
smooth	middle	middle
Height of the first tier	2.00×10^{-4}m	2.00×10^{-5}m
Maximum number of layers	5	30
growth rate	1.2	1.2
Rigid body behavior	Dimensionally reduced	Dimensionally reduced
Triangular Surface Mesher	Programmatic control	Programmatic control
Pinch Tolerance	1.63×10^{-4}m	3.60×10^{-5}m
node	412724	706588
element	154300	244890

As shown in Tables 4.3 and Fig. 4.4, increasing the number of meshes in the circumferential direction and number of elements for the rotating drill pipe model was provided in this study. Since the boundary layer mesh was made finer than in the previous

study, in order to represent the position of the node point of the pipe model accurately the deformed shape of the pipe model will be precisely configured in this study.

4.3.3 Computational Results for Different Rotational Velocities of the Drill Pipe Model

From these computational setups and parameters, we studied the flow around the tilt-oblique rotating cylinder as shown in (Fig. 4.5). As the deformed drill pipe was still difficult to mention in normal, tangential, and binormal components stated in (Suzuki et al., 2022), the hydrodynamic force was defined as the absolute coordinates x, y, and z in this computation. From the different orientations of the angles, the hydrodynamic force results were obtained respectively.

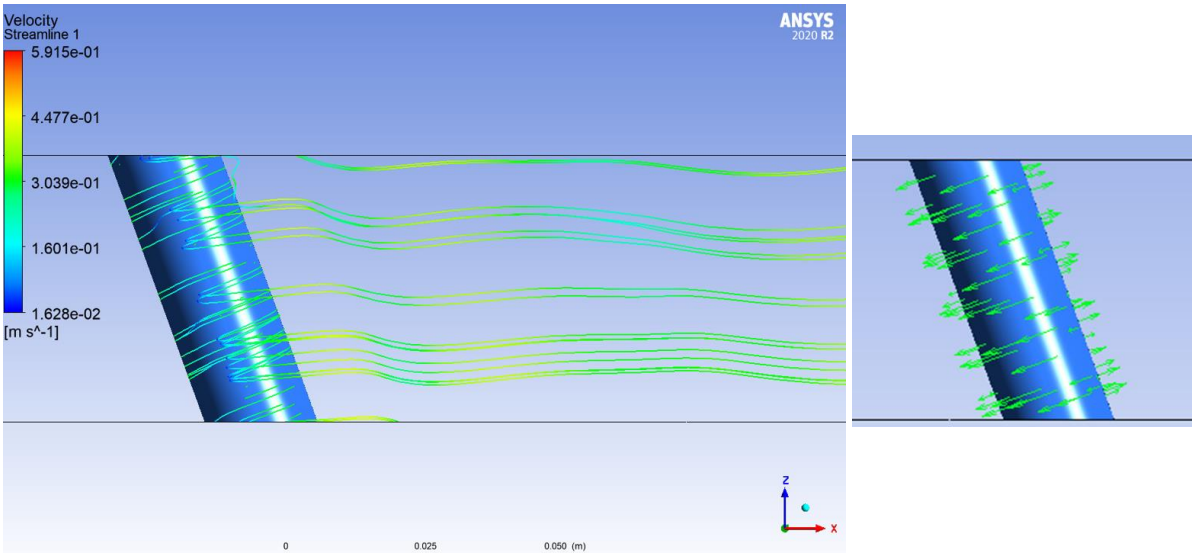

Fig. 4.5 Streamlines flow around the tilt-oblique rotating cylinder

The hydrodynamic force results for the 200,250 and 300 rpm of the rotating drill pipe model were described in (Fig. 4.6, 4.7, and 4.8) for counterclockwise rotation and Fig. 4.9 shows the 250-rpm rotation with a clockwise direction. From these figures, the dependencies of the hydrodynamic force in the x and y directions were observed with the oblique angle, α, and the less dependency with the tilt angle, θ. Meanwhile, the hydrodynamic force in the z direction showed the dependency on both the oblique angle, α, and tilt angle, θ.

Based on the computational results of hydrodynamic force distribution, the forces corresponding to the tilt and oblique angles were obtained through the interpolation function by using the least square method. From this hydrodynamic force distribution,

we applied these forces as the external force vector to the drill pipe behavior estimation program applying ANCF (which will be discussed after this section) and calculated the underwater behavior of the rotating drill pipe model due to the Magnus effect, accordingly.

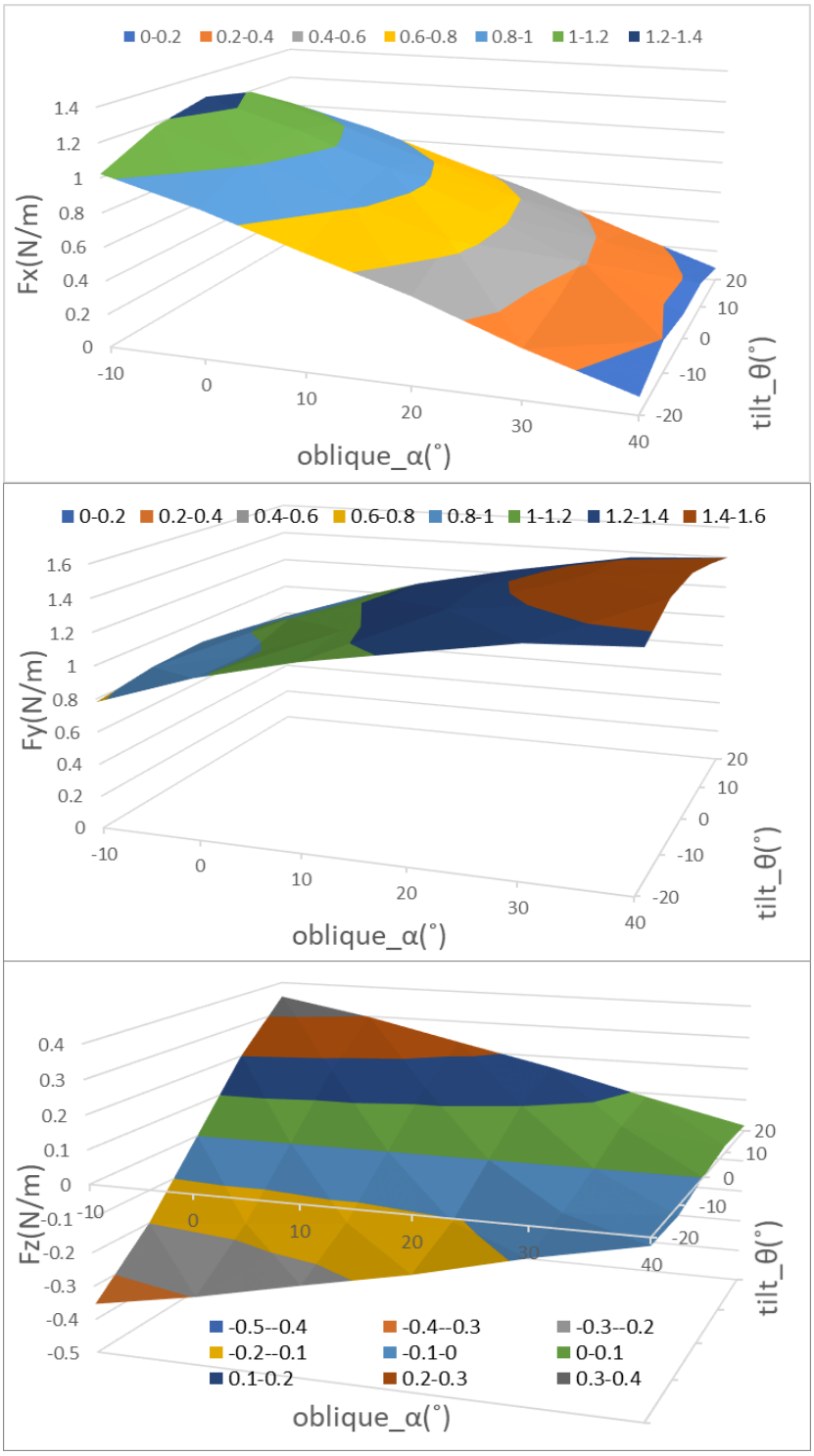

Fig. 4.6 Hydrodynamic force distribution (U=0.3m/s, 200rpm with clockwise rotation)

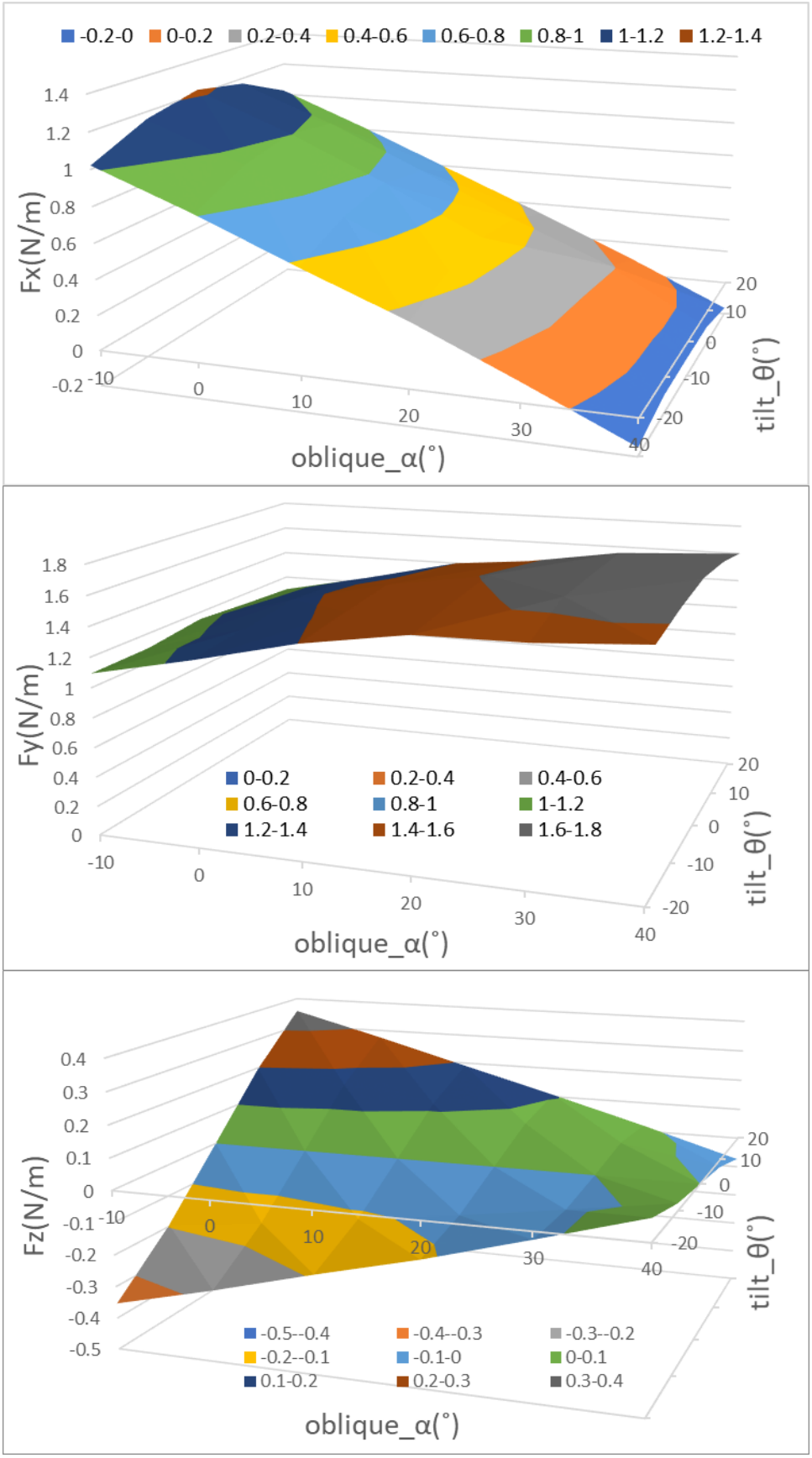

Fig. 4.7 Hydrodynamic force distribution (U=0.3m/s, 250rpm with clockwise rotation)

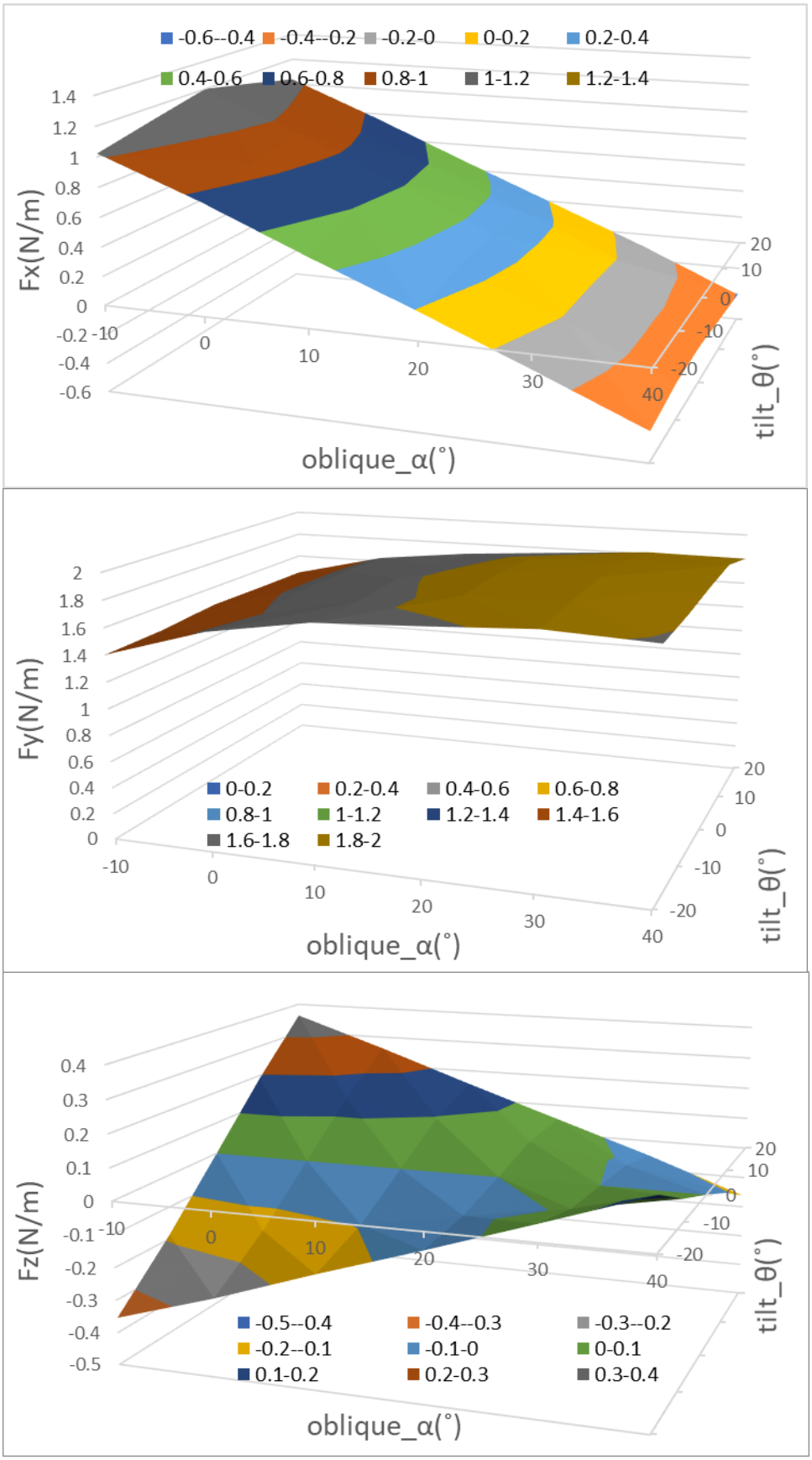

Fig. 4.8 Hydrodynamic force distribution (U=0.3m/s, 300rpm with clockwise rotation)

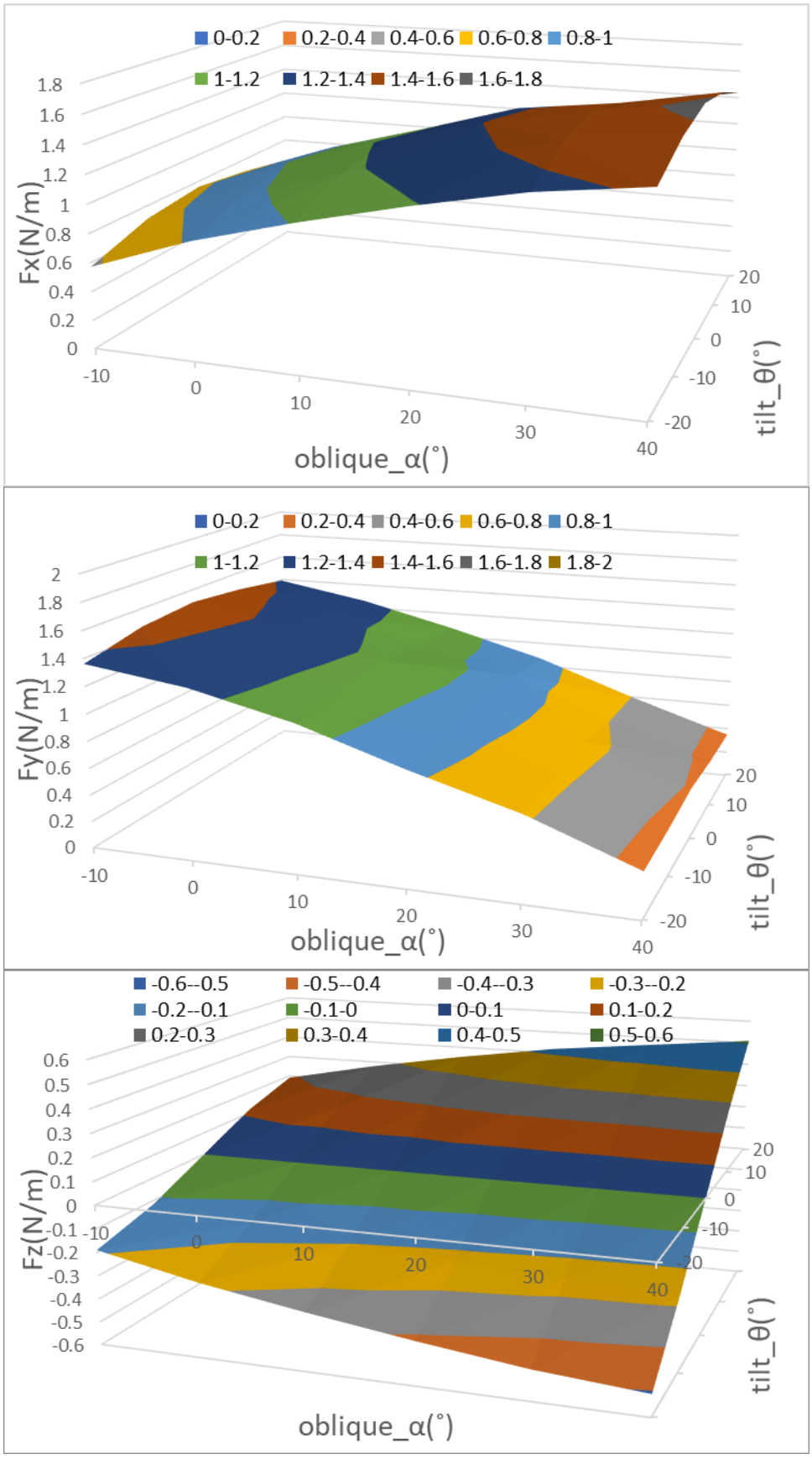

Fig. 4.9 Hydrodynamic force distribution (U=0.3m/s, 250rpm with counterclockwise rotation)

Chapter 5

Underwater Behavior of the Rotating Drill Pipe Model in Uniform Flow

5.1 Computational Setup and Boundary Conditions for Drill Pipe Model

To study the underwater behavior of the rotating drill pipe model due to the Magnus effect, we applied the three-dimensional hydrodynamic forces calculated from ANSYS Fluent as the external force vectors to the rotating drill pipe model implemented in ANCF. Unlike the previous study (Suzuki et al., 2022), we consider the drill pipe model length, (l_p)for 3.155 m in this case and the compensation for an extra 1m length, (l'), buried in the ground was not added in this calculation. Therefore, we set the ground reaction force as 0% as a preliminary condition and will use it as a variable for further calculations as shown in (Table 5.1) and the length of the pipe in the air, (l_a) was set up at 0.26 m and the other portion was set for 2.89 m in water until it reached the bottom of the guide pipe. The calculation condition of the rotating drill pipe model is shown in (Table 5.1).

Table 5.1 The calculation conditions for the ANCF simulation

Main particulars	SI unit
Total pipe length (l_p)	3.155 (m)
Length in the air (l_a)	0.26 (m)
Length in the ground (l')	0 (m)
Inflow velocity, U	0.3 (m/s)
Number of Revolution, ω	26.46 (rad/s) 250 RPM
Rotation Ratio ($r\omega/U$)	0.84
Ground reaction force NR [%], WOB	Variable

Since the bottom position of the drill pipe model has been fixed in the x, and y directions, the position only in the z-direction of the pipe has changed according to the pipe bending deformation profile. In addition, a corresponding ground reaction force is given to the last

node of the drill pipe to represent the ground state of the bottom of the sea. The boundary conditions for ANCF computation are stated in (Fig 5.1). Then, the displacement values of the pipe were calculated by applying these boundary conditions to the FORTRAN In-house Code developed for estimating the dynamic behaviors of the rotating drill pipe model.

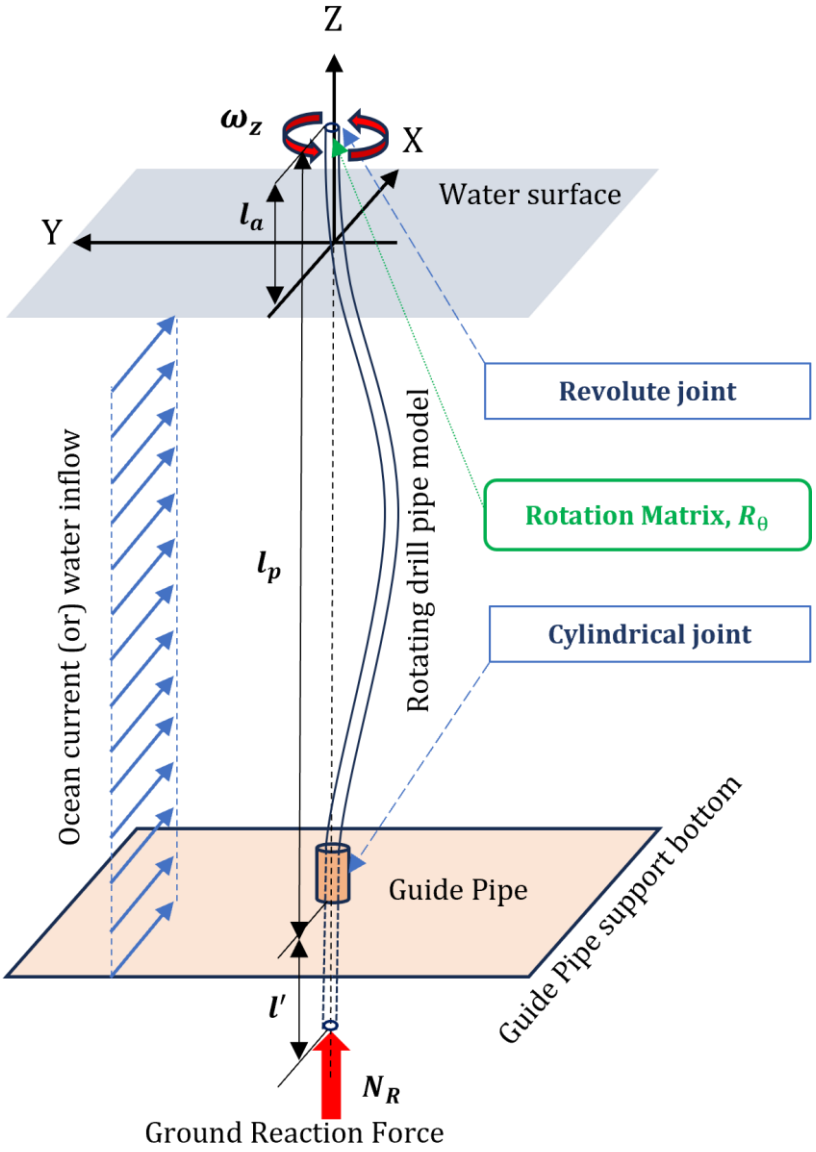

Fig. 5.1 Boundary conditions for the ANCF computation of the pipe model

In consideration of the boundary condition of the rotating drill pipe model, the upper end of the drill pipe model and the rotating device can be connected via a revolute joint which constrains all displacement in the *x*, *y*, and *z* directions and a rotation matrix, R_θ was

implied at the top node of the pipe. The lower connection of the drill pipe model and guide pipe was connected via a cylindrical joint, which restrains in *x, y* directions and, but allows rotation in the *z*-direction so that the actual drilling state can be expressed at the lower end.

In addition, a corresponding ground reaction force is given to the last node of the drill pipe to represent the ground state of the bottom of the sea. The boundary conditions for ANCF computation are stated in (Fig 5.1) and the characteristics of the rotating model drill pipe are described in (Table 5.1). Then, the displacement values of the pipe were calculated by applying these boundary conditions to the FORTRAN In-house Code developed for estimating the dynamic behaviors of the rotating drill pipe model.

A rotation matrix, $\boldsymbol{R}_\theta = (\boldsymbol{a}_1 \ \boldsymbol{a}_2 \ \boldsymbol{a}_3)$ was implied at the top node of the pipe to the *x*, *y*, and *z* directions can be expressed as in (Eq. 5.1) and (Eq. 5.2).

$$\boldsymbol{R_\theta} = \boldsymbol{J_0^{-1}} \begin{pmatrix} 1 & 0 & 0 \\ 0 & \cos\theta & \sin\theta \\ 0 & -\sin\theta & \cos\theta \end{pmatrix}, \ \boldsymbol{J_0} = (r_{,x_0} \quad r_{,y_0} \quad r_{,z_0}) \tag{5.1}$$

$$\boldsymbol{r}_{,x} - \boldsymbol{a}_1 = 0, \boldsymbol{r}_{,y} - \boldsymbol{a}_2 = 0, \boldsymbol{r}_{,z} - \boldsymbol{a}_3 = 0 \tag{5.2}$$

In consideration of the boundary condition of the rotating drill pipe model, the upper end of the drill pipe model and the rotating device can be connected via a revolute joint which constrains all displacement in the *x, y,* and *z* directions as described in (Eq. 5.3).

$$\boldsymbol{r}_1(t) - \boldsymbol{r}_1(t_0) = 0, \ \boldsymbol{r}_2(t) - \boldsymbol{r}_2(t_0) = 0, \boldsymbol{r}_3(t) - \boldsymbol{r}_3(t_0) = 0 \tag{5.3}$$

The lower connection of the drill pipe model and guide pipe was connected via a cylindrical joint, which restrains in *x*, *y* directions and, but allows to rotate in the *z*-direction as in (Eq. 5.4) so that the actual drilling state can be expressed at the lower end.

$$\boldsymbol{r}_1(t) - \boldsymbol{r}_1(t_0) = 0, \ \boldsymbol{r}_2(t) - \boldsymbol{r}_2(t_0) = 0, \boldsymbol{r}_{,x} - \boldsymbol{a}_1 = 0 \tag{5.4}$$

Here, t_0 and t are represented for the initial reference position and deformed state of the drill pipe model, respectively. Since the bottom position of the drill pipe model has been fixed in the *x, and y* directions, the position only in the *z*-direction of the pipe has changed according to the pipe bending deformation profile.

5.2 Underwater Behavior of the Rotating Drill Pipe Model Considering the Hydrodynamic Performance in the Uniform Flow

Based on the above computational setup (Fig. 5.1) and calculation conditions in (Table 5.1), we have carried out the ANCF simulation for the rotating drill pipe model stimulating in the uniform flow. In comparison with the experimental results, the calculated *y*-displacement (related to lifting force) is smaller than the experimentally measured value, while the *x*-displacement (related to the drag force component) is estimated to be similar. Nevertheless, the point where the largest deformation formed in the same position as the measured values in both x and y directions.

As shown in (Fig. 5.2), the calculated result for *y*-displacement was comparatively small to measured values and it is possible to reconsider the amount of hydrodynamics force exerted on the drill pipe model in the y direction and the further considerations for fluid force in the *y*-direction were discussed and mentioned below. Since the *y*-direction deformation is an important consideration for the configuration of the Magnus effect in this study, we need to implement the *x* and *y* displacements properly in the numerical simulation model. Before applying the hydrodynamic force considerations, we considered applying the ground reaction force as the weight on bit (WOB) exerted on the last node of the drill pipe model, and the calculation results are shown in (Fig 5.3).

According to (Fig. 5.3), the displacement in the *x*-direction was more deformed than the previous one shown in (Fig. 5.2) based on the applied *NR%*, meanwhile, in the *y*-direction, the deformation profile hasn't shown the proper shape although the ground reaction force applied on this calculation model. Here, it was found that the *x*-displacement in this calculation model can perform well with or without applying the ground reaction force. However, the deformation in the *y*-direction shows a different configuration compared to the experimental values in both cases. Therefore we decided to implement the evaluation of the hydrodynamic performance of the present model by taking into account the different hydrodynamic forces in the y-direction and the underwater dynamic behavior of the rotating drill pipe model in uniform flow incorporating the Magnus effect will be analyzed and discussed in details with 5 simulation case studies by multiplying with 25% increment of the current hydrodynamic force model as $1Fy$, $1.25Fy$, $1.5Fy$, $1.75Fy$ and finally $2Fy$ for the rotating drill pipe model.

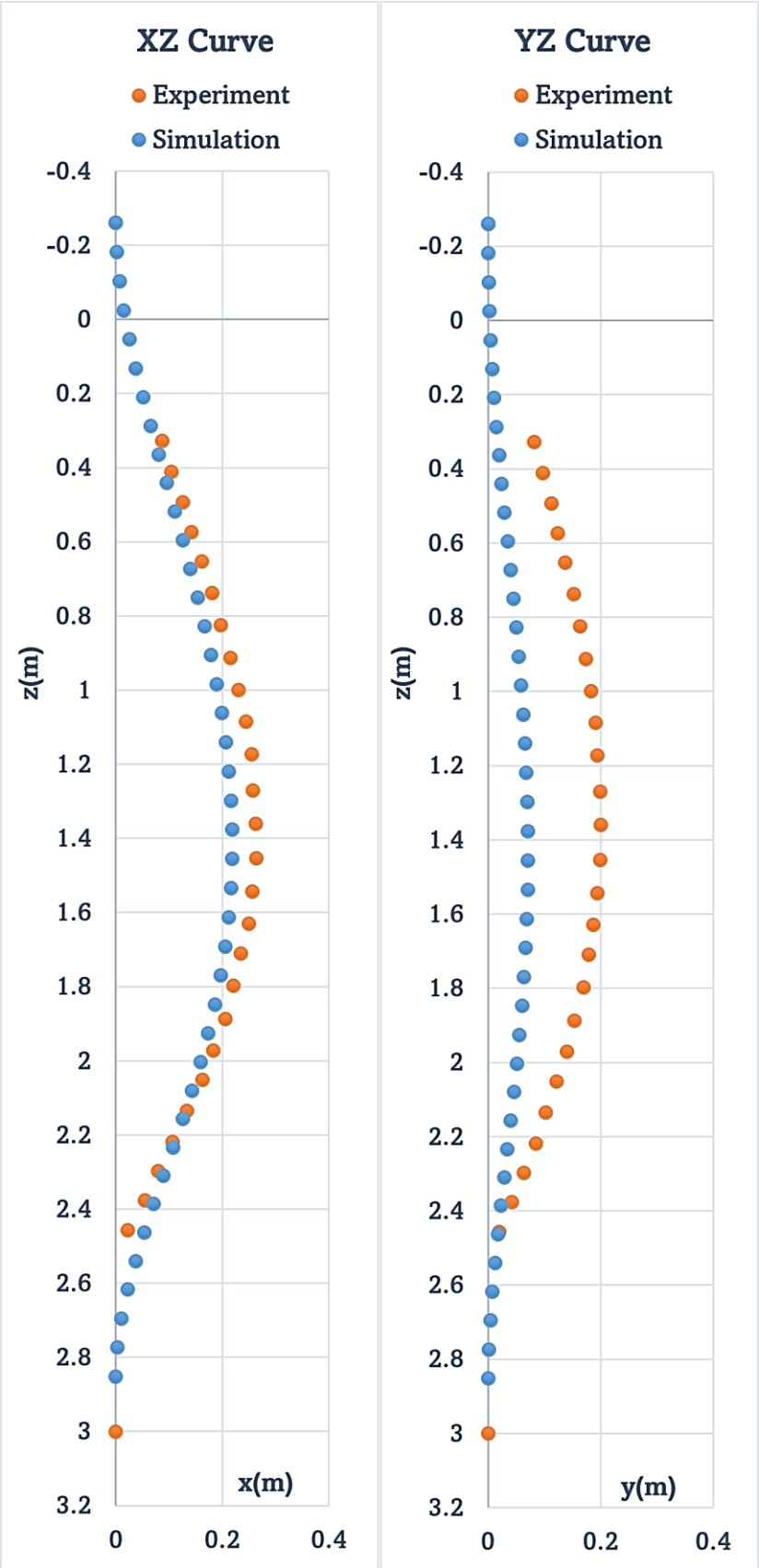

Fig. 5.2 Computational result for the rotating drill pipe model in uniform flow

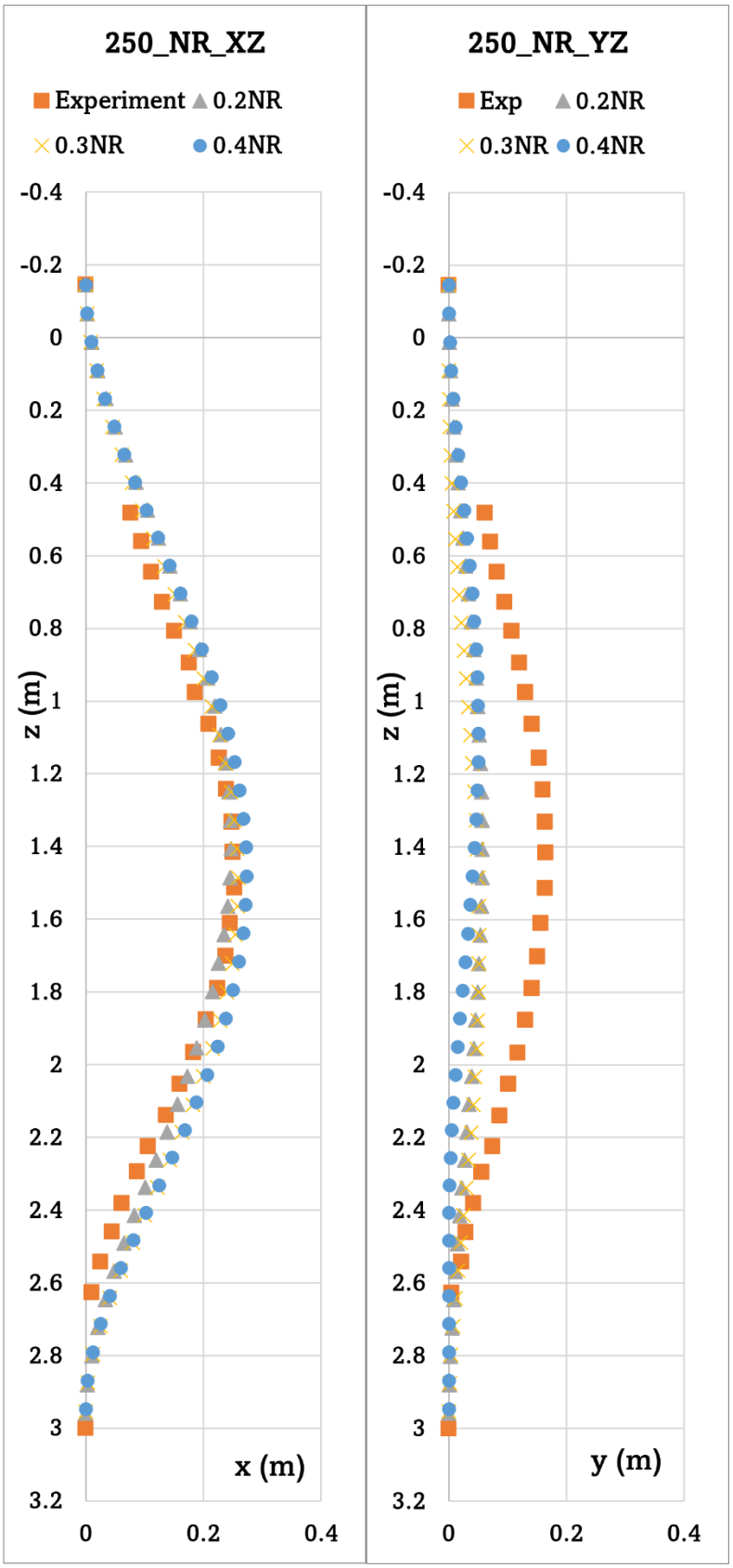

Fig. 5.3 Computational result for the rotating drill pipe model considering the *NR%*

5.2.1 Study Case 1 (Original Fluid Force)

Based on the above computational setup and calculation conditions in (Table 5.1), we have carried out the ANCF simulation for the rotating drill pipe model stimulating in the uniform flow. In comparison with the experimental results, the calculated *y*-displacement (related to lifting force) is smaller than the experimentally measured value, while the *x*-displacement (related to the drag force component) is estimated to be similar. Nevertheless, the point where the largest deformation formed in the same position as the measured values in both *x* and *y* directions.

As shown in (Fig. 5.4), the calculated result for *y*-displacement was comparatively small to measured values and it is possible to reconsider the amount of hydrodynamics force exerted on the drill pipe model in the *y* direction and the further considerations for fluid force in the *y* direction were discussed and mentioned below.

5.2.2 Study Case 2 (1.25 *Fy*)

In the case of 1.25 times increase in fluid force in the *y* direction, both *x* and *y* displacement values increase for the drill pipe model as in (Fig. 5.5). It can be found that the *x*-displacement shows better-estimated values compared to measured values. While in *y*-displacement, it will still need to get some further approximation for fluid force values, although it shows better results than the previous *y*-displacement values shown in (Fig. 5.4).

The maximum displacement value for *x*-displacement shows similar results with measured values. Meanwhile, in the case of displacement in the y direction, although the deformed shape shows a similar shape with measurement values, the magnitude needs to increase to get a better approximation of the behavior of the rotating drill pipe model.

5.2.3 Study Case 3 (1.5 *Fy*)

When the fluid force in the *y* direction increased to 1.5 times its original value, the x-displacement was agreed with the measured values. The *y*-displacement tends to be closer than the previous cases and the magnitude of *y*-displacement here has significantly increased compared to Case 1 as shown in (Fig. 5.6), which used the original fluid force values resulting from CFD calculation and Case 2, 1.25 times increase in *Fy*.

Although the magnitude of the fluid force in the *y* direction has increased, the *x*-displacement has still shown the proper deformed shape compared to measured values and *y*-displacement has gradually increased related to the values of the fluid force. Meanwhile, the maximum displacement values for both *x* and *y* show the same position as the experimental results.

5.2.4 Study Case 4 (1.75 *Fy*)

In this case, the fluid force in the *y* component has raised to 1.75 times larger than the force in Case 1. Here, the displacement in x was a little bit smaller than the measured one, but the *y*-displacement tends to have congruence with the measured values, and the position that the maximum displacement occurred for both *x* and *y* directions has become the same point as seen in (Fig. 5.7).

To compare the previous cases, the displacement in the *x* and *y* directions shows the optimum position in the other cases. Not only the magnitude but also the deformed shape of the calculated condition coincides with the experimentally measured values in this case. Moreover, it can be found that the maximum displacement value was shown near the center point of the rotating drill pipe model, where the Magnus force will be the greatest along the length of the pipe.

5.2.5 Study Case 5 (2.0 *Fy*)

To study the underwater behavior of the rotating drill pipe model for the fluid force values in the y component, the fluid force values in Case 5 were enlarged double compared to Case 1. In this simulation, the x-deformation shows some differences both in the upper and lower parts of the drill pipe model as in (Fig. 5.8). In contrast, *y*-displacement for the pipe has still coincided with the experimental results.

Despite the computational results in Case 5 showing the acceptable deformed shape in the *x* and *y* direction, it cannot be denied that the computational results for Case 4 (1.75*Fy*) have better approximation results in both displacement values. Moreover, the difference between the computational and measured value is shown in the *x*-displacement while the *y*-displacement in Case 3, as in (Fig. 5.6).

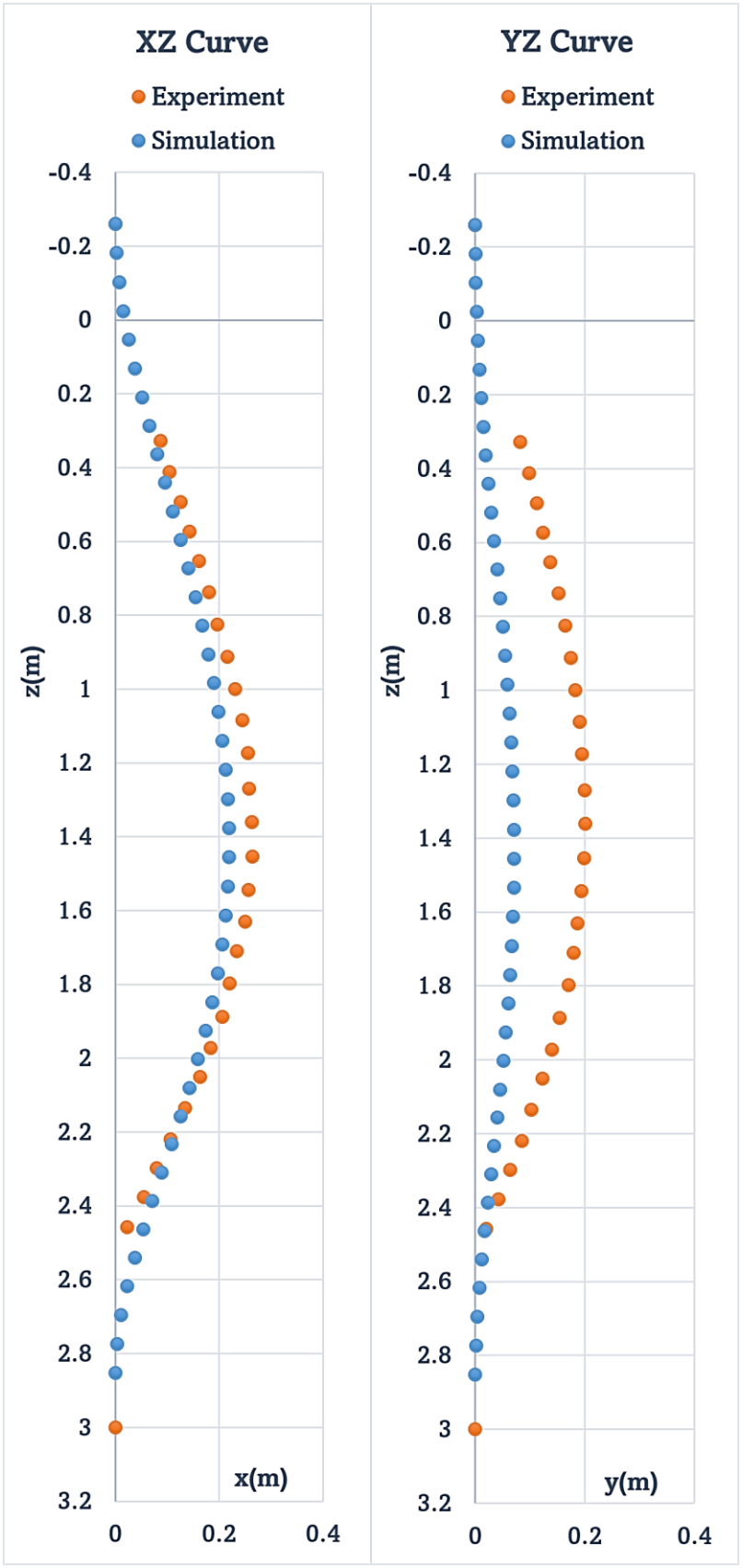

Fig. 5.4 Computational result for rotating drill pipe model considering 1.0*Fy*

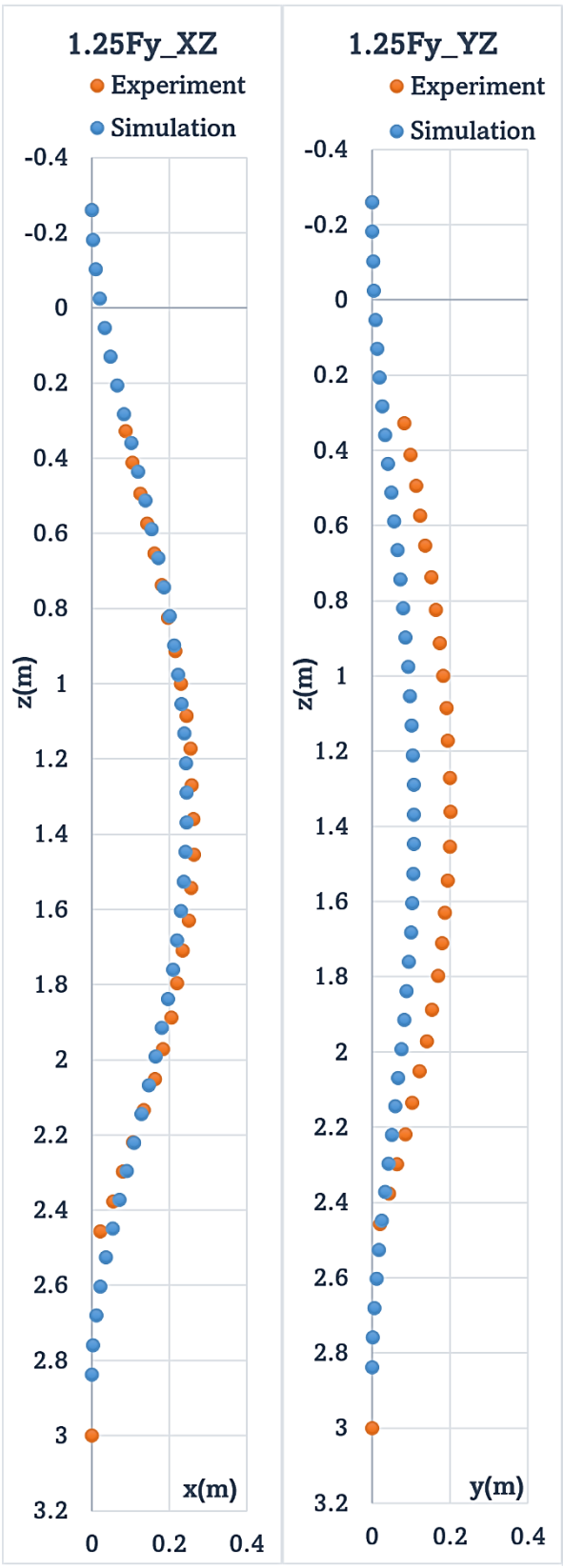

Fig. 5.5 Computational result for rotating drill pipe model considering 1.25*Fy*

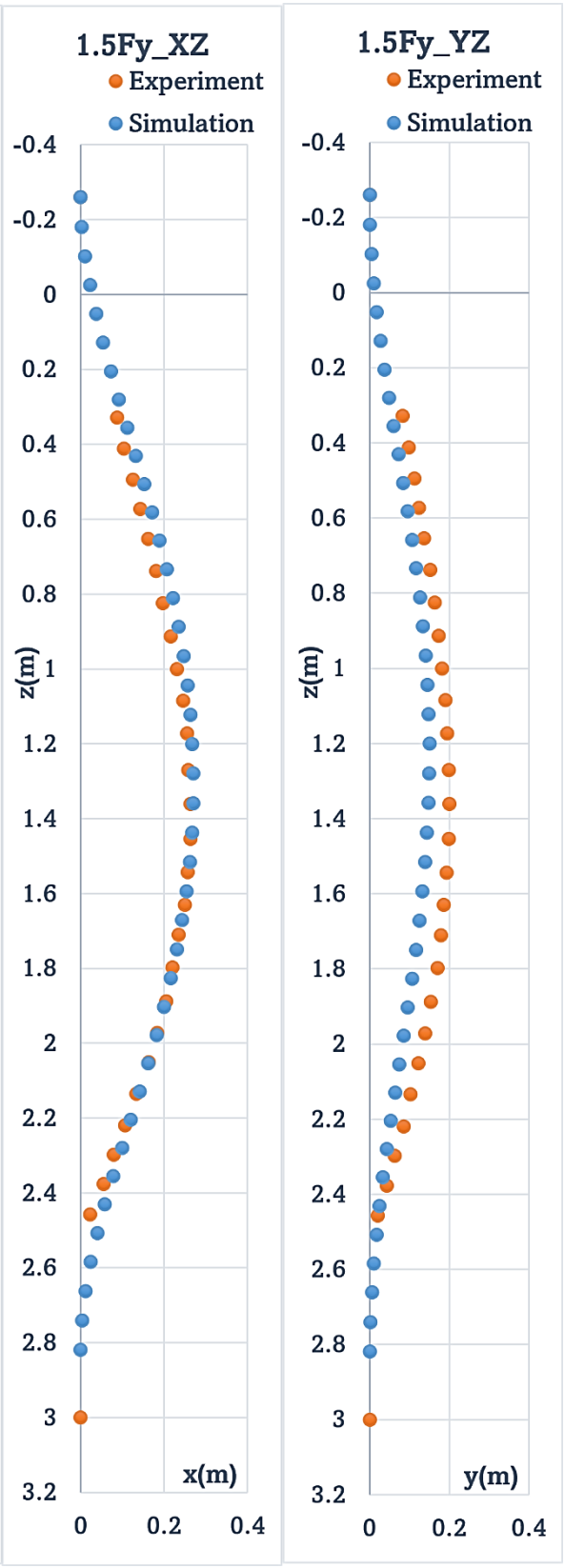

Fig. 5.6 Computational result for rotating drill pipe model considering 1.5*Fy*

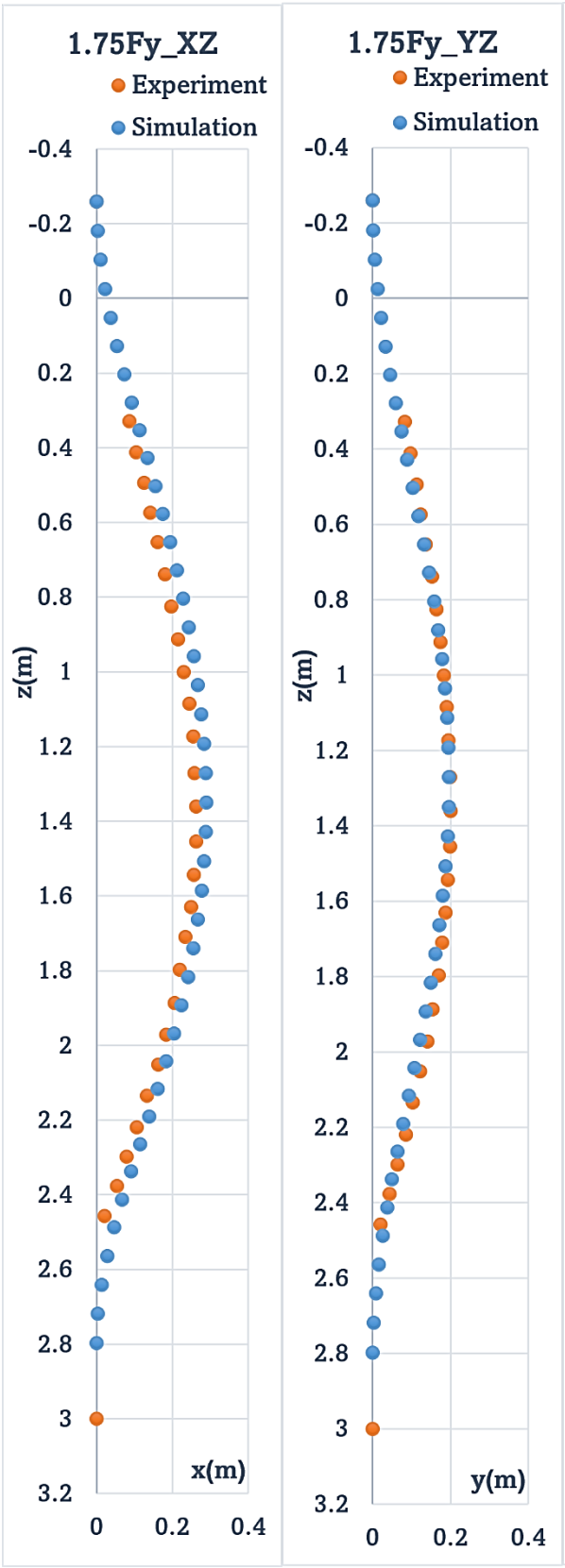

Fig. 5.7 Computational result for rotating drill pipe model considering 1.75*Fy*

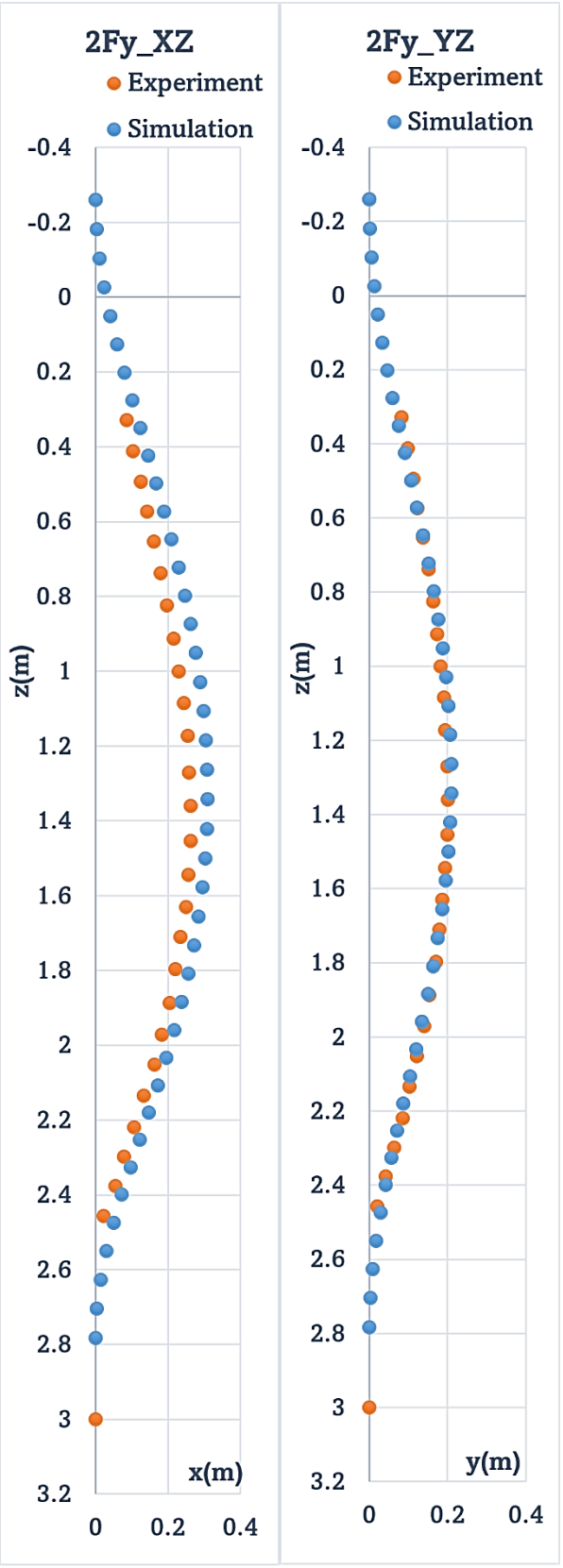

Fig. 5.8 Computational result for rotating drill pipe model considering 2.0*Fy*

5.2.6 Hydrodynamic performance on the Different Rotational Velocities by applying the $1.75Fy$

From the above study cases, the optimum deformation profiles in the x and y directions were found when the hydrodynamic force in the y-direction was increased by 1.75 times than the original one. Based on these facts, the computations for the different rotational velocities of the rotating drill pipe model were implemented and compared to the drill pipe model experimental results which were carried out in the Osaka University towing tank previously. The computational conditions for this calculation are described in Table 5.2.

Table 5.2 Computational conditions for the different rotational velocities with $1.75Fy$

Main particulars	SI unit
Length (l_p)	3.155 (m)
Length in air (l_a)	0.145 (m)
Length in the ground (l')	0 (m)
Pushing distance, dp	0.115(m)
Inflow velocity, U	0.3 (m/s)
Number of Revolution, ω	200,250,300 RPM
Rotation Ratio ($r\omega/U$)	0.84
Ground reaction force NR [%], WOB	0%

The computational results for different rotational velocities of 200,250 and 300rpm with $1.75Fy$ were mentioned in Fig. 5.9, 5.10, and 5.11 accordingly. In these cases, the displacements in the x-direction show similar profiles and are slightly larger than the experimental condition in 200 and 250 rpm calculations, but in the 300 cases, the x displacement is relatively similar to the experimental values. On the other hand, the displacement profiles in the y-direction coincide with the experimental values in all cases of 200,250 and 300 rpm respectively. Therefore, it was proven that the consideration of hydrodynamic performance on the behaviors of the rotating drill pipe model was congruent when the hydrodynamic force in the y-direction was increased by 1.75 times than the original one for every rotational speed of the pipe model.

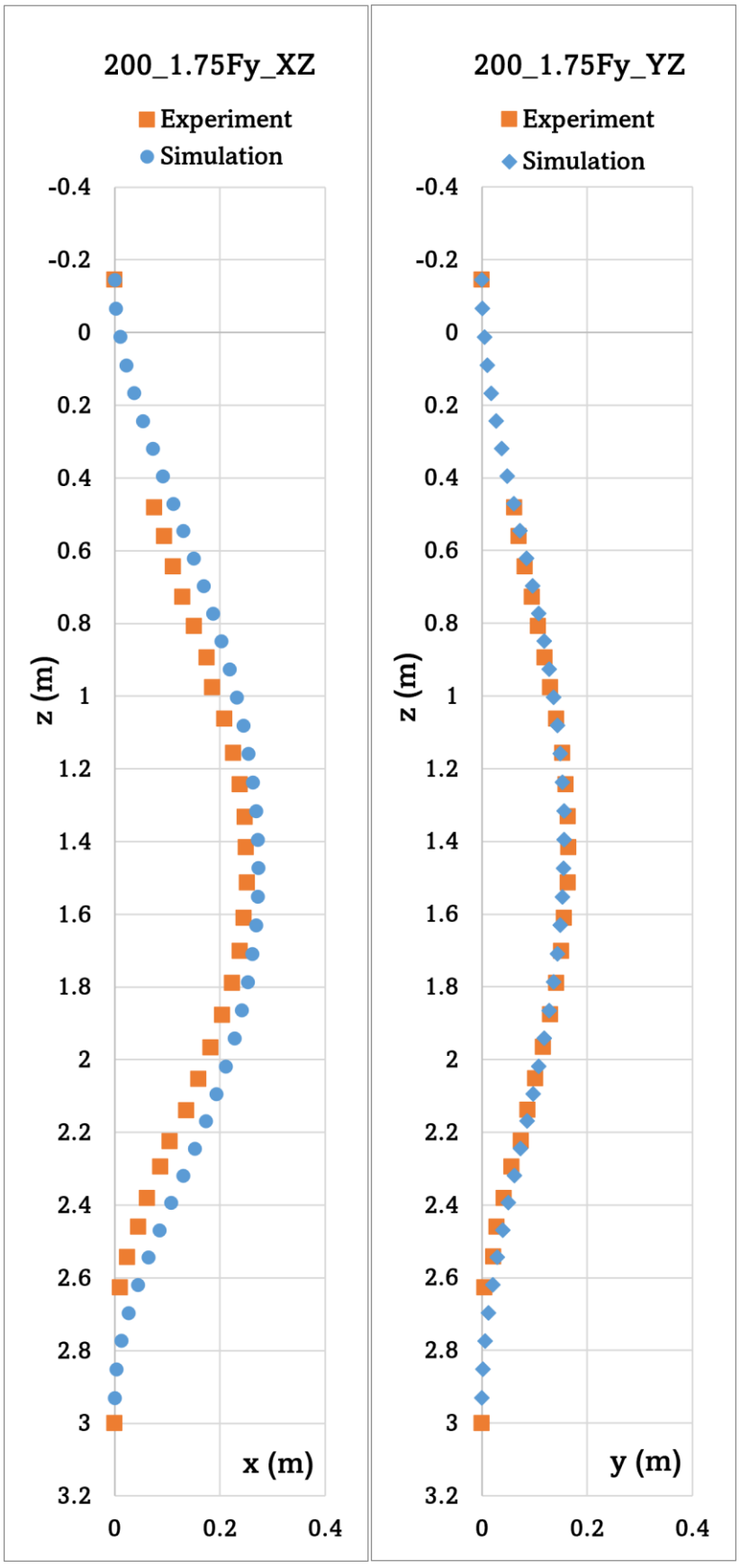

Fig. 5.9 Computational results for rotating drill pipe model (200RPM,1.75*Fy*)

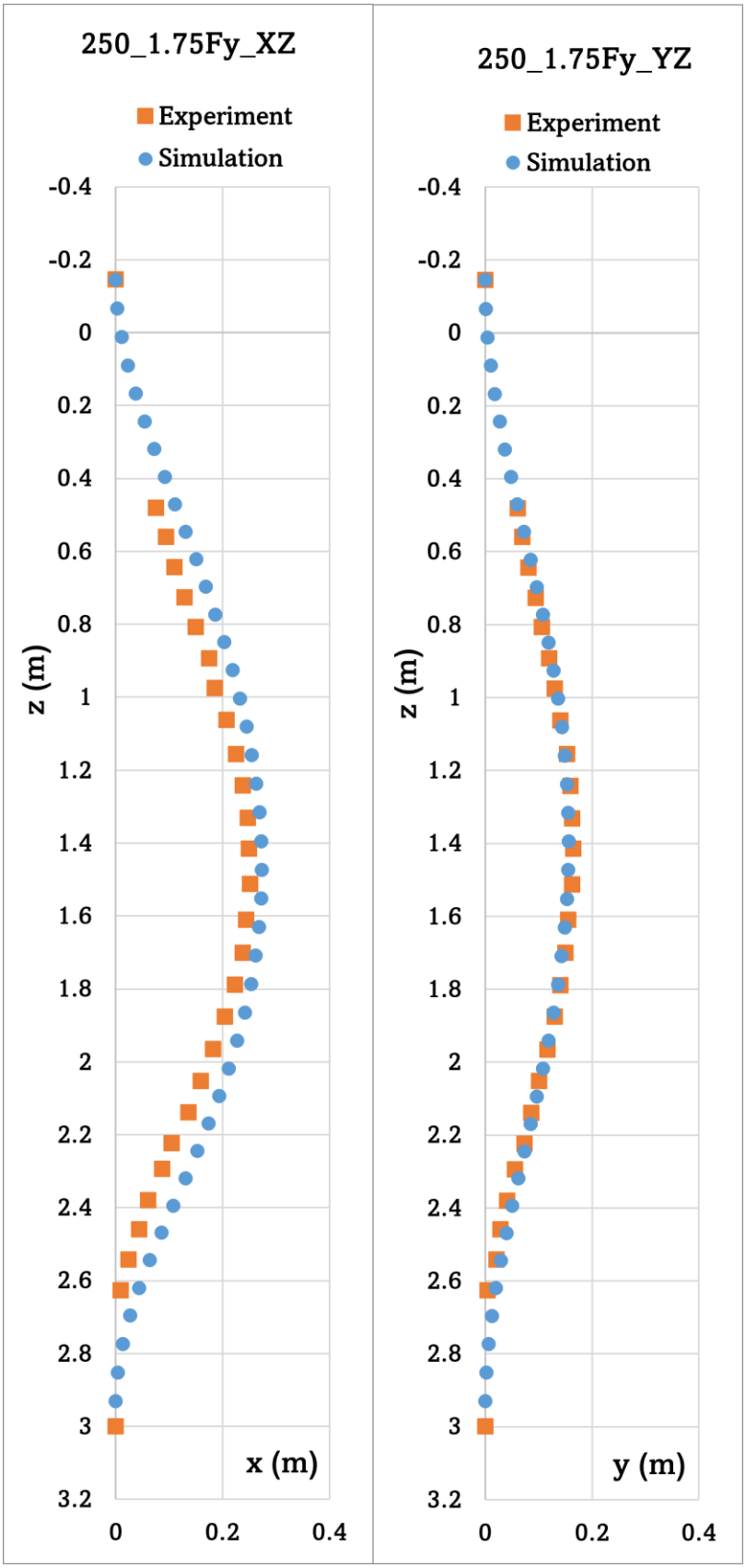

Fig. 5.10 Computational results for rotating drill pipe model (250RPM,1.75*Fy*)

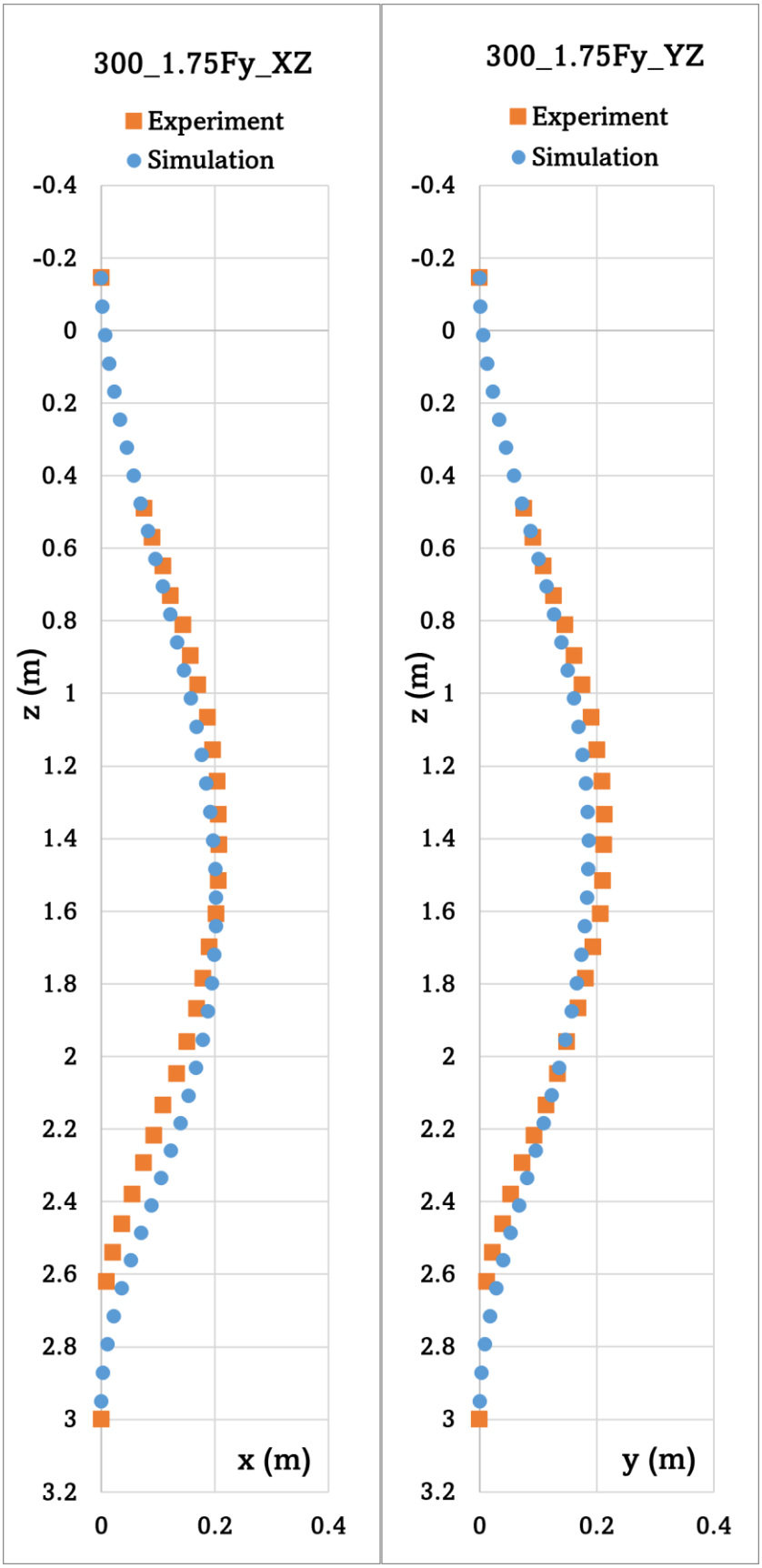

Fig. 5.11 Computational results for rotating drill pipe model (300RPM,1.75*Fy*)

5.3 Underwater Behavior of the Rotating Drill Pipe Model Considering the Effect of Internal Viscous Damping Model

In the previous section, it was discussed about the hydrodynamic performance on the dynamic behavior of the drill pipe model, and it was proposed that the optimum results on the behavior of the drill pipe model were obtained by increasing the 1.75times of hydrodynamic force in the *y*-direction. On the other hand, another consideration of the rotating drill pipe model was analyzed and discussed based on the material properties of the drill pipe model called, internal viscous damping as the continual study on the behavior of the drill pipe model.

Internal viscous damping is a phenomenon that can be encountered in systems where the energy is dissipated due to the internal friction between the components of the system as they move relative to each other. This damping mechanism is commonly observed in mechanical systems, such as oscillatory systems like springs and dashpots. When a system undergoes oscillatory motion, internal viscous damping converts some of the mechanical energy into heat, thereby reducing the amplitude of the oscillations over time. This damping effect is typically modeled by a damping coefficient, which quantifies the amount of damping present in the system.

In practical terms, internal viscous damping appeared as the resistance to motion within the system, resulting in a gradual decrease in the amplitude of oscillations or vibrations until the system reaches a steady state or comes to rest. It plays a crucial role in controlling vibrations and ensuring stability in various engineering applications, such as structural dynamics, vehicle suspension systems, and mechanical machinery.

In this section, the computation results of the underwater behavior of the drill pipe model considering the effect of different damping ratios were analyzed and discussed based on two elastic force models. Since we applied the Teflon material as the drill pipe model in this study and considered as a flexible structure because of its dimensional ratio and material properties, the application of hyper-elastic material models will be advantageous to capture the pipe deformation well and the applicability of these models to the study of underwater behavior of the drill pipe, which is made of steel, can also be observed as a future study.

5.3.1 Consideration of Damping Ratio (Internal Viscous Damping) on the Dynamic Behavior of the Rotating Drill Pipe Model

In a previous study, (Tun et al., 2023), the damping constant, ξ (also called damping ratio) was set at 0.05 (5%) and the study of drill pipe model behavior based on the consideration of hydrodynamic forces was carried out and it was congruent with the experimental result. Meanwhile, it was analyzed that the calculation accuracy should have been increased to capture the Magnus effect in y-displacement with better hydrodynamic force consideration. Therefore, consideration of the internal viscous damping model with the proper damping constant should also be applied to the drill pipe dynamic analysis in ANCF as an alternative study.

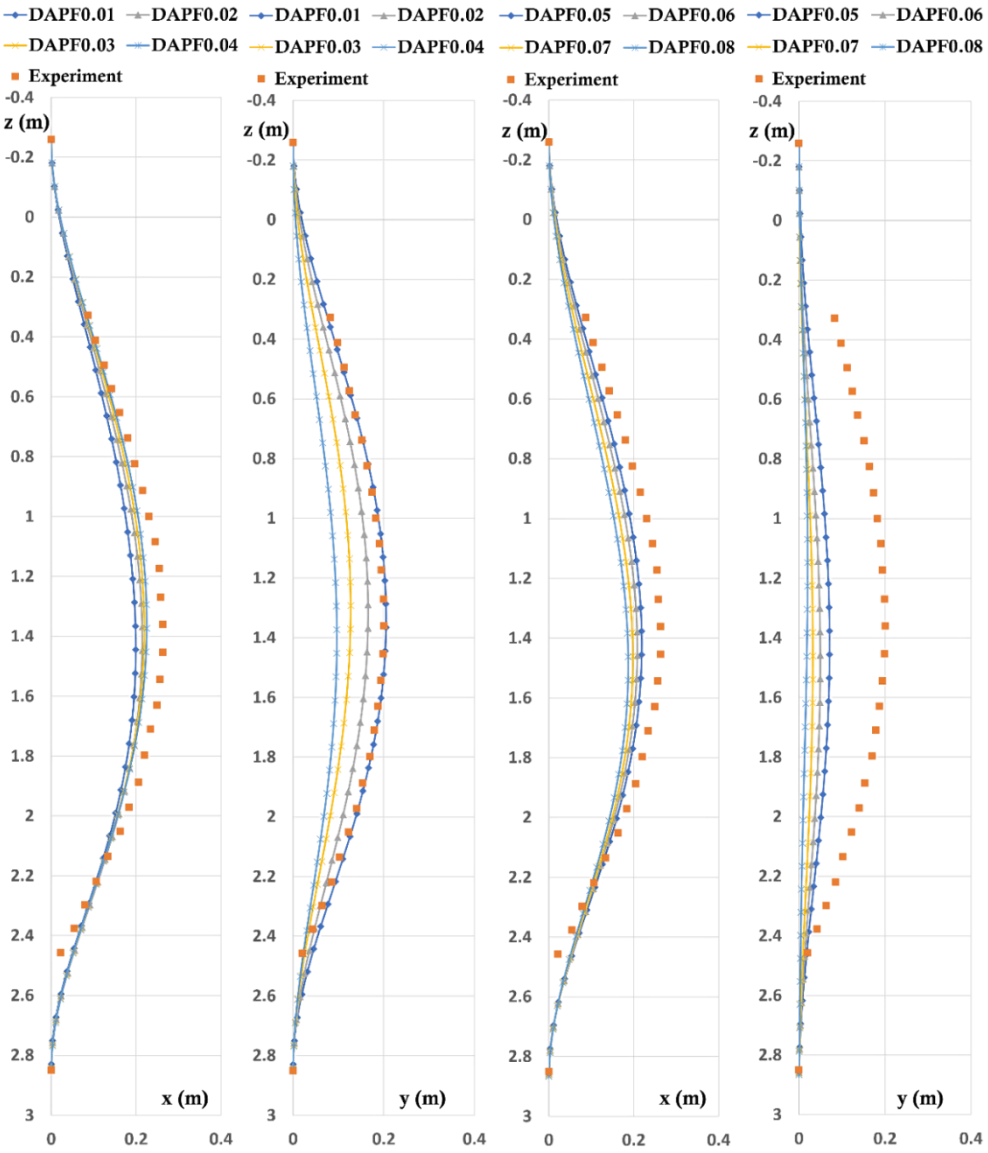

Fig. 5.12 Effect of damping ratios on the behavior of drill pipe model (ξ=0.01-0.08)

Therefore, the numerical study of the underwater behavior of the drill pipe model based on the consideration of the effect of internal viscous damping (in different damping ratios 0.01-0.08) without considering the WOB (*NR*= 0%) was carried out as shown in (Fig. 5.12) and (Fig. 5.13).

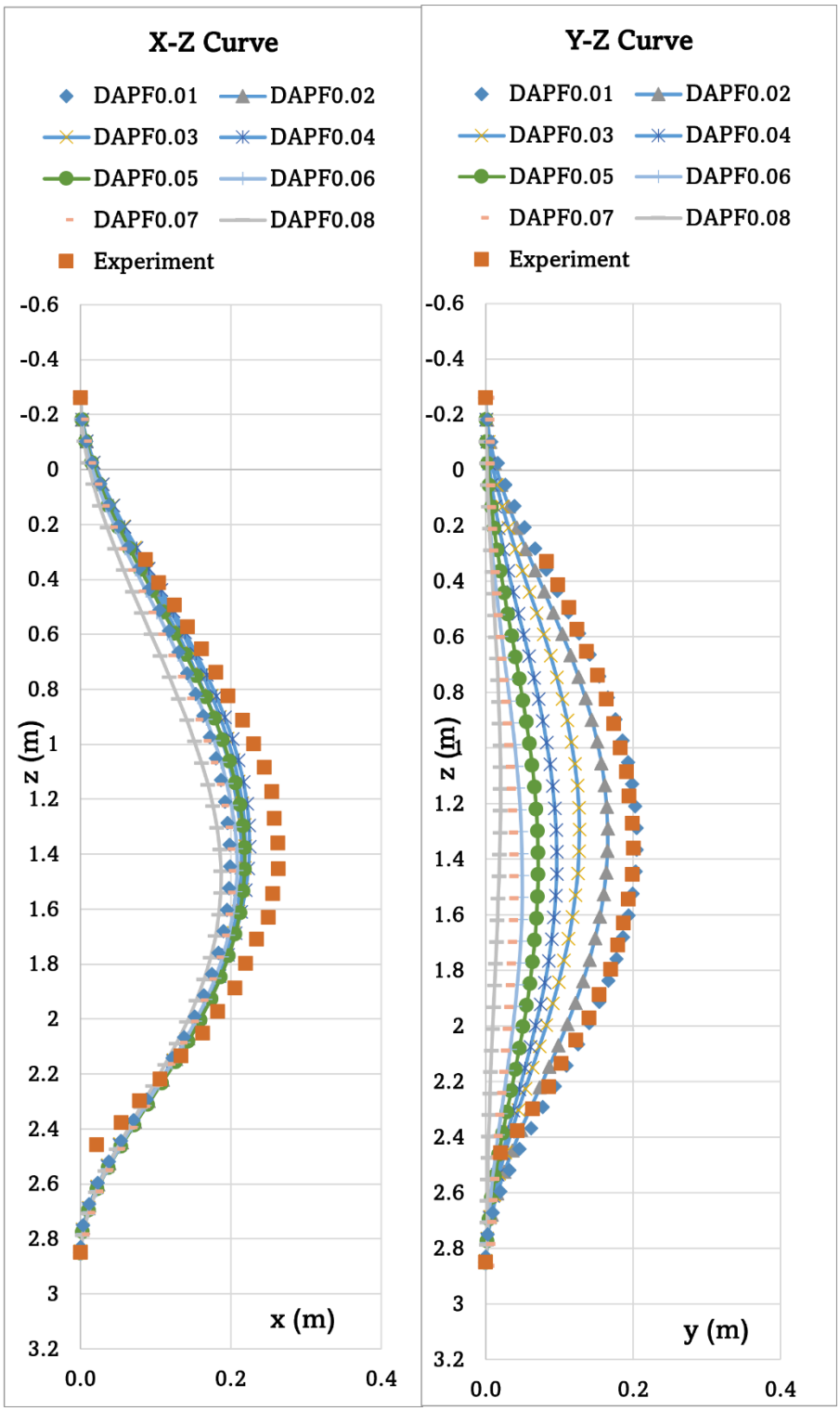

Fig. 5.13 Comparison of the effect of damping ratios on the behavior of drill pipe model (ξ=0.01-0.08)

Among these results, the x and y displacements showed better results in damping constant 0.01 to 0.04 and y displacements lacked congruence in the values of 0.05-0.08 although x displacements were similar to experiment results. Although the y-displacement shows the congruent results for $\xi = 0.01$, the x-displacement shows the difference compared to the experiment. Thus, the optimum results were obtained at damping ratio 0.02 in x and y displacements as shown in (Fig. 5.12).

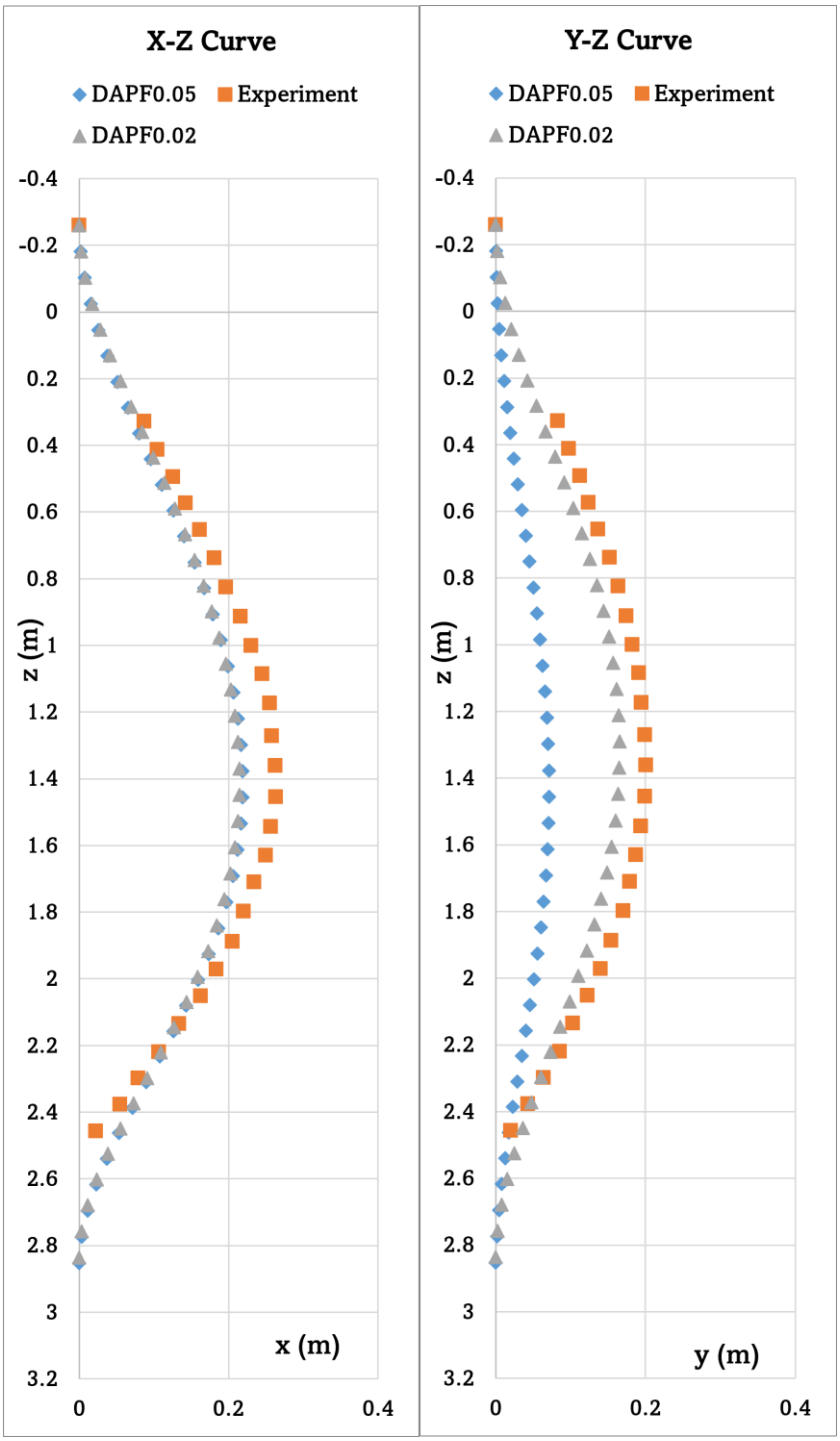

Fig. 5.14 Computational result comparison for (ξ=0.02 and ξ= 0.05) with the experimental results

According to Fig. 5.12 and 5.13, the effect of the damping ratio on the dynamic behavior of the rotating drill pipe model was observed as the x-displacement shows less dependency on the damping ratio values meanwhiles in y-displacement shows that the deformation profile is dependent dominantly on the damping ratio values. The deformation profiles of damping constant ξ=0.02 and 0.05 were mentioned in Fig. 5.14 and especially, the y displacements are described in better shape with the experimental results in ξ=0.02.

5.3.2 Comparative Studies of the Elastic Force Models

In this section, the dynamic behavior of the rotating drill pipe model was discussed by considering the different damping constants with the comparative studies of the appropriate material model for drill pipe. The range of damping constant from (ξ=0.01-0.05) for two different elastic force models of Mooney Rivlin and Neo-Hookean model was analyzed and described in Fig. 5.15 and Fig. 5.16. From this analysis, it was proven that the optimum damping constant for both x and y displacements would be (ξ=0.02).

Therefore, by using the optimum damping constant, (ξ=0.02), obtained from the previous calculations, we evaluated the dynamic analysis of the drill pipe model on two hyper-elastic models, Neo Hookean and Mooney Rivlin models, based on the viscoelastic force formulation and internal damping model in ANCF.

The deformations of the drill pipe model based on the comparative studies of the elastic force models without considering the WOB fluctuations (N_R=0%), were described in (Fig. 5.17). According to (Fig. 5.17), x and y displacements in the Mooney Rivlin model show better results than the displacements in the Neo Hookean model compared to the experiment data for the drill pipe model.

Since the drill pipe model's material, Teflon is easy to deform and has the properties of thermoplastic behaviors, setting up a proper damping ratio and modeling with the appropriate hyper-elastic material models could lead to the exact modeling of the pipe deformation profile. For both elastic force models, it was observed that the deformation profiles of the x and y displacements were similar to the experimental results before applying the WOB to the current models with a new damping constant of (ξ=0.02).

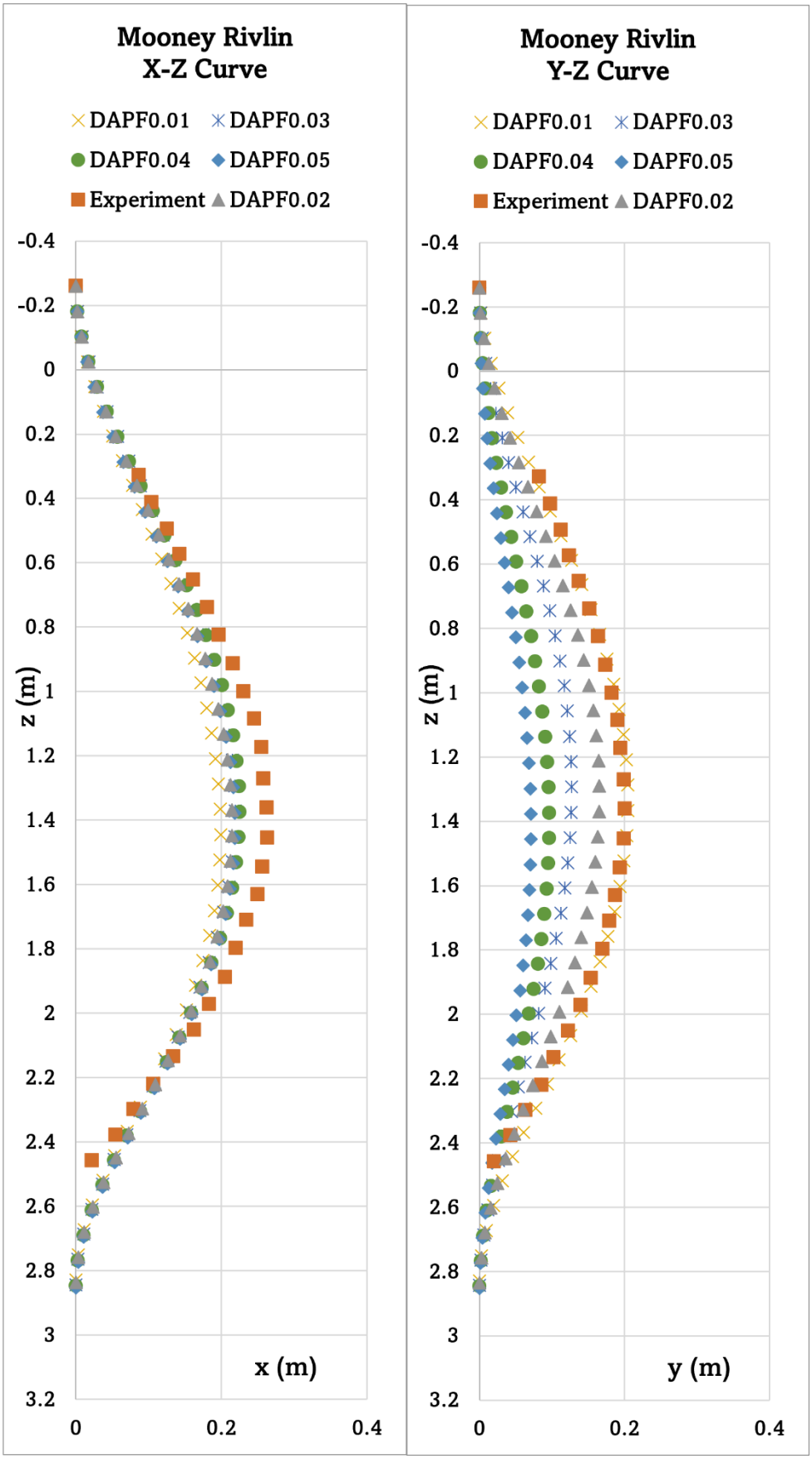

Fig. 5.15 Computational results for damping ratios (ξ=0.01-0.05), Mooney Rivlin Model

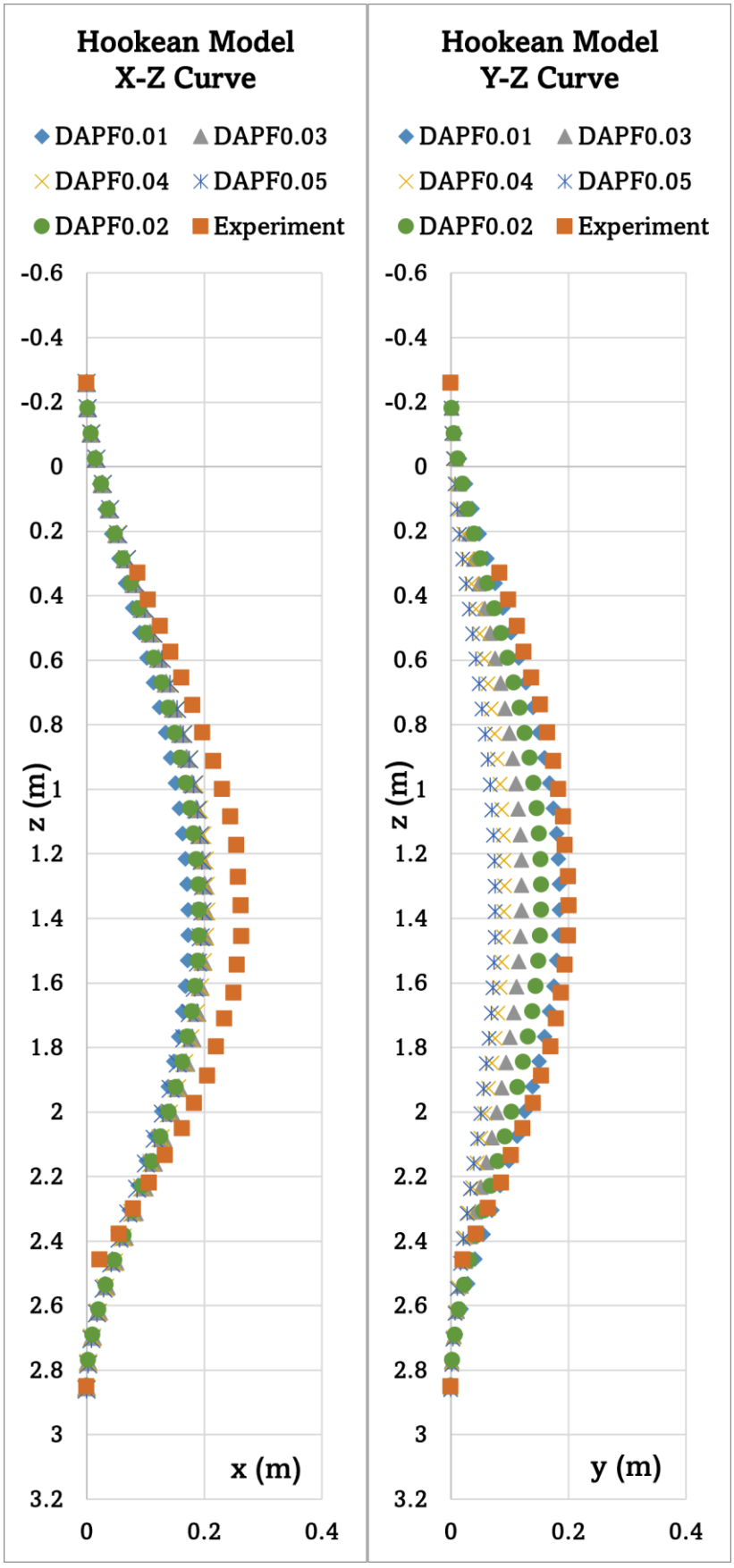

Fig. 5.16 Computational results for damping ratios (ξ=0.01-0.05), Neo Hookean Model

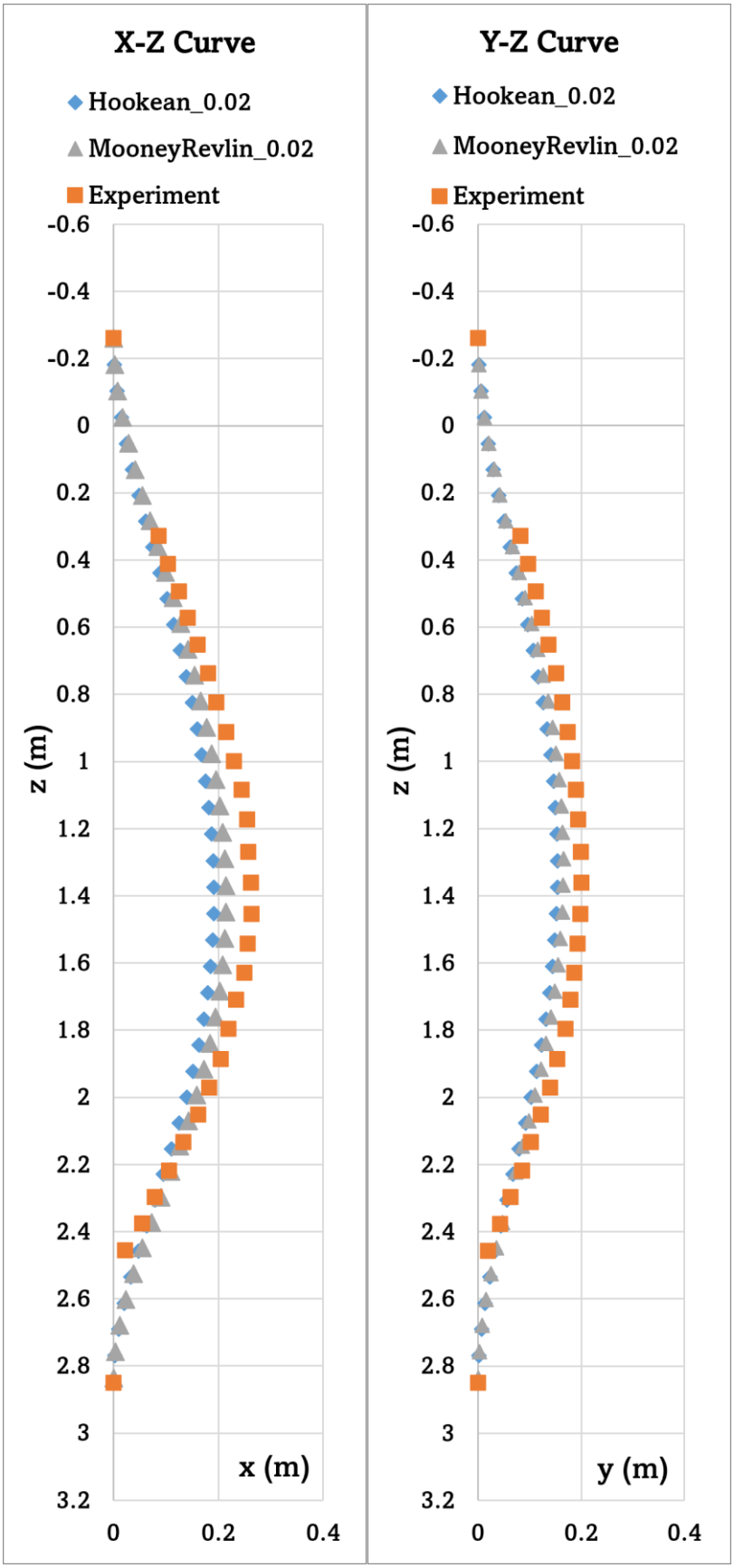

Fig. 5.17 Deformation of the pipe on elastic force models (Neo Hookean and Mooney Rivlin) with *NR*=0% and damping constant, ξ=0.02

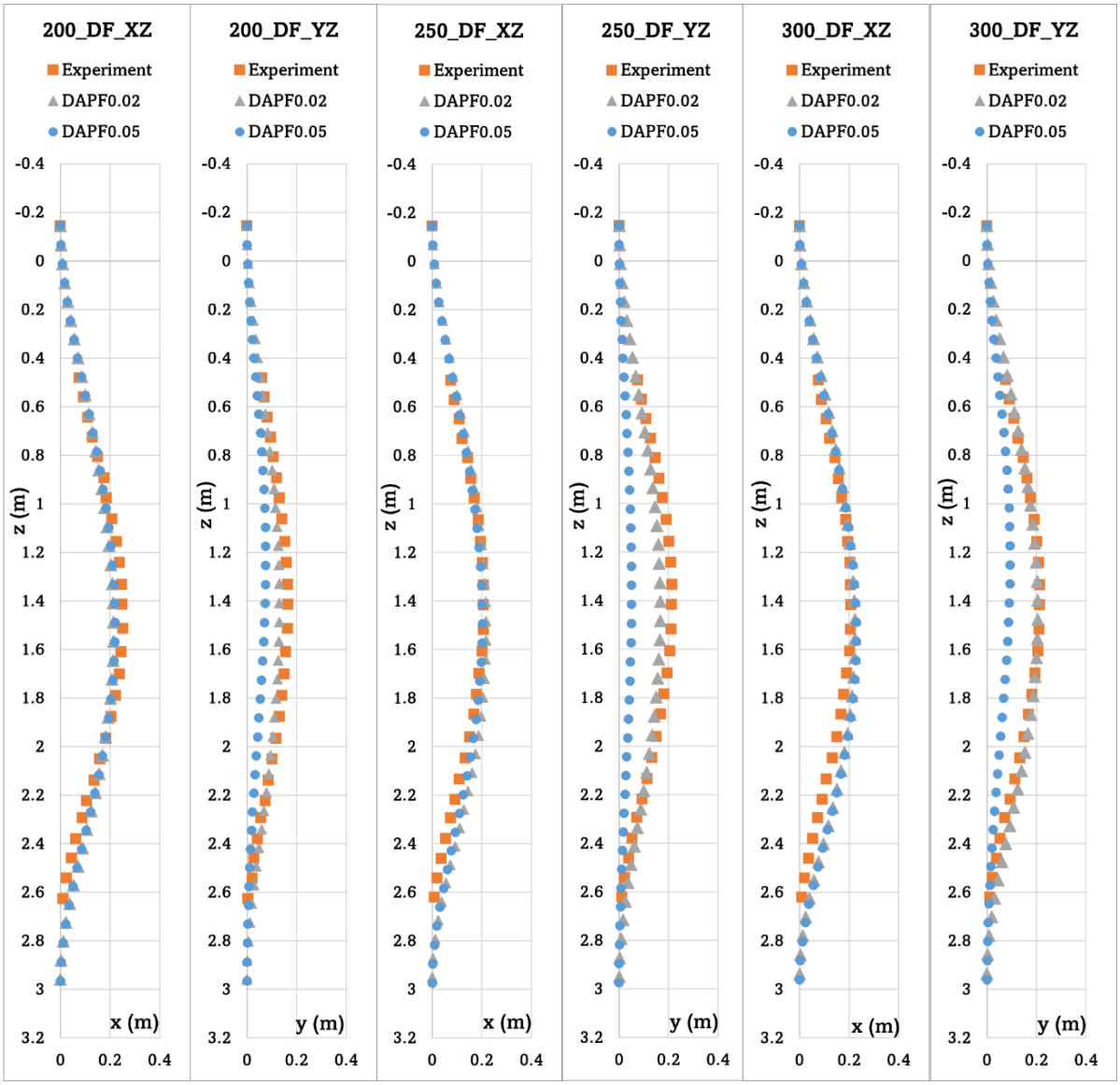

Fig. 5.18 Computational results comparison for the rotational velocities of 200,250, and 300 rpm with damping constant, ξ=0.02 and ξ=0.05 with the experimental values

Since the drill pipe model of 250 rpm shows better results than the previous studies, the dynamic behaviors of the rotating drill pipe model in other rotational velocities will be one of the study interests of this study. Therefore, the analysis of the rotating drill pipe model operating at 200,250, and 300 rpm with a pushing distance of 115 mm, (length in air = 0.145m) was carried out by using the damping constant of 0.02 and 0.05 as the comparison study as shown in Fig. 5.18. Based on these results, the deformation profiles in the y-direction for all of the rotational velocities improved with the new damping constant, as well as the *x*-deformation.

5.3.4 Fluctuation of WOB on the Pipe Deformation

In this study, we aimed to investigate the pipe's WOB fluctuation phenomenon, which is important to maintain the proper range for the drilling operation. If the pipe has very large WOB values, the pipe will lead the fatigue and failure and if less amount than the required one, it will not reach the optimum drilling operation stage. On the other hand, we couldn't capture it not only in the actual drilling operation but also in the experiment currently because of the lack of measurable methods for the pipe bottom position. Thus, the variable ground reaction force will be considered as a percentage of pipe weight and the status of WOB and the pipe bottom position in the z direction will be discussed in this study.

To study the dynamic behaviors of the drill pipe in drilling operations, it has been still challenging to maintain the proper WOB because of the many constraints in visibility and measuring methods that can measure the drill pipe dynamics behaviors in the ocean. In the previous study (Suzuki et al., 2022), the underwater behavior of the non-rotating drill pipe model which took into account the weight on bit fluctuation was described with the consideration of ground reaction force, $NR\%$ which exerted at the last node point of the pipe model as shown in (Fig. 5.1).

In addition, the dynamic analysis of the rotating drill pipe model without considering the effect of WOB was presented by (Tun et al., 2023). Thus, the study of the underwater behavior of the rotating drill pipe model considering the WOB fluctuation is necessary to implement as one of the research interests of this study.

As described in (Fig. 5.19, 5.20), the deformation in the x and y directions without WOB and under the proper WOB fluctuation were different for both material models of the rotating drill pipe model. Not only the x-displacement but also the y-displacement were congruent with the experiment result and the deformed shape was also almost the same in the drag profile (x-displacement) and lift profile (y-displacement) with the current hydrodynamic force model. The optimum WOB fluctuation which coincides with the experimental results was found at 22.5% for the Mooney Rivlin Model and 45% for the Neo Hookean Model with the comparison of with or without WOB reported in (Fig. 5.21 and 5.22).In addition, the deformation profiles with WOB fluctuation improved and coincided with the experimental results in both material models respectively.

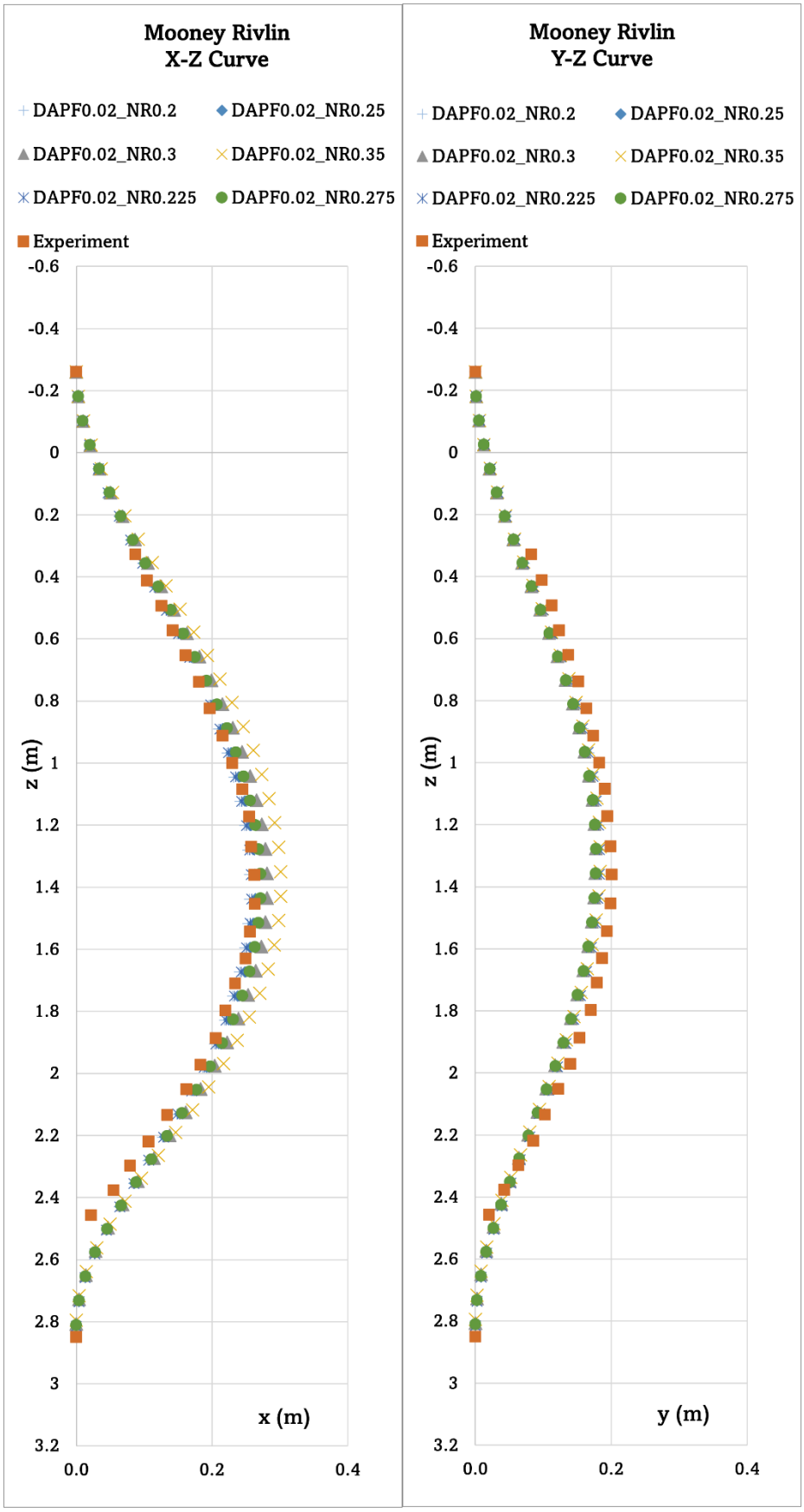

Fig. 5.19 Computational results with WOB fluctuation of Mooney Rivlin Model, ξ=0.02

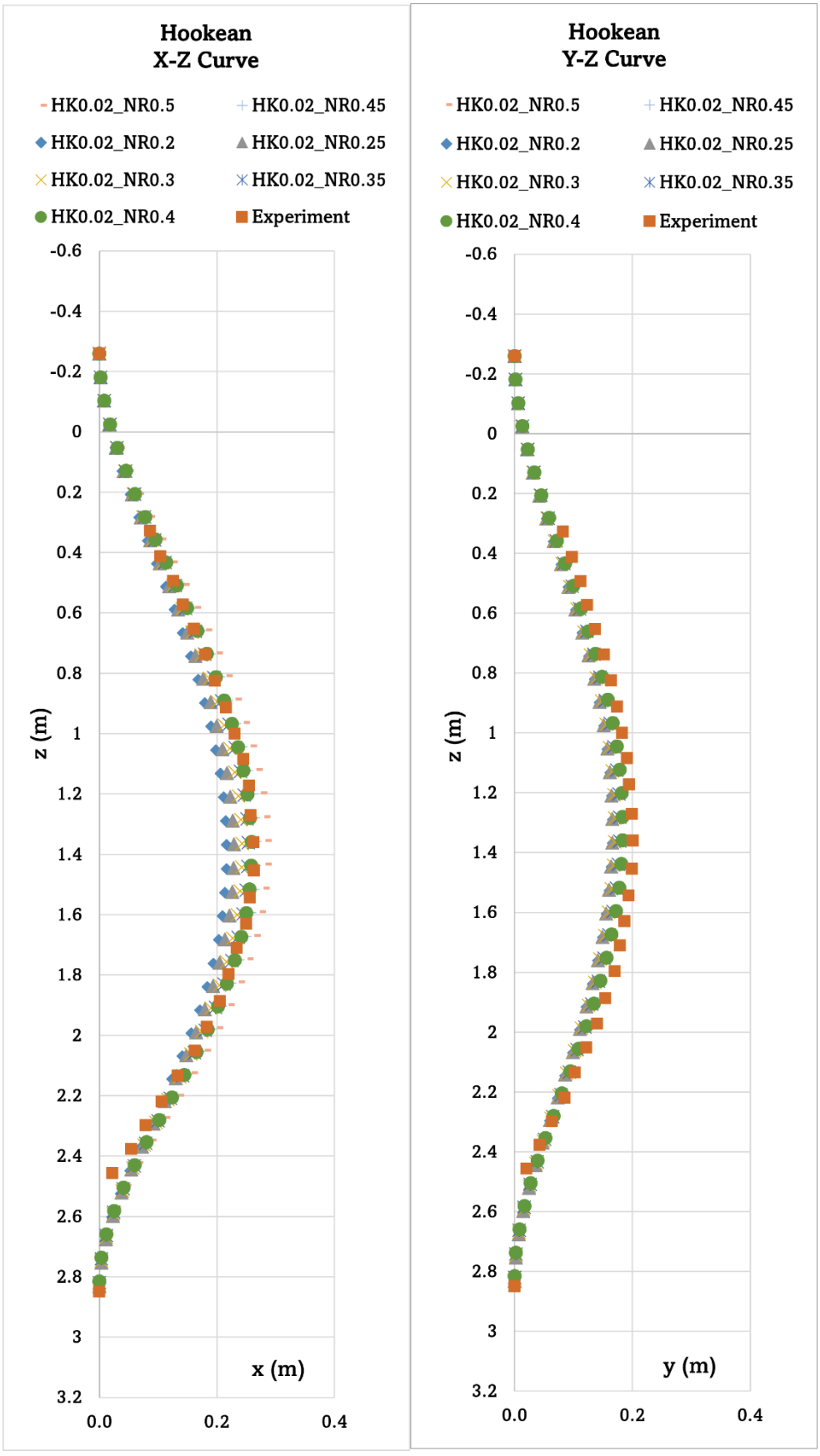

Fig. 5.20 Computational results with WOB fluctuation of Hookean Model, ξ=0.02

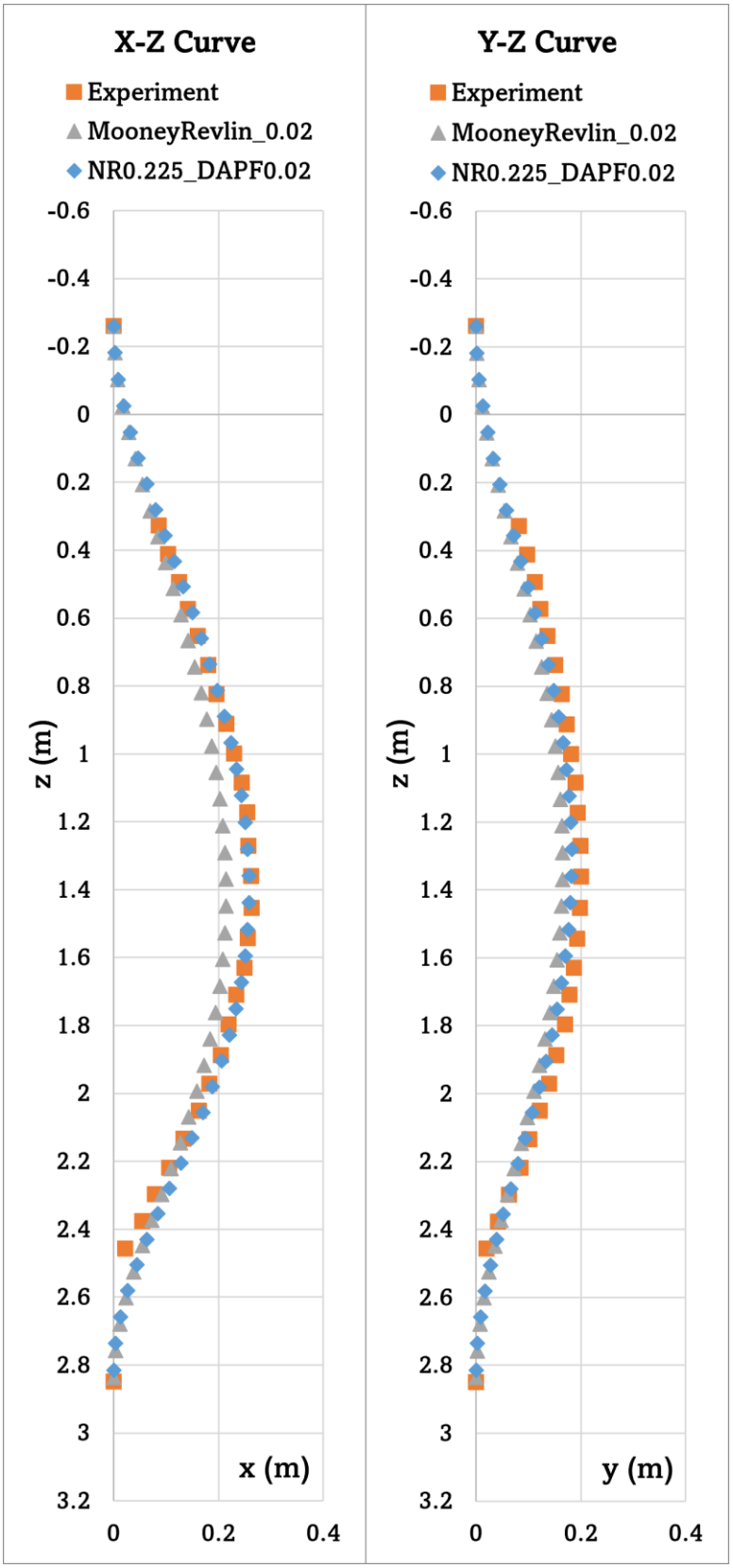

Fig. 5.21 Computational results comparison without WOB fluctuation (*NR*=0%) and with (*NR*=22.5%) in Mooney Rivlin Model, ξ=0.02

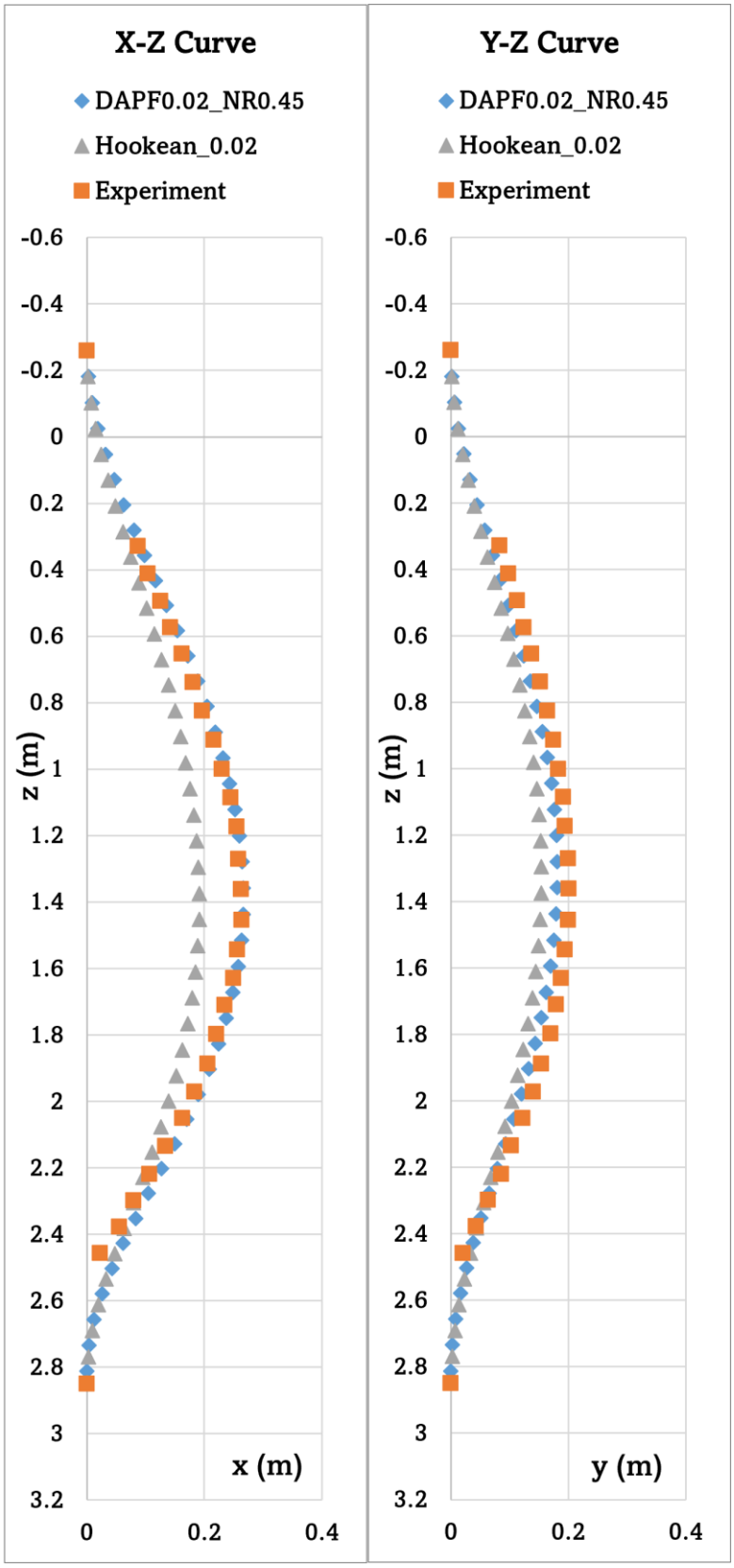

Fig. 5.22 Computational results comparison without WOB fluctuation (*NR*=0%) and with (*NR*=45.0%) in Hookean Model, ξ=0.02

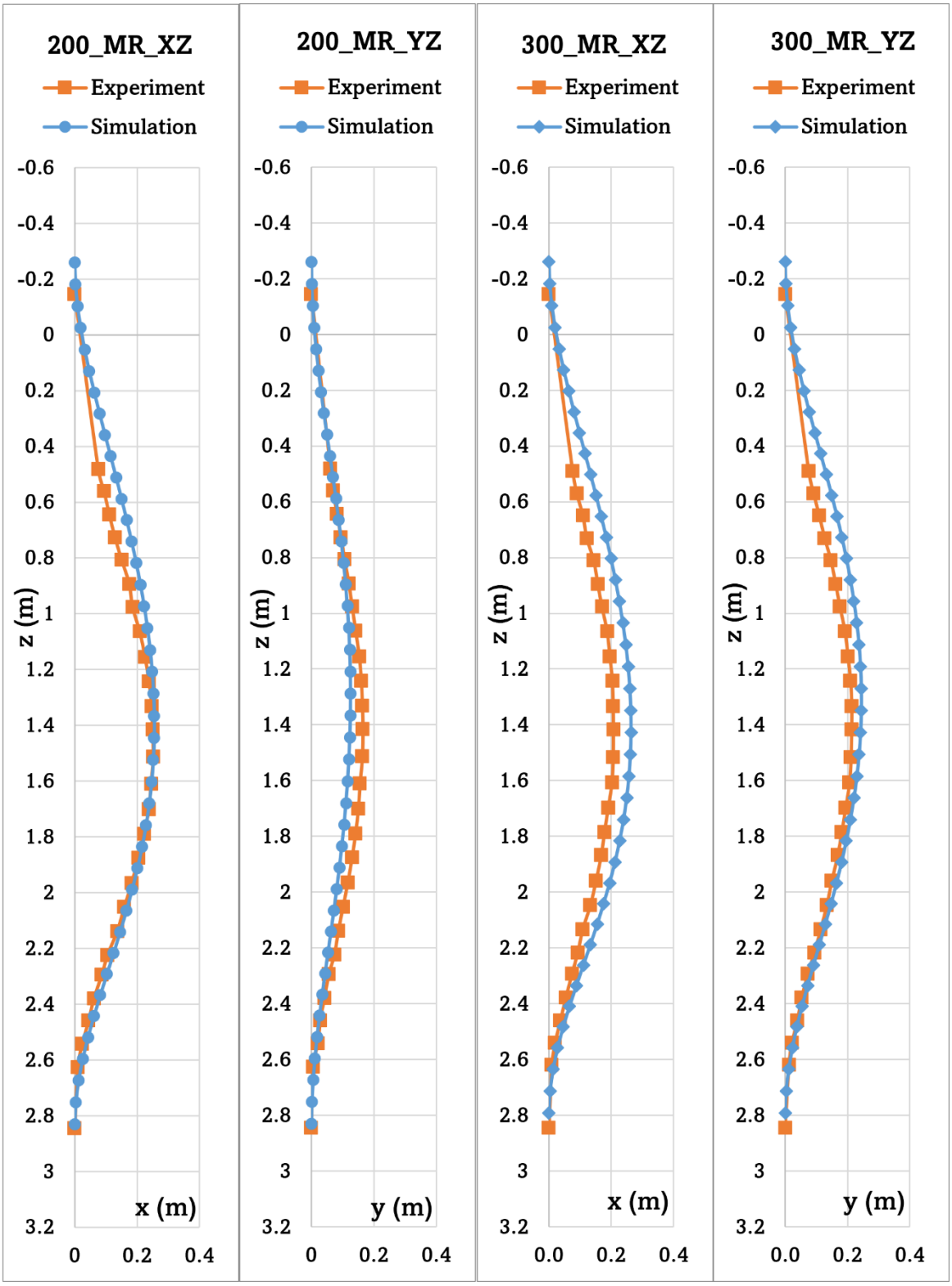

Fig. 5.23 Computational results for 200 and 300 RPM with (*NR*=22.5%) in Mooney Rivlin Model, ξ=0.02

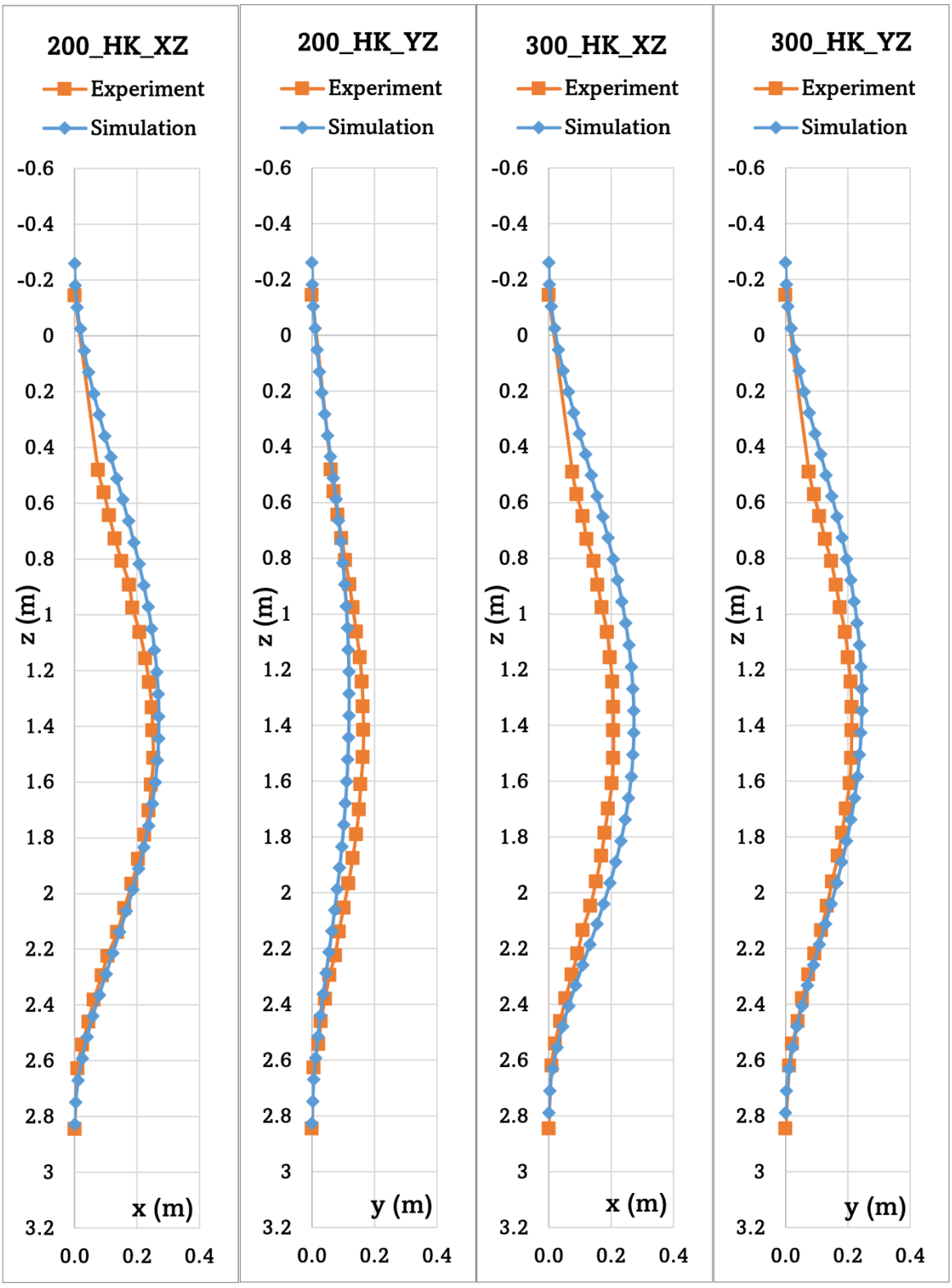

Fig. 5.24 Computational results for 200 and 300 RPM with (*NR*=45%) in Hookean Model, ξ=0.02

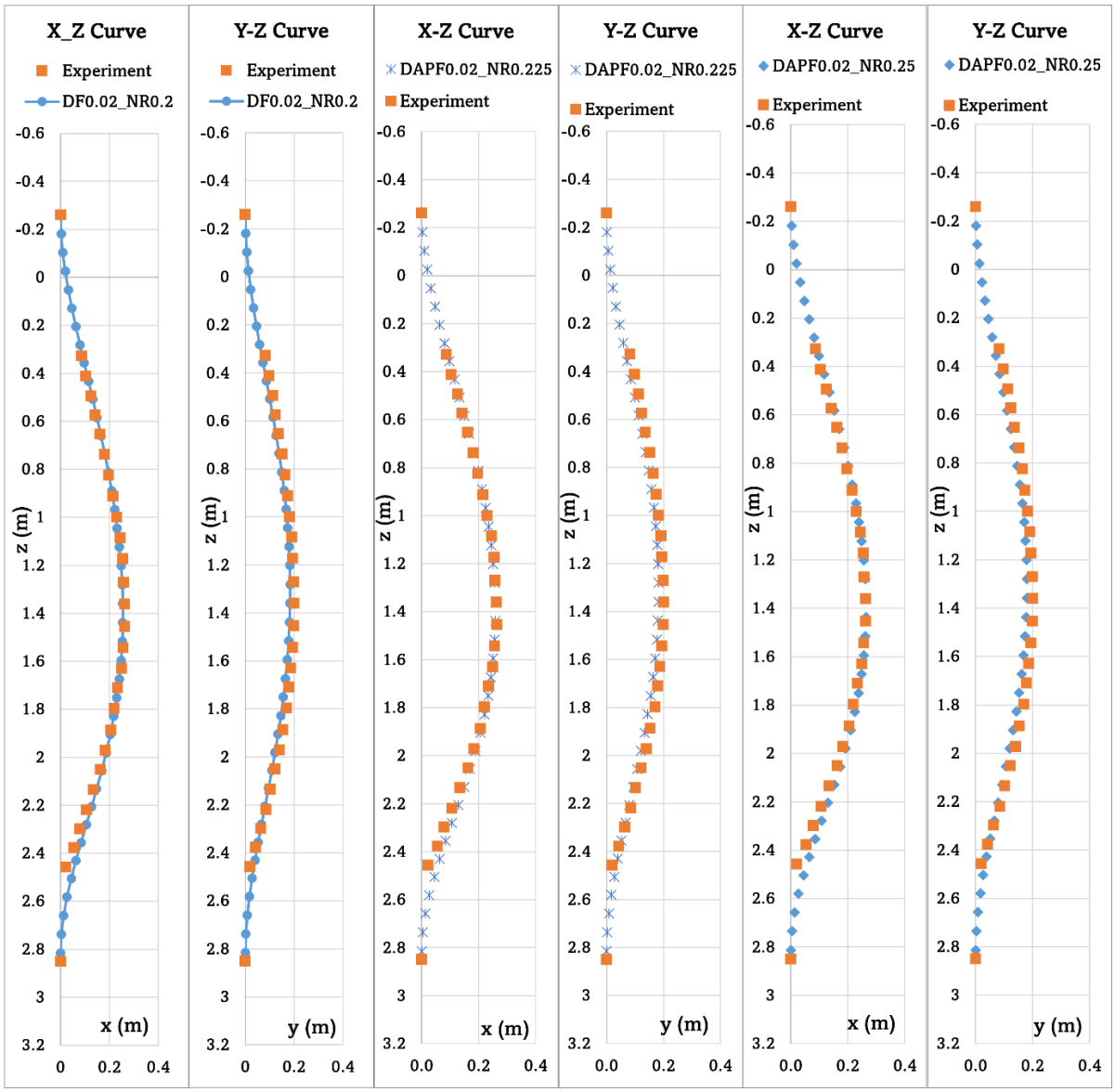

Fig. 5.25 Computational results for *NR* 20%,22.5%, and 25% for rotating drill pipe model

By using the 22.5% WOB in the Mooney Rivlin model and 45% WOB fluctuation in the Neo Hookean model, the drill pipe dynamic behavior analysis was carried out for 200 and 300 rpm for both material models and stated in Fig. 5.23 and 5.24 accordingly. At 200 rpm, both models show an acceptable range compared with the experimental results. On the other hand, the simulation results for 300 rpm in both model state that the *x*-displacement in simulation a little bit exceeds the values of the experimental result and the y-displacement still coincides with the experiment. Generally, the underwater behavior of the rotating drill pipe model in this case also describes better agreement with

the experimental results, and the application of proper damping constant and WOB fluctuation was observed.

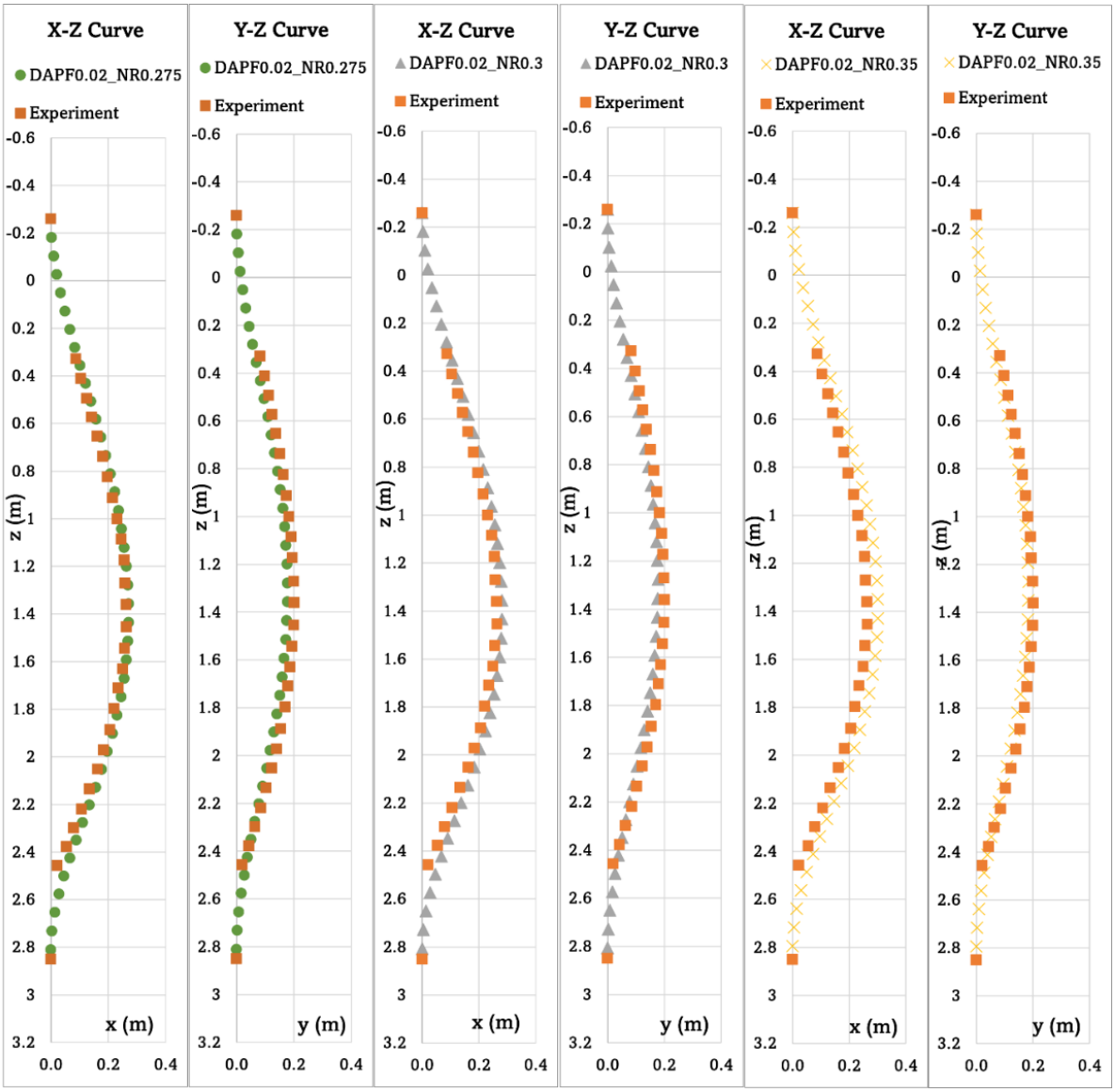

Fig. 5.26 Computational results for *NR* 27.5%, 30%, and 35% for rotating drill pipe model

In the previous study, (Suzuki et al., 2022) the WOB fluctuation of the non-rotating pipe model was discussed and analyzed accordingly and compared with the experimental results. Based on these facts, a comparative study was conducted on the WOB fluctuation ranging from 20% to 35% for the drill pipe model using the Mooney-Rivlin Model, as illustrated in Fig. 5.25 and Fig. 5.26. It has been studied that the application of WOB fluctuation between 20% to 35% shows better agreement with the experimental results. Both deformation profiles coincide with the experimental results. It was analyzed that the present simulation model can capture the deformations of the rotating drill pipe model straightforwardly by applying the proper damping constant and WOB fluctuation. The

results for the previous case (non-rotating drill pipe model) in Fig. 5.27 and the current study (rotating drill pipe model) in Fig.5.28 were studied by using 22.5% and 25% of the WOB fluctuation respectively. Compared to the previous studies, the improvement in the drill pipe model deformations was seen and the comparison studies of the current study in the consideration of hydrodynamic force consideration and the effect of internal viscous damping under WOB fluctuation was described in Fig. 5.29. Thus, it was proved that all the current simulation model shows reasonable agreement in capturing the dynamic behavior of the rotating drill pipe model simultaneously.

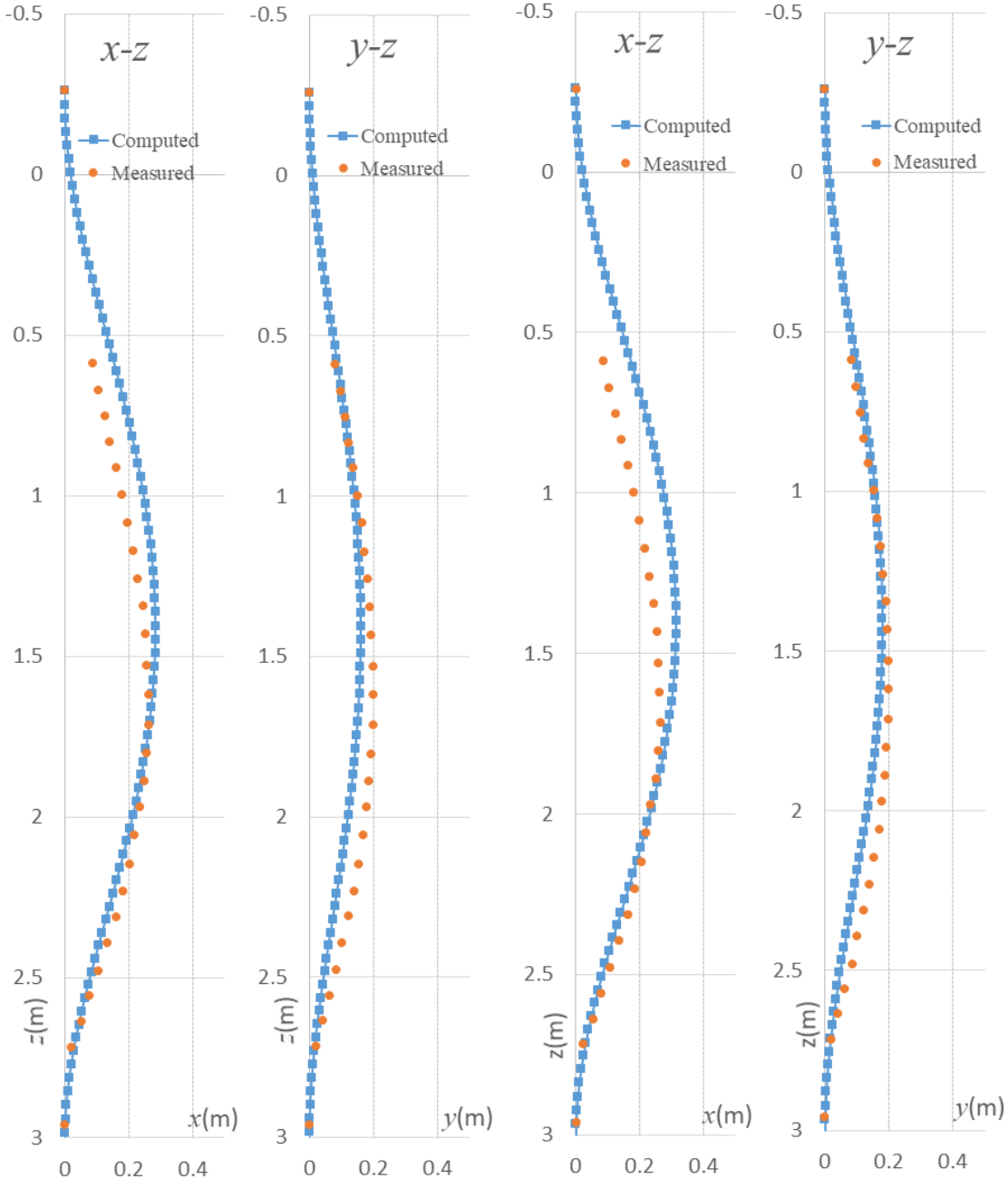

Fig. 5.27 Computational results for non-rotating drill pipe model with *NR* 22.5% and 25%

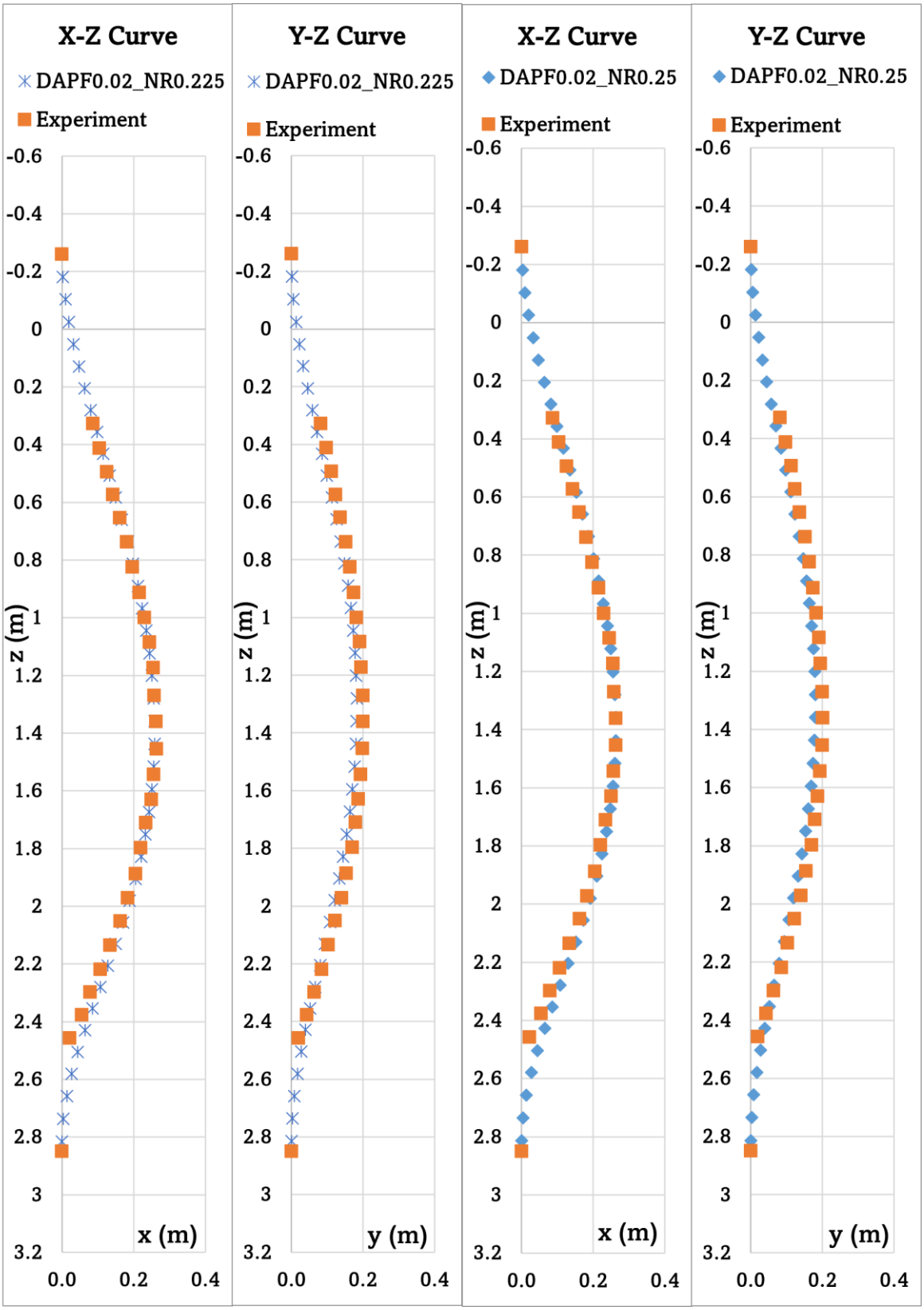

Fig. 5.28 Computational results for rotating drill pipe model with *NR* 22.5% and 25%

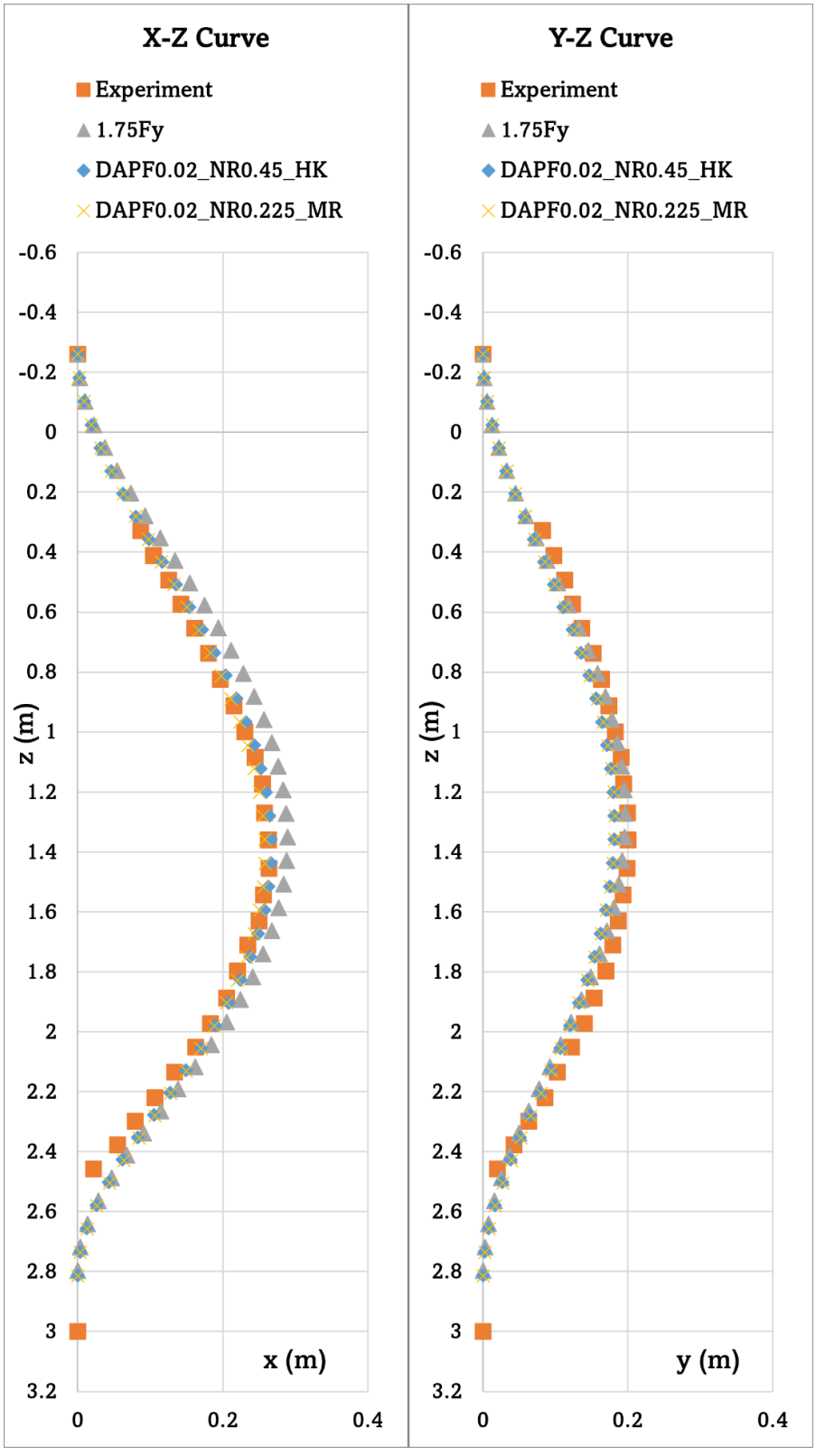

Fig. 5.29 Computational results comparison for rotating drill pipe model with 1.75*Fy* and damping constant, ξ=0.02, WOB fluctuation based on Mooney Rivlin and Hookean Models

Finally, the status of WOB fluctuation and the position of the drill pipe bottom position in the z direction was demonstrated in (Fig. 5.30) and the status of maximum x and y displacements with respect to WOB, ($NR\%$) was shown in (Fig. 5.31) respectively. Here, it was assumed that the amount of WOB would be equal to the amount of force exerted at the pipe bottom position, $NR\%$ which was formulated based on the percentage of the pipe's weight.

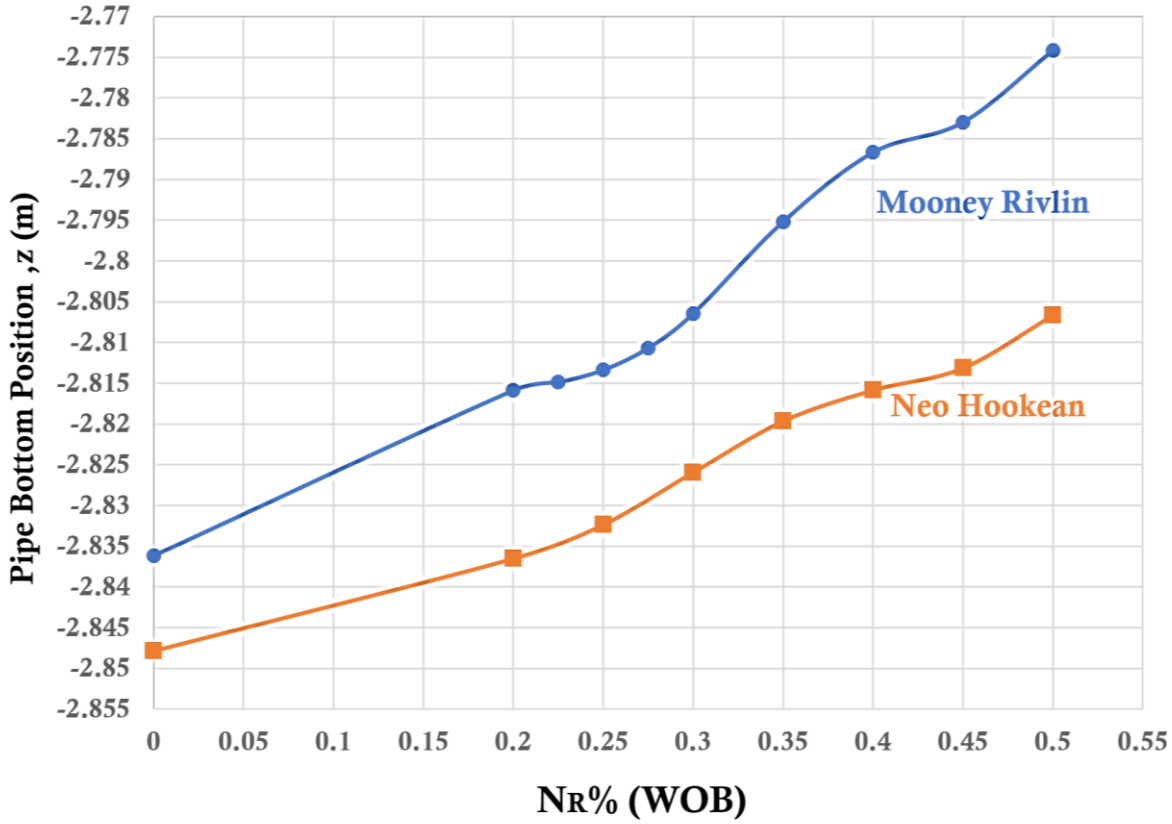

Fig. 5.30 Pipe bottom position status with WOB fluctuation

However, it was found that the percentage of the applied NR (WOB) was different based on the elastic models. In the Mooney Rivlin model, the pipe deformation coincided with the experiment results when 22.5% of N_R was applied to the pipe model, which means 22.5% of the pipe's weight was applied as the WOB at the bottom position of the pipe. But when we are modeling with the Neo Hookean model, the percentage of the WOB that should be applied for this model is 45%, which means that the percentage of N_R exerted on the pipe bottom is 45% of the pipe's weight as shown in (Fig. 5.30).

Moreover, the pipe bottom position shown in (Fig. 5.30) and the amount of maximum displacement in the x and y directions (Fig. 5.31) show that the Neo Hookean model has shown more stiffened properties with less deformations than the Mooney Rivlin model

under the same WOB fluctuation. It was observed that the current model could capture the lifting effect of the pipe bottom position due to the bending deformation and *NR*%. Since the positions in *x*, *y,* and *z* increase due to the applied *NR*% as shown in (Fig. 5.30), the effect of WOB on the dynamic behavior of the rotating drill pipe model could also be analyzed.

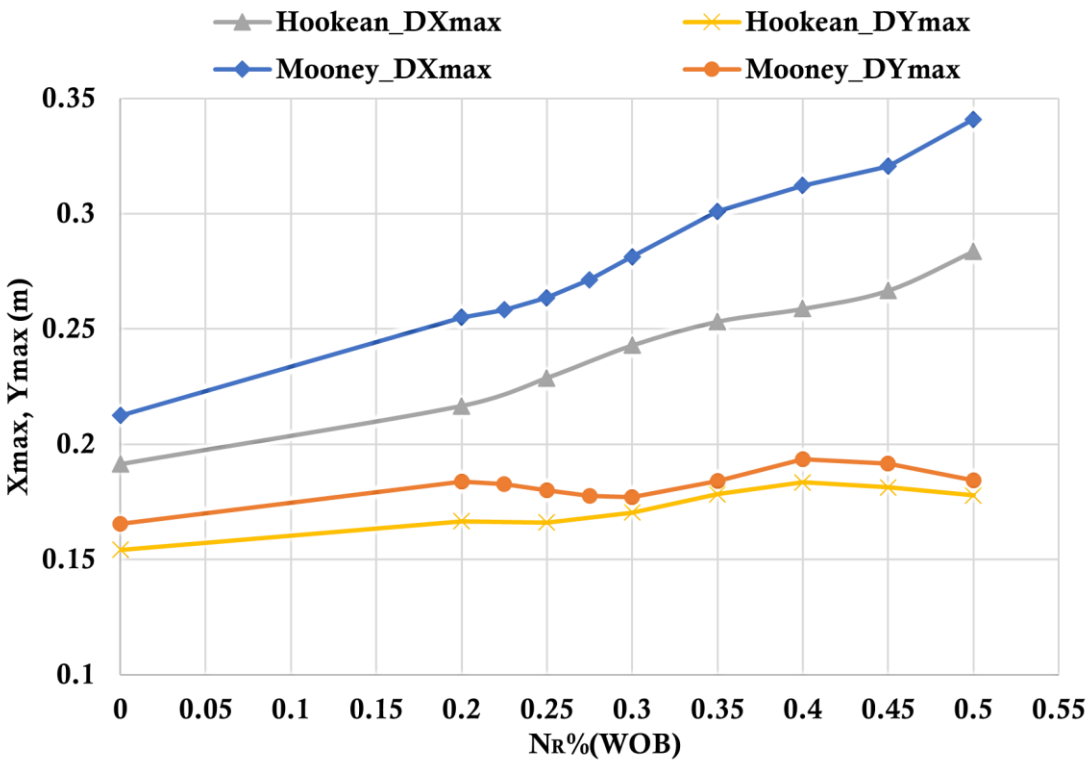

Fig. 5.31 Maximum displacements in *x* and *y* directions with WOB fluctuation

Nonetheless, the considerations of the performance of the hydrodynamic force model and the effect of the internal viscous damping model with respect to the use of the hyper-elastic material models for the rotating drill pipe model were implemented in this study. In addition, the numerical simulation results can be validated properly with the results obtained in the experiment for different rotational velocities of the pipe model.

Therefore, it is proposed that the current simulation model for the rotating drill pipe model could be a reference study for the implementation of the study of the dynamic behavior of the actual scale drill pipe applying the ANCF scheme which is operated in current drilling operations.

Chapter 6

Preliminary Study of the Underwater Behavior of the Actual Drill Pipe in the Uniform Flow by Applying ANCF Simulation

6.1 Calculation Conditions for ANCF Simulation

In this chapter, the application of the ANCF simulation model for the rotating drill pipe model in uniform flow was introduced to implement the study of the actual scale drill pipe model in real drilling operations. Based on the study of (Inoue et al., 2017), the current simulation model applying the 24-DOF ANCF beam element which can account for the pipe rotary inertia and the cross-sectional deformation modes such as torsion and shear deformation, was implemented to capture the schematic of the real drill pipe situations. The computational particulars for the reference case and the 2-simulation study cases for the study of dynamic motions of the drill pipe. In addition, the same length of the drill pipe was considered as the full scale in study case 1, and the length with $1/10^{th}$ scale of the full scale with the same element number was analyzed and discussed in study case 2 as shown in Table 6.1.

Table 6.1 Computational parameters for the actual scale drill pipe

Main Particulars	**Reference Study**	**Study Case 1**	**Study Case 2**
Length of the pipe (m)	1423	1423	142.3
Length of the pipe in air (m)	N/A	50	5
Diameter of the pipe, outer (m) and inner (m)	0.1397,0.1140	0.1397,0.1140	0.1397,0.1140
Element length (m)	0.5	25	0.5
Number of elements (nodes)	2846(2847)	60(61)	295(296)
Density of seawater (kg/m^3)	1025	1025	1025
Rotational velocity (*RPM*)	60,12,180	150	150
Flow velocity (m/s)	0.05-0.7	0.5144	0.5144
N_R %, WOB fluctuation	N/A	0%	0%
Damping factor, ξ	N/A	0.05,0.08	0.08
ANCF Beam Element	6DOF	24DOF	24DOF

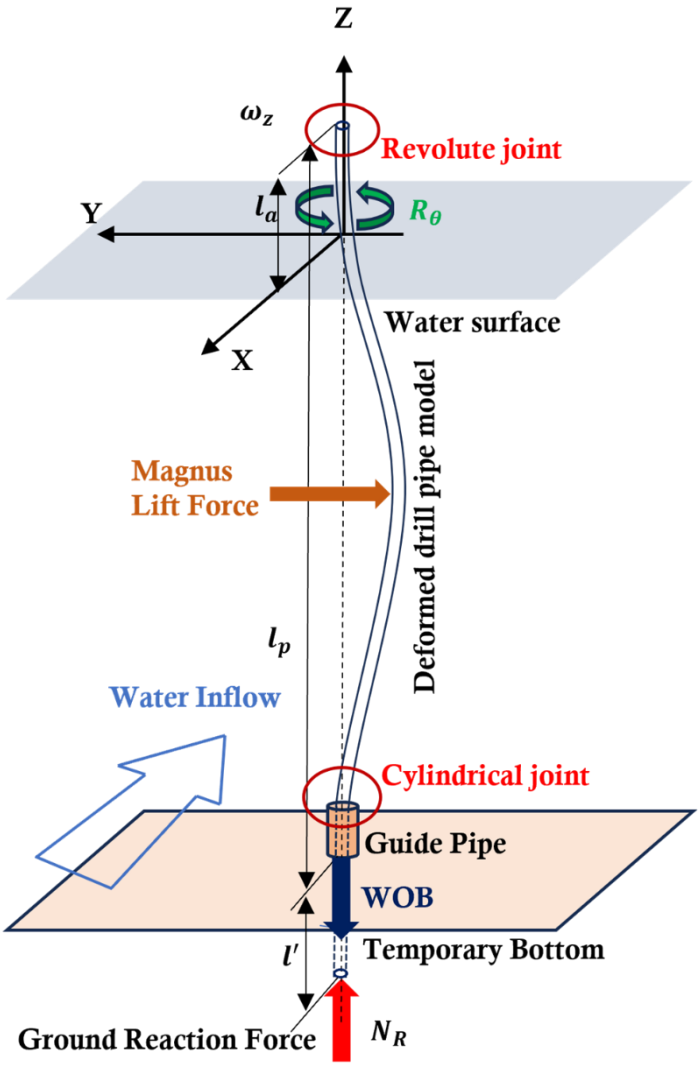

Fig 6.1 Computational setup for the ANCF simulation of the drill pipe

To consider the underwater behavior of the drill pipe in real scale, the same condition of the rotating drill pipe model computational setup was applied as shown in Fig. 6.1. The upper joint will be considered as the revolute joint and the lower end is cylindrical with free move in *z* direction. The deformation related to resistance will be captured in the *x*-direction and the y-deformation due to magnus life force will be captured based on the flow velocity and rotational velocity mentioned in Table 6.1 accordingly.

Based on the computational parameters shown in Fig. 6.1 and Table 6.1, the deformation of the drill pipe in uniform flow due to the Magnus effect was analyzed by using the three-dimensional fully parameterized beam element, and the computational results for each study case were evaluated and discussed respectively.

6.2 Dynamic behavior of the drill pipe in full scale: Study Case (1)

6.2.1 Study Case 1 (damping constant 0.05)

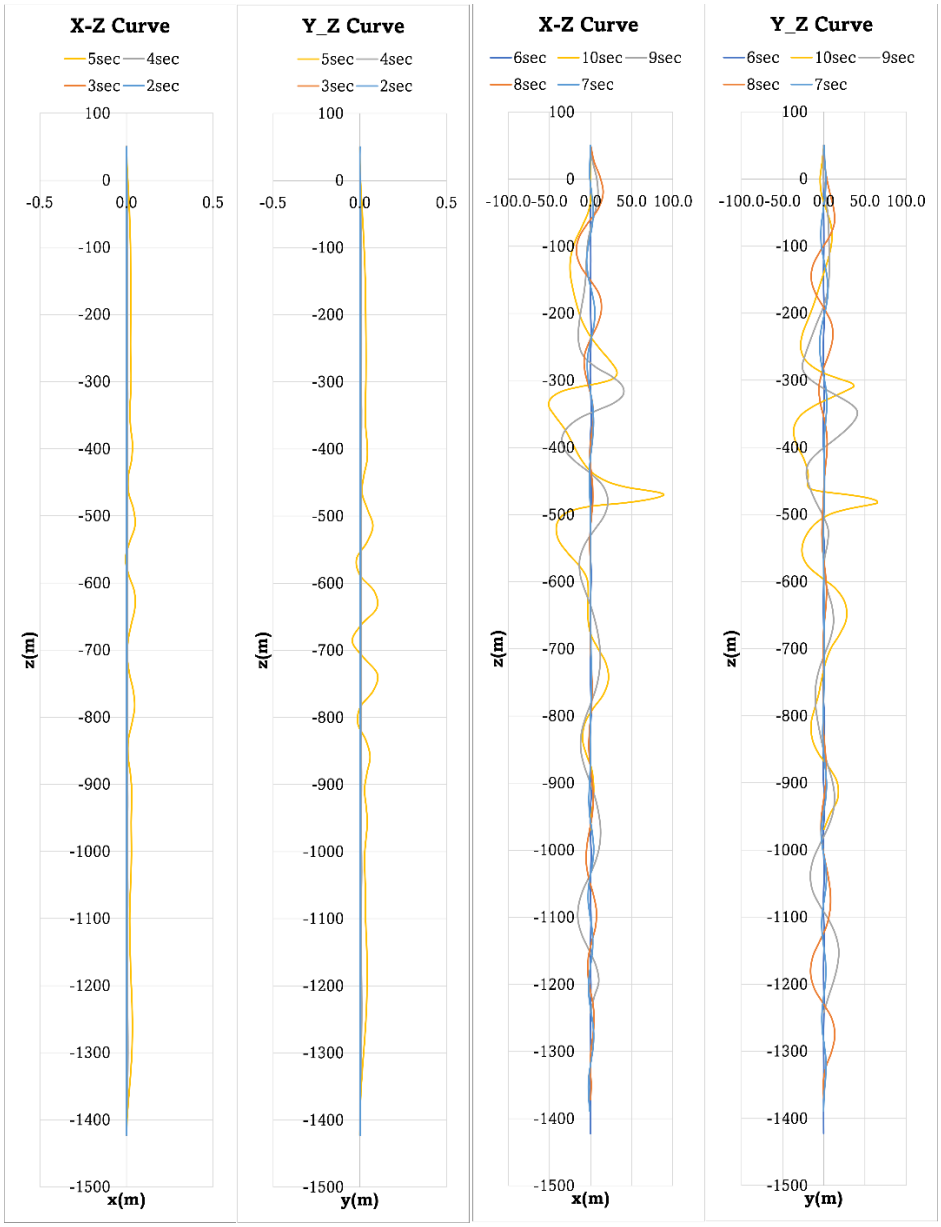

(a) (b)

Fig. 6.2 Dynamic behavior of the full-length drill pipe, damping constant 0.05, *NE* 60

These computational results were carried out based on the damping constant 0.05 and the simulation time is 10 sec for the whole simulation. In this case, the hydrodynamic forces started to apply at 2 sec and the drill pipe fluctuation started at 5 sec and the deformation until the 5 sec hasn't been found significantly yet. The lower part of the pipe remains unchanged as per the preliminary boundary conditions. The maximum deformation of the *x* and *y* direction couldn't be captured well in this stage as shown in Fig. 6.2 (a).

Meanwhile, the calculation results of the study case 1, starting from time steps of 6 seconds to 10 seconds state that the deformation profiles fluctuate significantly within the length of the 700m under the water surface. The drill pipe deformation and the dominant lifting force in the lower part of the pipe boundary were found starting from 7second to 10 seconds, as shown in Fig. 6.2 (b) except for the simulation result for 6 seconds. On the other hand, similar deformation profiles for the x and y directions were found at the 6-sec simulation time step as shown in Fig 6.3.

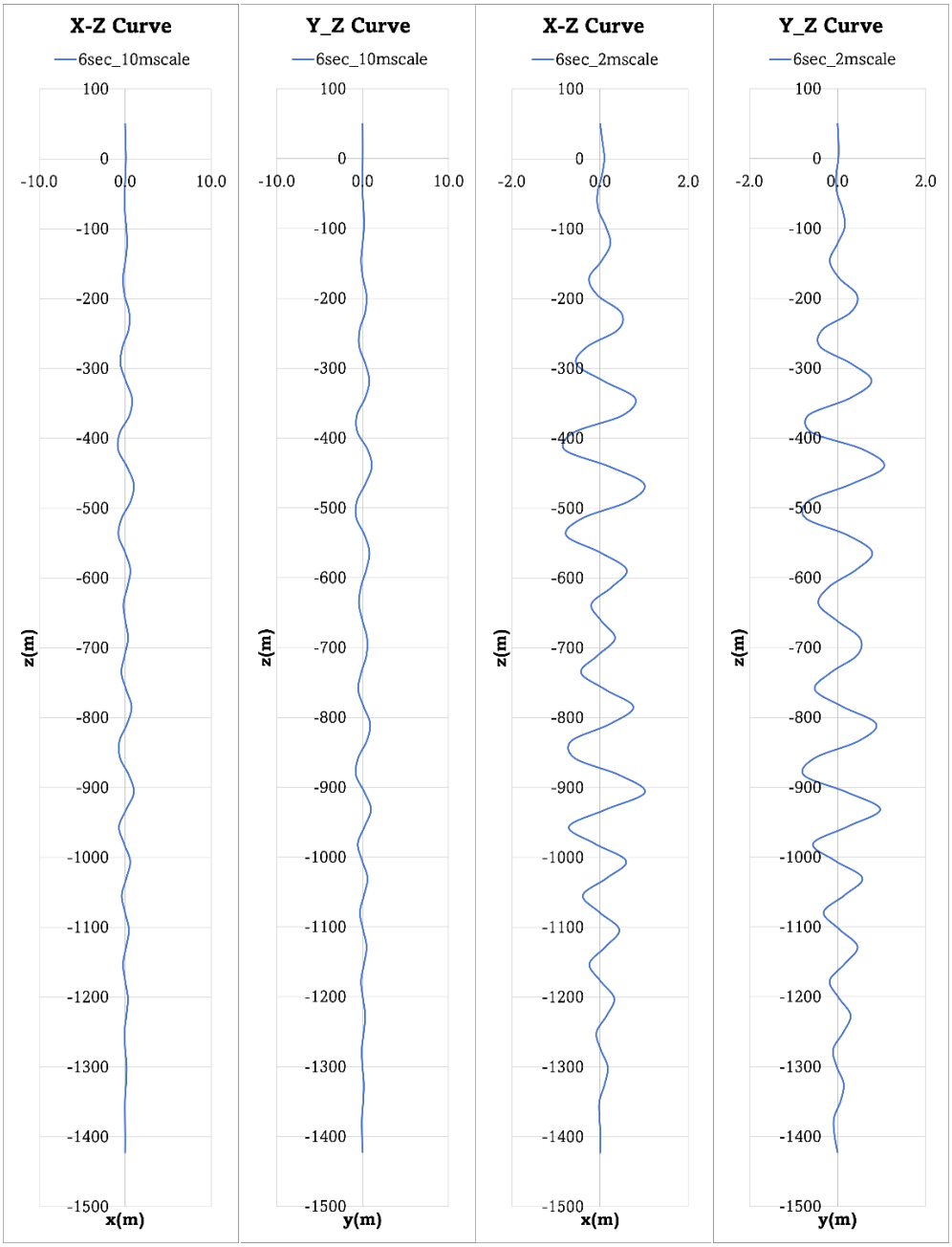

Fig 6.3 Computational results for 6-sec time step for the drill pipe, damping constant 0.05

6.2.2 Study Case 1 (damping constant 0.05 and new hydrodynamic force)

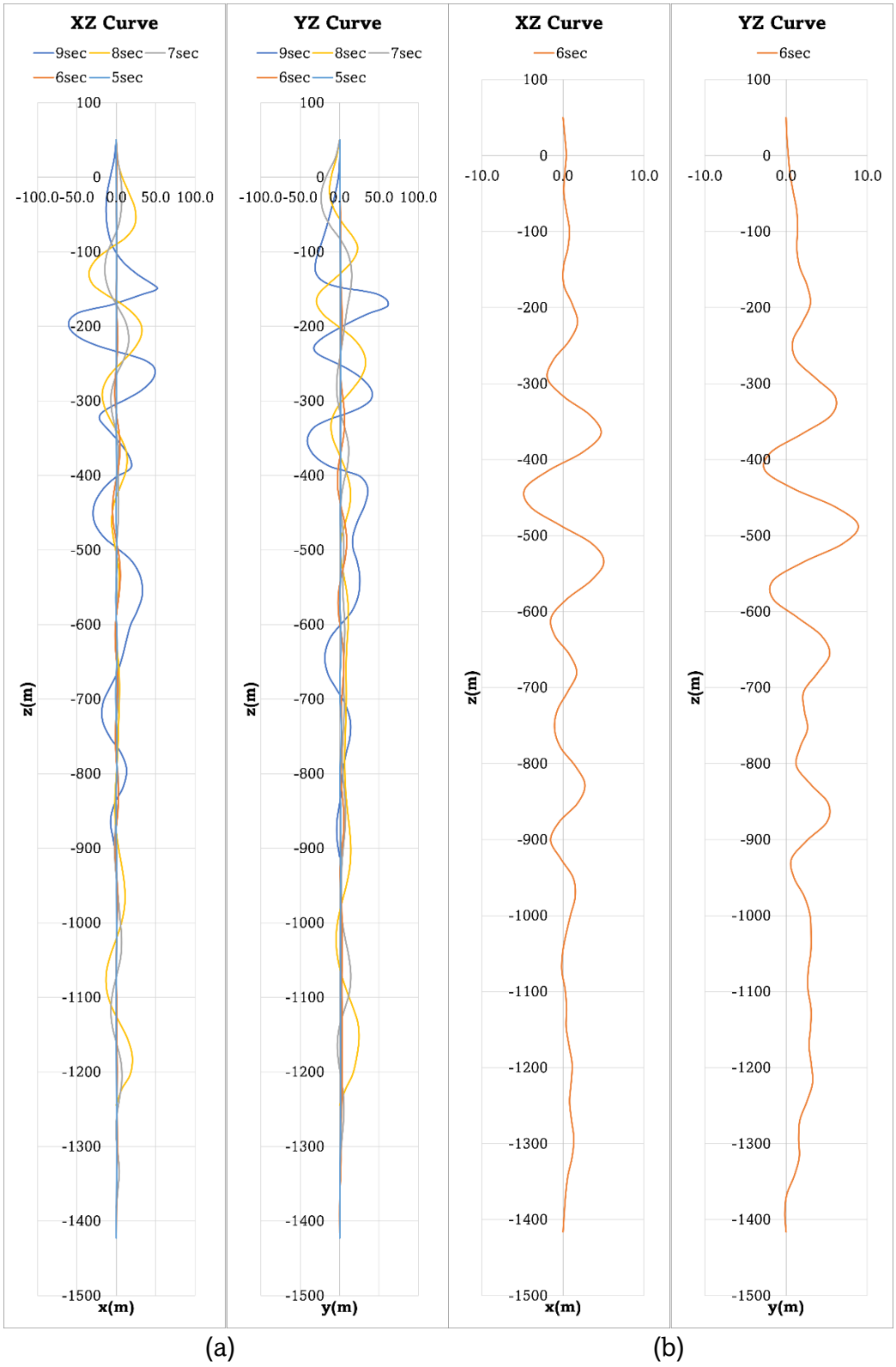

Fig. 6.4 Dynamic behavior of the drill pipe by applying the new hydrodynamic force, with damping constant 0.05

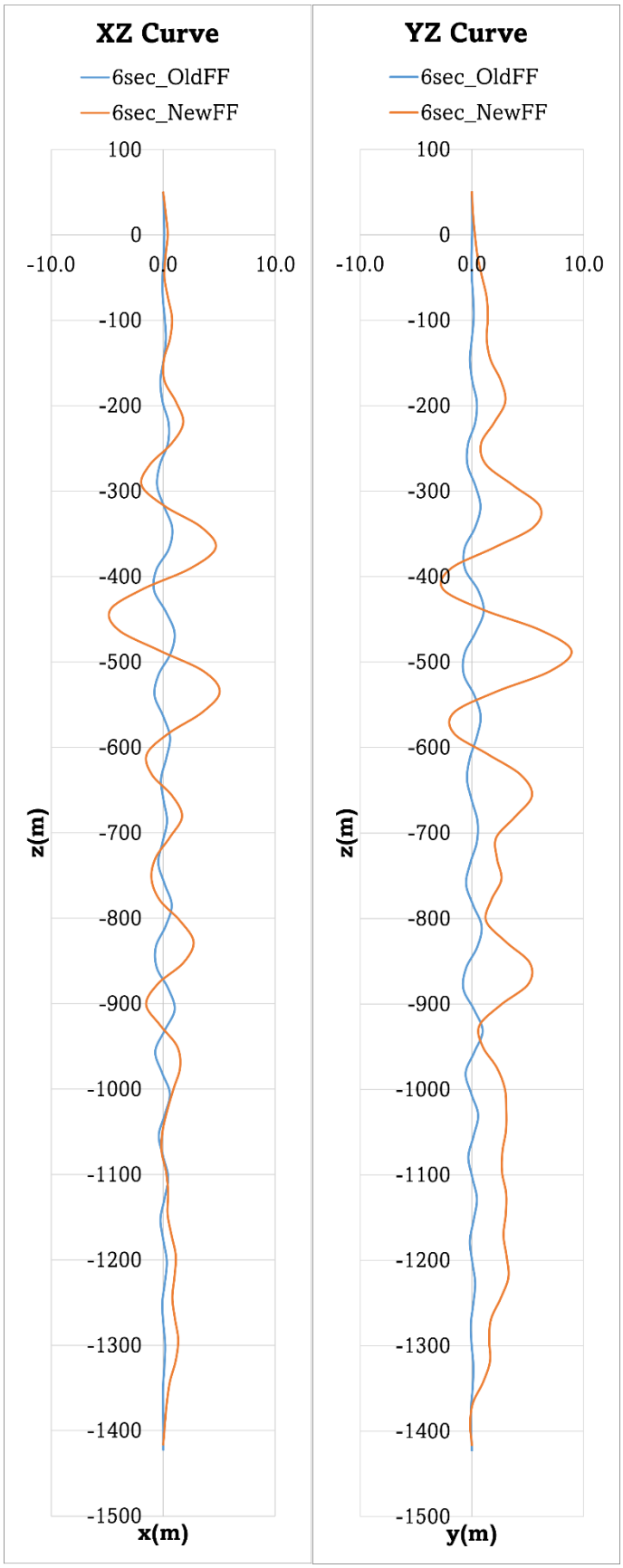

Fig. 6.5 Computational results comparison for hydrodynamic force with damping constant 0.05

Since the hydrodynamic performance of the actual drill pipe behavior should have been studied for capturing the dynamic performance of the rotating drill pipe, the modified hydrodynamic forces for the actual drill pipe were developed according to Chapter 4 and applied to the current simulation model, the detailed results of the application of new hydrodynamic force of the drill pipe were demonstrated in Fig. 6.4 (a) and the calculation time of 6sec profile was selected and shown in Fig. 6.4 (b).

To know the hydrodynamic performance of the present simulation model, the comparison study of the results for previous hydrodynamic force and new hydrodynamic forces are mentioned in Fig. 6.4. It was observed that the new hydrodynamic force model has a significant effect on the deformation of the drill pipe and the maximum deformation occurred around 500m length of the drill pipe in both models. However, the lift component of y-displacement is a greater value than the x-displacement in the new hydrodynamic force model.

6.2.3 Study Case 1 (damping constant 0.08 and new hydrodynamic force)

Since the actual drill pipe is made of steel structures and shows stiffened properties than the elastic material pipes, here, we assumed the damping constant as 0.08 and the dynamic behavior of the drill pipe was found in Fig. 6.5 and the comparison of the using of different damping constant was presented in Fig. 6.6 for 6sec simulation time step respectively.

Generally, the drill pipe with a damping constant of 0.08 states that the maximum displacement occurred around 800 m and 900 m in length from the water surface. Based on the simulation time steps, the deformation profiles in x and y changed accordingly and the position of the maximum displacement occurring is also changed according to the time and conditions of the computational model.

To sum up, for study case 1, the deformation of the drill pipe can capture the deformed shape based on the hydrodynamic force and consideration of the damping constant, but the calculation accuracy of the drill pipe should also have been optimized by using the small element numbers with many node points. Therefore, the dynamic behavior of the drill pipe with a small element number will be discussed and analyzed in the Study Case (2).

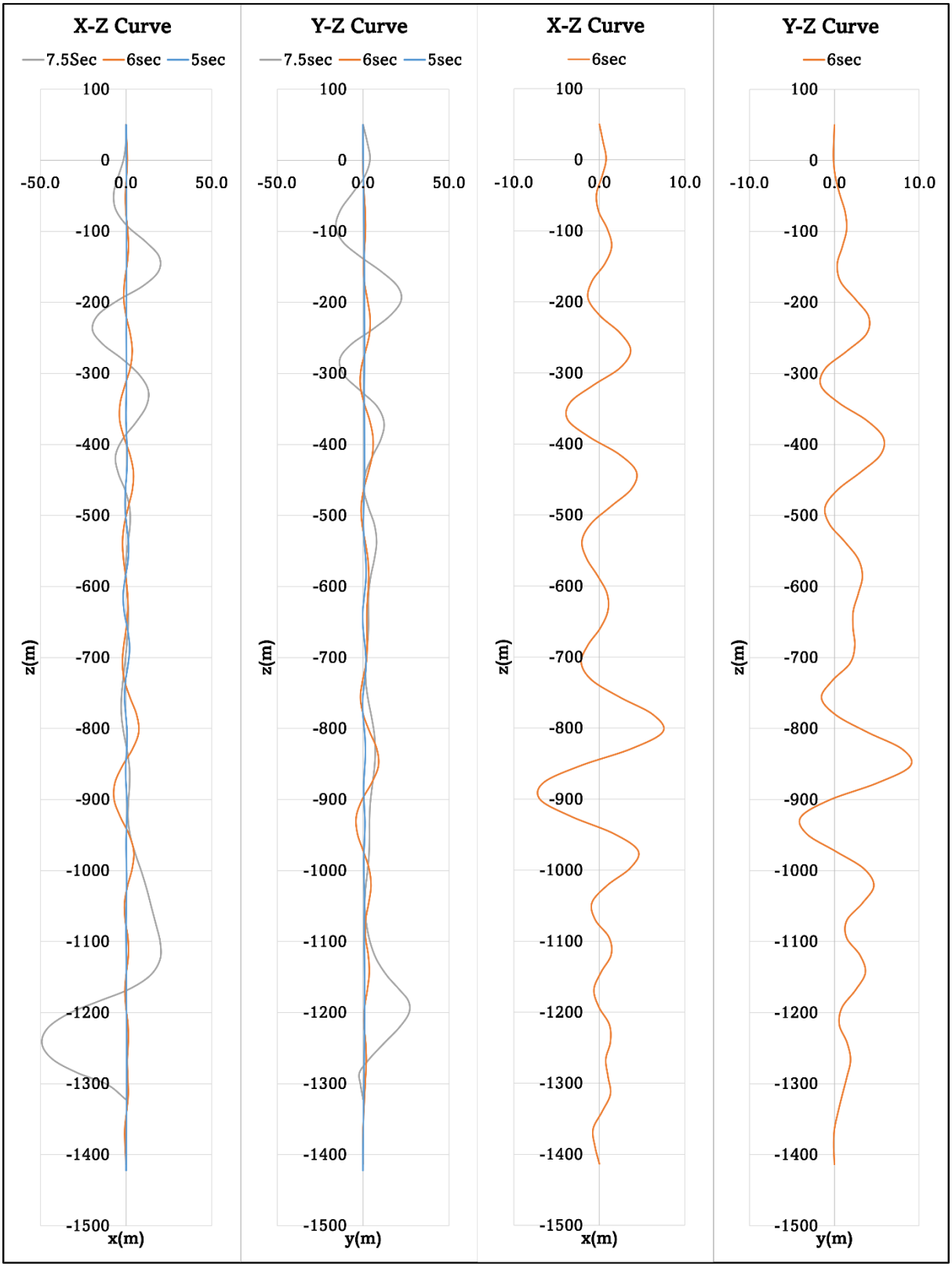

Fig. 6.6 Dynamic behavior of the drill pipe by applying the new hydrodynamic force, with damping constant 0.08

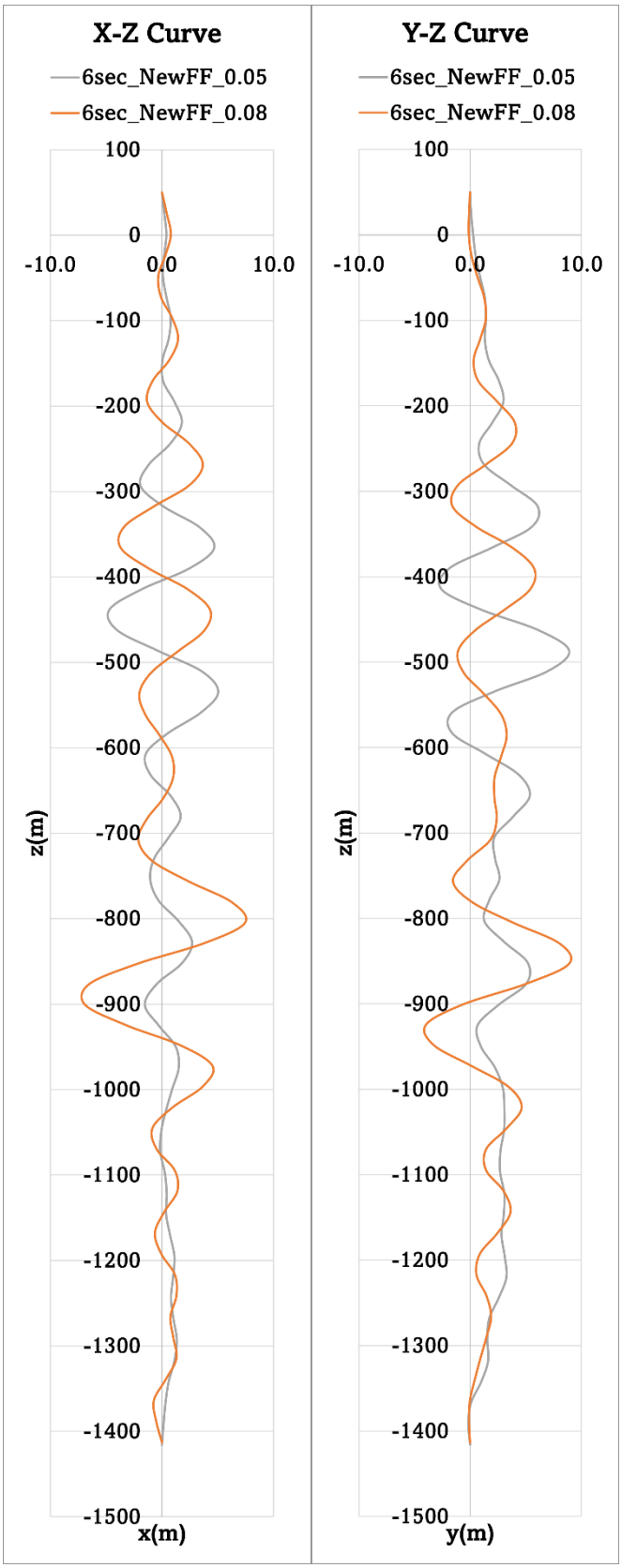

Fig. 6.7 Computational results comparison of damping constant, 0.05 and 0.08 with new hydrodynamic force model

6.3 Dynamic behavior of the drill pipe in $1/10^{th}$ scale: Study Case (2)

To study the real-scale drill pipe with a small element length in the current simulation model, the computational cost and time will be the merits that we should consider for computing the real-scale model. Therefore, the $1/10^{th}$ scale model of real size pipe of reference case, (Inoue et al., 2017), pipe length of 142.3m with a damping constant of 0.08, for a 5-sec simulation time step was analyzed and discussed as a reference case for a rotating drill pipe model research in the future study with 24-DOF ANCF beam element for each some time steps of the simulation model.

By using the computational parameters mentioned in Table 6.1, the study case (2) was conducted, and the computational results were shown in Fig. 6.7. The x and y displacements were not dominantly seen until the 4sec simulation time, and the predominant deformation was found at 5 sec as shown in Fig. 6.7. According to Fig. 6.8, the computational results for 4 and 4.5 sec shows that the amount of deformation in y-direction is greater than the x-deformation in both cases. The deformation profiles in both cases are stable and the effect of the Magnus lift force can be captured in both cases properly.

Moreover, the computational results of the 5-sec simulation showed that the deformation profiles in x and y became larger according to the simulation time step accurately. The y-displacement which represents the Magnus lift force also has a greater magnitude than the x-deformation in the 5-sec time step. The maximum displacement occurred around 80 m of the drill pipe and it was the same position in Case 1, which happened around 800 m for a damping constant 0.08 in the previous study.

Therefore, from this study cases, it can be concluded that the deformation profile and calculation accuracy are greatly dependent on the number of elements of the computational model. In addition, the maximum displacement position and the overall deformations are different according to the damping constant of the pipe. The configuration of the drag and life profiles in x and y displacements could capture well for each time step. Finally, it is proposed that the dynamic behavior of the drill pipe in uniform flow due to the Magnus effect could extend from the current simulation model in Case

Study (2) as a reference case, by considering the different approaches and methods to implement the real drilling situation appropriately.

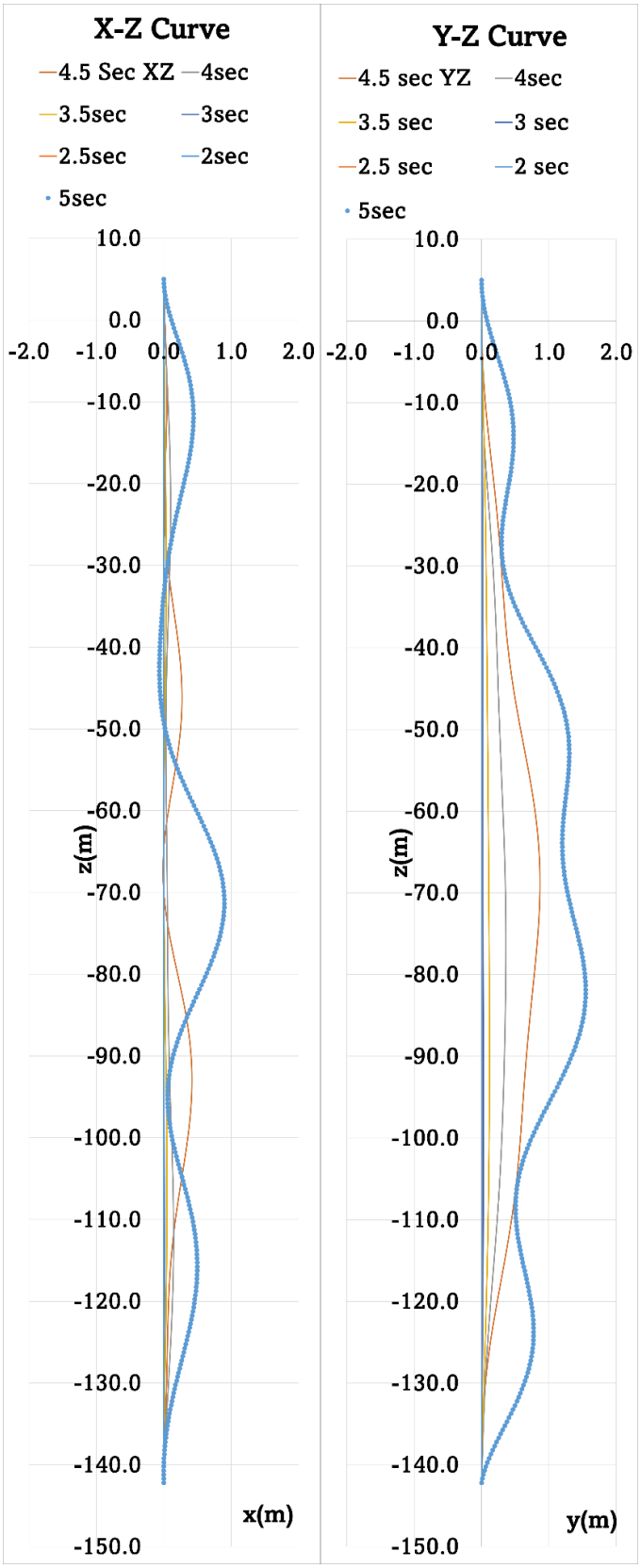

Fig. 6.8 Dynamic behavior of the $1/10^{th}$ scale drill pipe with damping constant 0.08

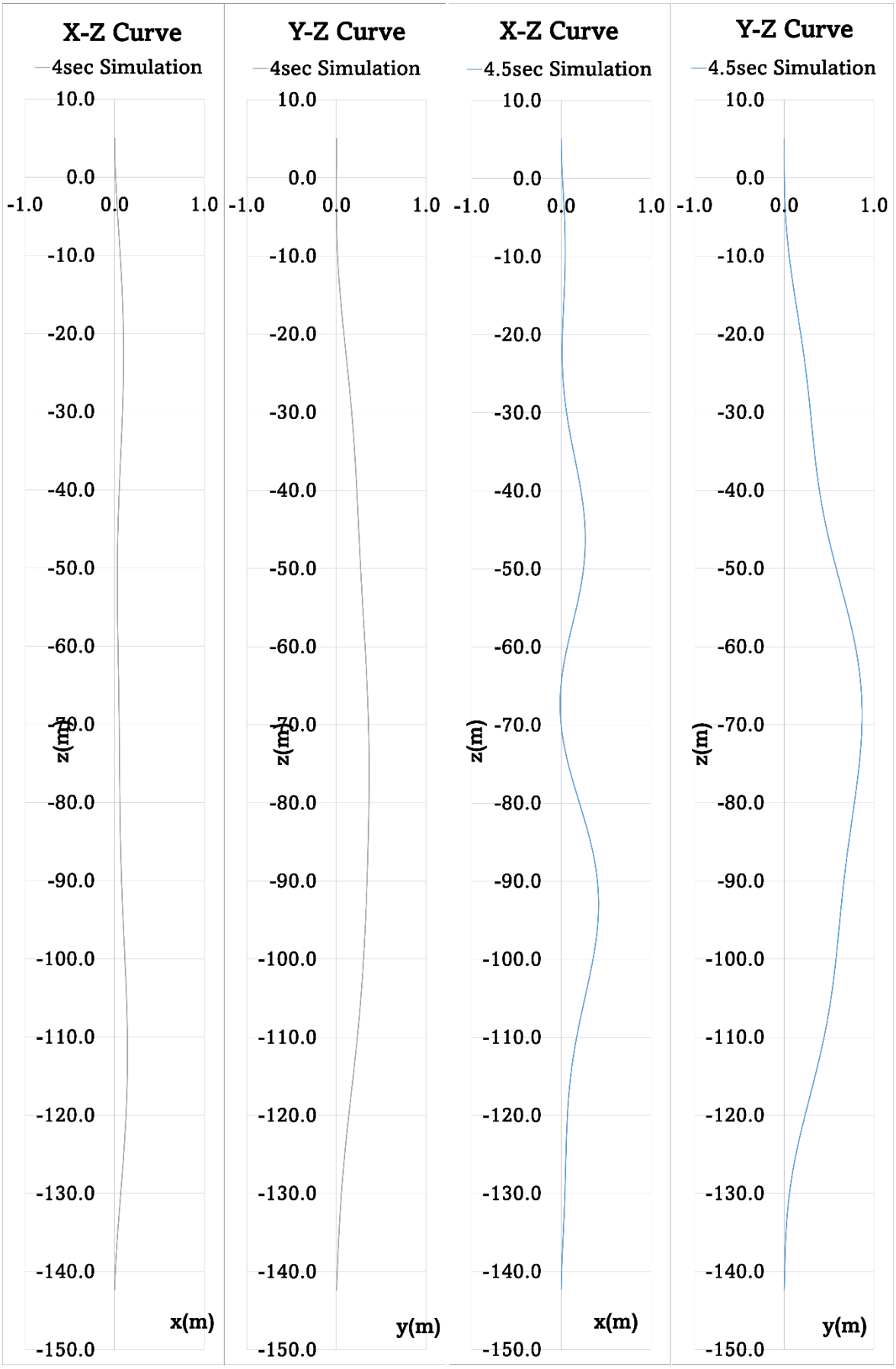

Fig. 6.9 Computational results for 4 sec and 4.5 simulation time steps

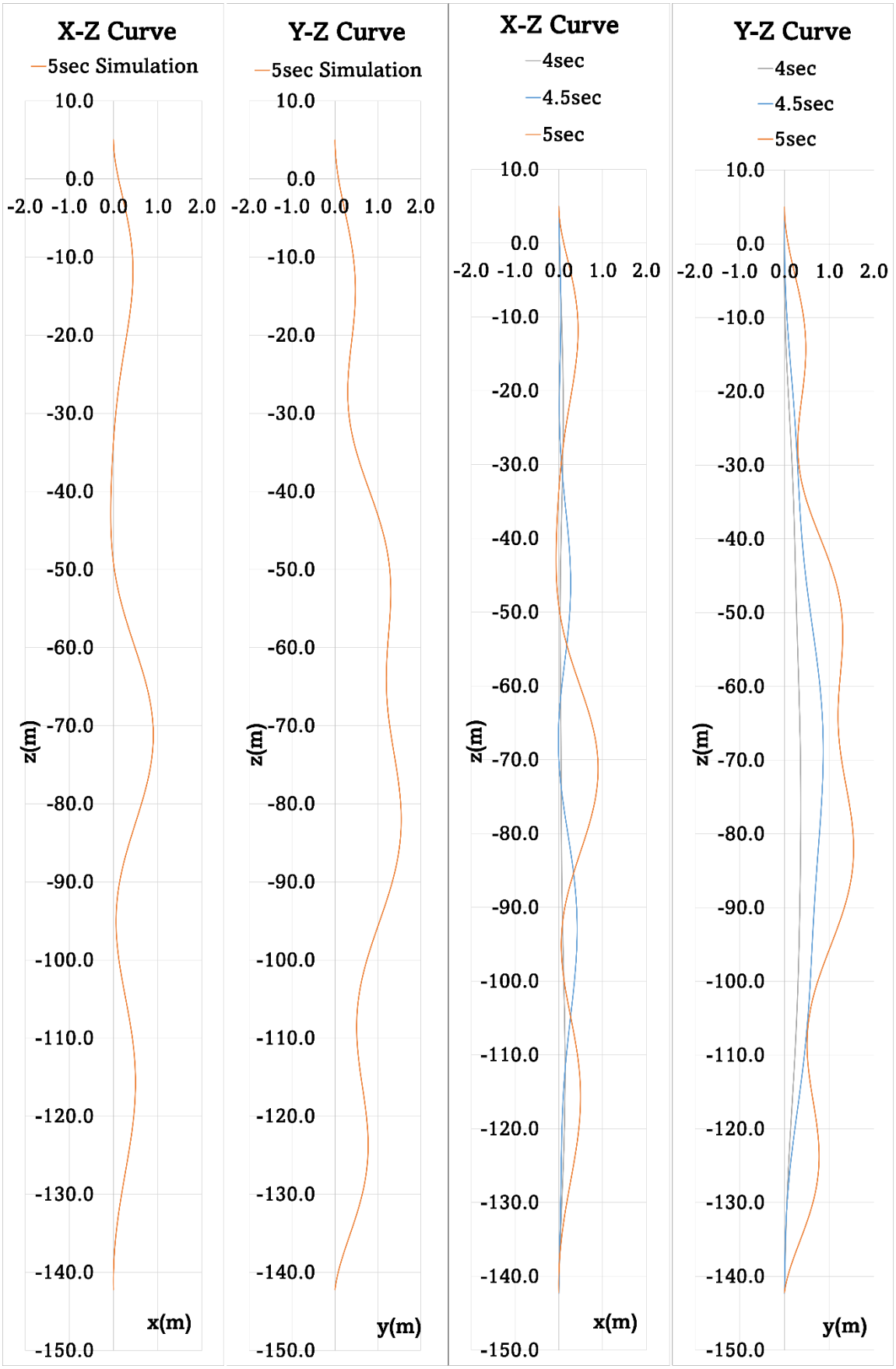

Fig. 6.10 Computational results for 5sec and results comparison for different time steps

Chapter 7

Conclusions and Future Works

7.1 Conclusions

In this study, the nonlinear dynamic motion of the rotating drill pipe has been investigated by considering the gyroscopic effect and rotary inertia with a new hydrodynamic force model for the rotating drill pipe model. This study also contributes to understanding the influence of Magnus effect parameters on the motion of the underwater drill pipe. The underwater behavior of a drill pipe model rotating in a uniform flow was investigated from numerical simulation and compared and validated to the results obtained from previous experimental measured values.

The hydrodynamic force acting on the tilted rotating cylinder was obtained by CFD analysis (ANSYS Fluent), and the underwater behavior of the drill pipe model was estimated by using ANCF. The results obtained from the consideration of different hydrodynamic forces exerted on the drill pipe model can be summarized as follows.

1) The results of CFD analysis show that *Fx* tends to decrease with the increase of the oblique angle, *Fy* tends to increase with the increase of the oblique angle, and *Fz* depends on both tilt and oblique angle. By using the estimated fluid force distribution, the interpolation function of the orientation of the pipe, tilt angle, θ, and the oblique angle, α was obtained.

2) ANCF was used to estimate the displacement of a rotating drill pipe model in a uniform flow. It was found that the displacement values obtained by increasing the fluid force in the y component 1.75 times compared to the original values, Case 4, got the optimum results for both *x* and *y* displacements for the rotating drill pipe model.

3) Mostly, the maximum displacement point in computational results can be found absolutely at the same position as the measured ones.

4) The bottom positions only in the *z*-direction along the pipe length were changed according to the deformation profile of the rotating drill pipe model under the given

constraints, and the total length of the pipe model remained unchanged both in the experiment and simulation.

This study also investigates the dynamic behavior of the rotating drill pipe model due to the Magnus effect by analyzing the effect of internal viscous damping on the pipe's deformation and setting up the appropriate damping constant for the internal damping model in ANCF. Based on the comparative studies of the two hyper-elastic material models, the deformation of the drill pipe model with the fluctuation of WOB condition was discussed and the bottom position changes in the z direction and the maximum displacement in x and y directions according to the WOB were analyzed and discussed as follows.

(i) To study the effect of the internal damping model on drill pipe behavior, different damping constants were analyzed, and it was observed that the optimum deformation profile occurred at the damping constant, ξ was equal to 0.02.

(ii) For the consideration of material hyper-elastic models, the deformation profiles in Mooney Rivlin are more coincide with the experiment results while fluctuation of WOB is absent. Meanwhile, the Neo Hookean model is more stiffened than the Mooney Rivlin model and it is proposed to be used for the study of actual drill pipe behavior estimation in the future.

(iii) Under the WOB fluctuation, the proper deformation profiles were obtained at 22.5% *NR* in the Mooney Rivlin model and 45% *NR* in the Neo Hookean model with all the same constraints applied in the ANCF simulation.

Finally, it was observed that the WOB fluctuations of the non-rotating pipe model and for rotating pipe model coincide at 22.5% of *NR* based on the studies of (Suzuki et al., 2022). The preliminary consideration of the dynamic behavior of the actual drill pipe was analyzed and discussed based on the effect of hydrodynamic force consideration and the setting up for the appropriate damping constant of the pipe model. To sum up, this study proposed the implementation of the dynamic behavior of the drill pipe model in uniform flow due to the Magnus effect by applying the ANCF numerical simulation method and the simulation results indicated reasonable agreement with the experimental results in the case of the rotating drill pipe model for different rotational velocities. Furthermore,

the preliminary study of actual scale drill pipe was initiated straightforwardly, and it could be the reference study case for future drill pipe dynamic research.

7.2 Future Works

For the estimation of hydrodynamic forces exerted on the drill pipe, we need to approach a better estimation method for the nonlinear hydrodynamic force model for three-dimensional components and applied to the rotating drill pipe model of the ANCF simulation.

It is also needed to consider the coupling effect in terms of the tension, biaxial, and twisting of the drill pipe model, and pipe bending concerned with the Magnus effect will be calculated and discussed respectively.

It could be checked that the influence of other drill pipe dynamics and the study of actual drill pipe behavior in current and the unsteady flow condition for rotating drill pipe behavior will be certainly carried out for future studies.

Moreover, Fluid-Structure Interaction (two-way FSI) proposals for studying the nonlinear behavior of the rotating drill pipe both in steady and unsteady flow conditions should be applied.

The fluctuation of WOB that will be exerted at the lowermost part of the drill bit and the weight and buoyancy distribution of each element along the length of the model drill pipe should be improved accordingly.

It was proposed that a non-linear viscoelastic model that can capture the deformation of the real drilling situations, and the application of the elastic-plastic model for different material properties of the drill pipe should have been analyzed in the consideration of the actual drill pipe's dynamic behavior in straightforwardly.

To conclude, the number of computational times should be reduced properly since actual scale drill pipes are thousands of meters long and several element numbers and node points are included in numerical simulation. Therefore, the calculation accuracy and computational efficiency should have been upgraded for studying the actual drill pipe's dynamic behavior as a future study.

References

ANSYS (2020). ANSYS Fluent 2020 R2, Retrieved from https://www.ansys.com.

Batchelor, G.K.(1967) “An introduction to Fluid Dynamics”, page.427, Cambridge University Press.

Blevins, R.D., Coughran C.S., Utt, M.E. and Raghavan, K (2017)” Drilling-Induced Riser Vibration”, Int. J. Offshore Polar Eng. Vol. 27 No. 03:pp. 232–238.

Berzeri, M, Shabana, AA (2000). “Development of simple models for the elastic forces in the absolute nodal coordinate formulation,” J Sound Vib, 235 (4), 539–565.

Chen, W, Rheem, CK (2019). “Experimental investigation of rotating cylinders in the flow,” JMST, 24 (1), 111-122.

Chung, J. and Felippa C.A.(1981). “Nonlinear State Analysis of Deep Ocean Mining Pipe – Part II: Numerical Studies” ASME J Energy Resources Tech, 103, pp.11-25.

Chung, J. and Whitney A. K. (1993). “Flow-induced Moment and Lift for a Circular Cylinder with Cable Attachment,” Intl J of Offshore and Polar Engineering, 1993, (3), 4, pp.280-287.

García-Vallejo, D, Valverde, J, Domínguez, J (2005). “An internal damping model for the absolute nodal coordinate formulation, Nonlinear Dynamics, 42(4), 347–369.

Gerstmayr, J, Shabana, AA (2006). “Analysis of Thin Beams and Cables Using the Absolute Nodal Coordinate Formulation,” Nonlinear Dynamics, 45(1), 109-130.

Hoerner, S. F, (1985). “Fluid-Dynamic Lift: Practical Information on Aerodynamic and Hydrodynamic Lift”, 2nd Edition, ISBN-10 : 9998831636.

Htun, TZ, Suzuki, H, Kuwano, A, Tomobe, H, Inoue, T (2019). “Numerical Motion Analysis of ROV coupled with Tether Applying 24-DOFs Absolute Nodal Coordinate Formulation,” Proc 29th Int Offshore and Polar Eng Conf, Honolulu, ISOPE.

Htun, TZ, Suzuki, H, Garcia-Vallejo, D (2020). “Dynamic modeling of a radially multilayered tether cable for a remotely operated underwater vehicle (ROV) based on the absolute nodal coordinate formulation (ANCF),” Mechanism and Machine Theory, 153, 10396.

Htun, TZ, Suzuki, H, Garcia-Vallejo, D (2022). “On the theory and application of absolute coordinates-based multibody modeling of the rigid-flexible coupled dynamics of a deep-sea ROV-TMS (tether management system) integrated model,” Ocean Engineering, DOI: 10.1016/j.oceaneng.2022.111748.

Inoue, T, Rheem, CK, Sakaguchi, M, Matsuo, H (2013). “Experimental Study on the Characteristics of VIV and Whirl Motions of Rotating Drill Pipe,”, Proc. of OMAE2013, OMAE2013-10182.

Inoue, T, Wada, K, Osawa, N, Fujikubo, M, Suzuki, H, Santus, C (2017a). “Technical Investigation on Drill Pipe Failure,” J of JASNAOE, 26, 183-193 (in Japanese).

Inoue, T, Suzuki, H, Thaw Tar, Senga, H, Wada, K, Matsuo M.Y (2017b). “Numerical Simulation of Motion of Rotating Drill Pipe due to Magnus Effect in Riser less Drilling,” Proc. of OMAE2017, OMAE2017-62327.

Inoue, T, Suzuki, H, Katsui, T, Tsuchiya, K, Notani, Y (2019). “Experimental and Numerical Study of Motion of Rotating Drill Pipe owing to Magnus Effect,” Proc. of OMAE2019, OMAE2019-96602.

Koga. T, (2022). “Study on Improvement of Method for Estimating Underwater Behavior of Drill Pipe Using ANCF”, Master Graduation Thesis, Osaka University.

Ma, C, Wang, R, Wei, C, Zhao, Y (2016).“A new absolute nodal coordinate formulation of solid element with continuity condition and viscosity model,” Int. J. Simul.: Syst. Sci. Technol. 1, 101–106.

Mooney, MA (1940). “Theory of Large Elastic Deformation,” J of Applied Physics, 11, 582-592.

Nakajima, T, Motora, S, Fujino, M (1983). “A Three-Dimensional Lumped Mass Method for the Dynamic Analysis of Mooring Lines,” J. of the Society of Naval Architects of Japan, 154, 192-202 (in Japanese).

Nuttall, P. and Kaitu’u J.(2016)” The Magnus Effect and the Flettner Rotor: Potential Application for Future Oceanic Shipping”, The Journal of Pacific Studies, Vol.36 Issue 2, pp.162-188.

Orzechowski, G, Fraczek, J (2015). “Nearly incompressible nonlinear material models in the large deformation analysis of beams using ANCF,” Nonlinear Dynamics, 82 (1) 451–464.

Otsuka, K. (2022). “Recent Advances in the Absolute Nodal Coordinate Formulation: Literature Review From 2012 to 2020”, Journal of Computational and Nonlinear Dynamics, Vol.17, 080803-1.

Ozturk, D.(2020)” Performance of a Magnus effect-based cylindrical roll stabilizer on a full-scale Motor-yacht”, Ocean Engineering, Vol.218, 108247.

Rivlin, RS, (1948). “Large elastic deformations of isotropic materials”, Collective electron ferromagnetism III, 195. A, 463-473.

Shabana, AA, Hussien, HA, Escalona, JL (1998). "Application of the Absolute Nodal Coordinate Formulation to Large Rotation and Large Deformation Problems," J Mech Des, ASME, 120, 188-195.

Shabana, AA, Yakoub, RY (2001). "Three-Dimensional Absolute Nodal Coordinate Formulation for Beam Elements; Theory," J Mech Des, ASME, 123, 606-613.

Sopanen, JT, Mikkola, AM (2003a). "Studies on the Stiffness Properties of the Absolute Nodal Coordinate Formulation for Three-Dimensional Beams," Conf. proc. of DETC'03, ASME.

Sopanen, JT, Mikkola, AM (2003b). "Description of elastic forces in the absolute nodal coordinate formulation", Nonlinear Dynamics, 34(1), 53–74.

Suzuki, H, Inoue, T, Thaw Tar, Senga, H (2016). "Numerical Study on Underwater Behavior of Rotating Drilling Pipe set in the tidal current," Conf. Proc. of JASNAOE, 23, 555-559, (In Japanese).

Suzuki, H, Tsuchiya, T, Inoue, T, Katsui, T, Senga, H, Nagaishi, Y, Notani, Y (2018). "Experimental and Numerical Study on the Underwater Behavior of Rotating Drill Pipe", Conf. Proc. of JASNAOE, 27 , 357-364. (In Japanese).

Suzuki, H, Inoue, T, Katsui, T, Wada, R, Tsuchiya, K, Notani, Y, Ishida, K, Koga, T (2022). "Experimental and Numerical Studies of Rotating Drill Pipe Model in Uniform Flow," Int J of Offshore and Polar Engineering, 32, 285–295.

Suzuki, M, Ikoma, T, Aida, Y, Masuda, K, Rheem, CK (2020). "Experimental Study on Edge Effects of Rotating Circular Cylinder in Uniform Flow", Conf. Proc. of JASNAOE, 30, 265-268 (in Japanese).

Takehara, S, Terumichi, Y, Sogabe, Y (2011). "Motion of a Submerged Tether Subject to Large Deformations and Displacements," J System Design and Dynamics, 5(2), 296-305.

Tamano, O, Toshie, T, (2019). "Bonds on the Day of the Tsunami: Children on the Deep-Sea Drilling Vessel, Chikyu", a hardcover book published by Tomiyama International.

Tun, H, Suzuki, H, Koga, T, Htun, TZ, Inoue, T (2023). "Nonlinear Dynamics Analysis of a Rotating Drill Pipe Model incorporating Magnus effect and Rotary Inertia of the Pipe," Int. J. Offshore Polar Eng, 33 (03), 286–293.

Wang, J, Hurskainen, VV, Matikainen, MK, Sopanen, J, Mikkola,A (2017). "On the Dynamic Analysis of Rotating Shafts Using Nonlinear Super element and Absolute Nodal Coordinate Formulations," Advances in Mechanical Engineering, 9(11), 1–14.

Yakoub, RY, Shabana, AA (2001). "Three-Dimensional Absolute Nodal Coordinate Formulation for Beam Elements; Implementation and Applications," J Mech Des, ASME, 123, 614-621.

Zhao, G., Zhao, L., Zhang, Y., X. and Li, J(2018)" Finite Element Analysis of Dynamic Fracture Behavior of Drill Pipe Under Various Impact Loads", MECHANIKA. Volume 24(4): pp.404-411.

Research Publications

1."Nonlinear Dynamics Analysis of a Rotating Drill Pipe Model Incorporating the Magnus Effect and Rotary Inertia of the Pipe", International Journal of Offshore and Polar Engineering (ISSN1053-5381), http://www.isope.org/publications, Vol.33, No.3, September 2023, pp.286-293; https://doi.org/10.17736/ijope.2023.jc900.

2. "Numerical Analysis of the Effect of Internal Viscous Damping on the Dynamic Behavior of a Rotating Drill Pipe Model", Conference Proceedings of the Thirty-fourth (2024) International Ocean and Polar Engineering Conference, Rhodos, Greece, June 16-21, 2024.